Label-Free Detection of Molecular Interactions

by

Runli Liang

A Dissertation Presented in Partial Fulfillment
of the Requirements for the Degree
Doctor of Philosophy

Approved March 2021 by the
Graduate Supervisory Committee:

Shaopeng Wang, Co-Chair
Jennifer Blain Christen, Co-Chair
Tianwei Jing
Chao Wang

ARIZONA STATE UNIVERSITY

May 2021

ABSTRACT

Quantifying molecular interactions is critical to the understanding of many biological processes and drug screening. To date, various detection techniques have been developed to determine the binding kinetics. However, because most of the mainstream detection technologies detect signals that scale with the mass of ligands bond to the sensor surface, it is still challenging to quantify the binding kinetics of small molecules. To address this problem, two different detection technologies, charge-sensitive optical detection (CSOD) and critical angle reflection (CAR), are developed for label-free detection of molecular interactions with the ability to detect a wide range of molecules including small molecules.

In particular, CSOD technique detects the charge rather than the mass of a molecule with an optical fiber. However, the effective charge of a molecule decreases with the buffer ionic strength. For this reason, the previous CSOD works with diluted buffers, which could affect the measured molecular binding kinetics. Here a technique capable of detecting molecular binding kinetics in normal ionic strength buffers is presented. An H-shaped sample well was developed to overcome this problem. With this new design, the binding kinetics between G-protein-coupled receptors (GPCRs) and their small molecule ligands were measured in normal buffer. To further improve the signal-to-noise ratio of CSOD and move it toward high-throughput detection, CSOD was implemented with a quadrant-cell detector to achieve detection in higher frequency range and decrease low-frequency noise.This improved CSOD technique is capable for direct quantification of binding kinetics of phage-displayed peptides to their target protein using the whole phages.

CAR imaging can be performed on surface plasmon resonance (SPR) imaging setups. It was shown that CAR is capable of measuring molecular interactions including

proteins, nucleic acids and cell-based detections. In addition, it was shown that CAR can detect small molecule bindings and intracellular signals beyond SPR sensing limit. CAR exhibits several distinct characteristics over SPR, including tunable sensitivity and dynamic range, deeper vertical sensing range, and fluorescence compatibility. CAR is anticipated to have the ability to expand SPR capability in small molecule detection, whole cell-based detection, simultaneous fluorescence imaging, and broader conjugation chemistry.

ACKNOWLEDGMENTS

My deepest gratitude goes to my late advisor Dr. Nongjian (NJ) Tao for his guidance and support over the years. There isn't a day that goes by in the lab that we don't think about his advice and miss him. He has set an example of excellence as a researcher, mentor, instructor, and role model.

I would like to express my appreciation to Dr. Shaopeng Wang for his indispensable help and advise in my research. His optimism and amiability makes working with him a pleasant experience. I have also learnt so much from his strong sense of curiosity.

I am thankful to Dr. Jennifer Blain Christen for her help during the hard times, she took on the co-advisor job without hesitation and has helped me through.

I am also thankful to other current and previous group members who helped me with my research with numerous discussions and on-site instructions: Dr. Guangzhong Ma, Dr. Yan Wang, Dr. Wenwen Jing, Dr. Yunze Yang, Dr. Fang Chen, Dr. Yixian Wang, Dr. Fenni Zhang, Dr. Pengfei Zhang, Dr. Chenwen Lin, Dr. Manni Mo, Dr. Hui Wang, Dr. Yueqi Li, Dr. Yue Deng, Dr. Fanyi Zhu, as well as Mr. Zijian Wan, Ms. Yi Wang and Ms Nanxi Yu. Dr. Nguyen Ly and Dr. Tianwei Jing from Biosensing Instrument also provided tremendous help to my research.

I acknowledge our collaborator, Dr. Hengzhu and Dr. Prashant Desai from Johns Hopkins University for providing VirD samples, and Dr. Yingnan Zhang from Genentech for providing M13 bacterial phage samples.

I would like to thank Dr. Chao Wang and Dr. Tianwei Jing for serving on my committee and providing constructive suggestions in my research.

I would like to thank Henrietta Lacks and her family. Henrietta Lacks, and the HeLa cell line that was established from her tumor cells without her knowledge or consent in 1951, have made significant contributions to scientific progress and

advances in human health. We are grateful to Henrietta Lacks, now deceased, and to her surviving family members for their contributions to biomedical research.

Lastly, but absolutely not least, Purry, Kenny, Jing, Chuhong, Xiong, and my parents, they have been a source of steadfast and unconditional love during these many years of study. Their support has meant more than words can express.

TABLE OF CONTENTS

CHAPTER Page

LIST OF TABLES

LIST OF FIGURES

Figure Page

Chapter 1

INTRODUCTION AND BACKGROUND

1.1 Introduction

Measuring molecular binding kinetics is critical to the understanding of many biological processes, including intercellular communication, enzymatic [1, 2, 3] and metabolic activities [4, 5, 6], and to the discovery and validation of drugs.[7, 8] To date, various detection techniques have been developed to determine the binding kinetics, which are divided into two categories, labeled and label-free detection techniques. Label-free methods for kinetic binding analysis are preferred over labeled methods such as enzyme-linked immunosorbent assay (ELISA) [9, 10] and Microscale Thermophoresis (MST)[11], because direct detection of a molecular binding process reduces secondary effects and complexity, and more importantly, produces real-time binding kinetics. For these reasons, many label-free methods have been developed, include surface plasmon resonance (SPR),[12], biolayer interferometry (BLI),[13] backscattering interferometry (BSI),[14, 15, 16] waveguide interferometry,[17] quartz crystal microbalance (QCM), [18] and surface acoustic wave (SAW) sensors[19, 20]. These techniques have greatly contributed to the understanding of molecular binding interactions.

Usually, binding kinetics and binding affinity are used to describe the binding process between a drug and its receptor. While binding affinity, quantified as the equilibrium dissociation constant K_D, describes the amount or concentration of a drug bound to its receptor at equilibrium, has been widely used in drug discovery, it was suggested that the kinetics of drug-receptor binding could be equally important to, or

sometimes more important than affinity in determining drug efficacy. In this chapter, detailed binding kinetics will be discussed, then different detection methods will be introduced.

1.2 Binding Kinetics

The binding kinetics between a drug and its receptor is described by rate constants k_a and k_d, which reflect the rate of drug-receptor association and dissociation respectively. Sometimes the notion k_{on} and k_{off} are used instead. Consider a reaction between a drug (L) and a receptor (R) to form a bi-molecular complex (LR):

$$L + R \underset{k_d}{\overset{k_a}{\rightleftharpoons}} LR \tag{1.1}$$

This mechanism comprises a single elementary step - the binding (or unbinding) of the drug - without any intermediate states, which is a first order binding kinetics.

The dissociation constant, K_D, which describes the binding affinity, is the ratio of relevant concentrations at equilibrium:

$$K_D = \frac{[L][R]}{[L]} \tag{1.2}$$

At equilibrium, the drug concentration at which half of receptor binding sites are occupied is equal to K_D (both in unit of moles per liter). K_D is directly related to the free energy difference, ΔG_d, between the bound and unbound states. However, the rate constants k_a and k_d depend on transient interactions along the binding pathway. The thermodynamics and kinetics of binding are linked as:

$$K_D = \frac{k_a}{k_d} \tag{1.3}$$

Where k_{on} and k_{off} are association rate constant and dissociation rate constant respectively. In theory, it is possible to have different drugs with different k_a and k_d

while having the same K_D. If K_D is the only parameter that is measured, we would not be able to assess in terms of which drug is better. It is possible that one drug has both slower on- and off-rates. Additionally, the average time that a drug stays bound to its receptor, the residence time is related to the dissociation rate constant: $t_R = 1/k_{off}$. We lose information as to how long the drug keeps bound to their receptors if only K_D is measured[21].

1.3 State of the Art Detection Technology

1.3.1 Enzyme Linked Immunosorbent Assay (ELISA)

Modern-day enzyme-linked immunosorbent assay (ELISA) was first introduced in the 1970s when researchers replaced the radioisotopes in tagged antigens and antibody with enzymes. Nowadays, ELISA has become a routinely used method and the golden standard in protein study[22]. ELISA utilizes the basic immunology concept that an antigen binds to its specific antibody, this allows detection of very small quantities of antigens such as proteins, peptides, hormones, or antibody in a fluid sample[23] . There are many types of ELISA including: direct, indirect, sandwich, and competitive ELISA (Figure 1[24]).

In direct ELISA, the surface of the plate is coated directly with the antibody or antigen. An enzyme tagged antibody or antigen enables the measurement. Even though direct ELISA requires the least steps, it is not widely used. Designing and labelling each primary antibody is not only time consuming but expensive.

Indirect ELISA uses a secondary antibody with enzyme labels to enable detection while primary antibody was used for binding. As the structure of the primary antibody

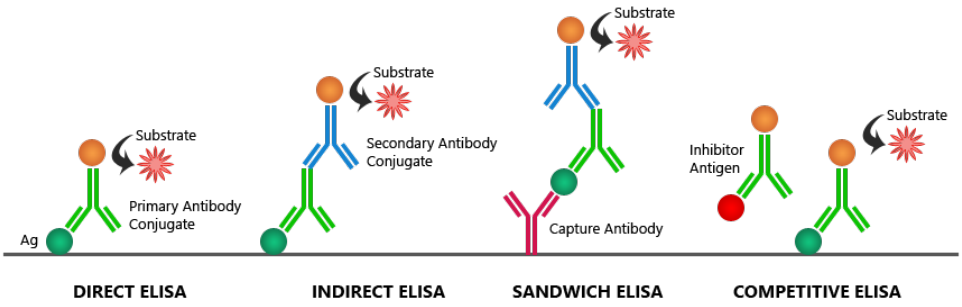

Figure 1. **Common ELISA types.**

is retained, the immunoreactivity is retained. Besides, in indirect ELISA, there are several epitopes on each primary antibody, allowing binding of secondary antibody thus amplifies the signal. However, in each step, incubation is needed and wash steps are required, making the procedure time consuming.

Sandwich ELISA is the most widely used ELISA method in protein detection. The antigen or antibody to be detected is sandwiched between the detection and primary antibody. Secondary antibodies that are tagged with enzyme enable measurement. The sandwich assay provides high specificity and sensitivity because the capture antibody excludes many nonspecific absorbed proteins on the substrate[22].

The advantages of ELISA are obvious in that it has high sensitivity and selectivity, enabling measurement of low concentration biomolecules in complex environments[23]. However, there are many limitations to ELISA. First, incubation and washing steps are time consuming. Second, ELISA is usually an endpoint assay, meaning that it would be hard to study binding kinetics with traditional ELISA. Furthermore, to study the interaction between small molecules and protein, the small size of the molecules makes it difficult to attach any enzyme tags to small molecules without affecting the interaction between small molecules and protein, which will reduce the accuracy of the technique.

1.3.2 Surface Plasmon Resonance (SPR)

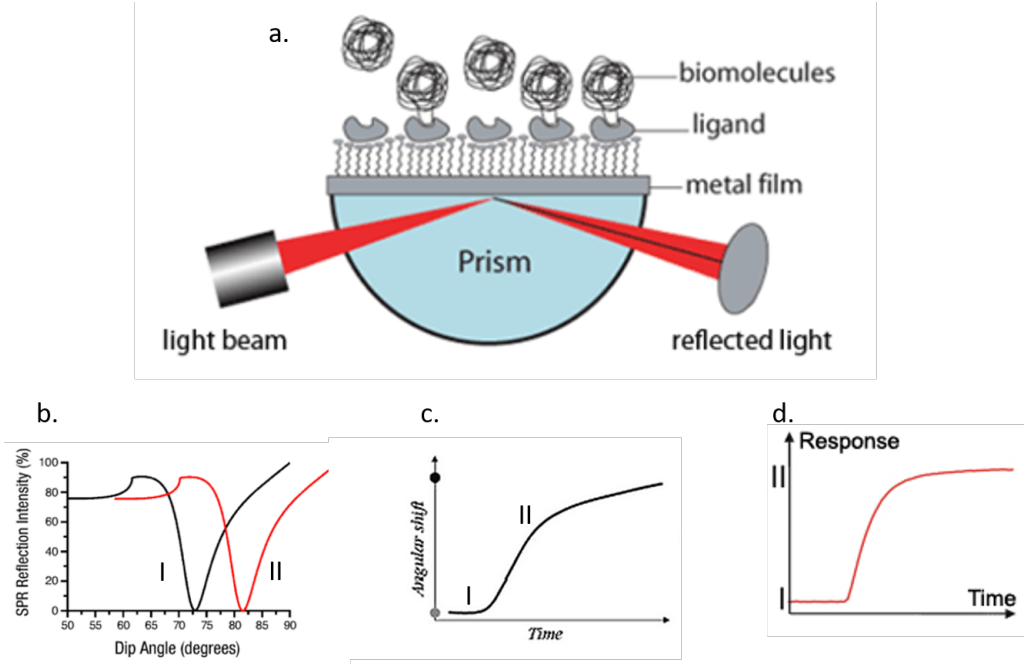

Figure 2. **SPR configuration.** (a). The Kretschmann configuration of SPR. (b). Resonance angle shift upon binding between molecules, resonance angle will shift form I to II. (C). Measured resonance angle shift as a function o time. (d). When SPR angle is fixed, measured reflective light intensity change with time.

Since the first demonstration of surface plasmon resonance for the study of processes at the surfaces of metals and sensing of gas in 1980s, SPR biosensors have become one of the most important tools in characterizing and quantifying biomolecular interactions[25]. By detecting the binding induced refractive index change, SPR can achieve real-time analysis of biospecific interactions without the use of labeled molecules[26].

A widely used SPR configuration is the Kretschmann configuration[27] (Figure 2a). A light beam is shone upon a metal film through a prism. When the incident angle reaches resonant angle, the surface plasmons are set to resonate with the light.

As a result, the reflective light intensity goes to minimum due to the absorption of the incident light energy by the exited surface plasmons. The resonance angel depends on the refractive index of medium near the metal film surface. When binding between molecules happens, the refractive index is changed due to the mass change, which then gives a resonance angle shift as shown in Figure 2b. There are two ways to measure the binding, first is to measure the resonance angle shift (Figure 2c), second is to fix the angle, and measure the reflective light intensity change (Figure 2d).

It was shown in a study of small molecules with carbonic anhydrase II that, by comparing the results to isothermal titration calorimetry and stopped-flow fluorescence, SPR can achieve results in agreement with those solution-based measurement[28]. It was shown that SPR can be used for studying the binding of small molecules ($<$ 1000 Daltons) to large targets[29, 30, 31].However, as SPR is a mass dependent detection method, the limit of detection drops with the size of the molecule of interest. This poses a major challenge for applying SPR to small-molecule drug discovery.

1.3.3 Backscattering Interferometry (BSI)

Backscattering interferometry is another method widely used in studying molecular interaction by monitoring the change in refractive index[32]. Figure 3 shows a typical configuration for BSI. Probing the object with an unfocused He-Ne beam at nearly 90°($\pm$7° to allow fringes to be viewed), results in a high-contrast interference fringe pattern in in the backscattered direction. Tracking the position of fringes enables the change of refractive index to be quantified. The most common interferometer configuration is based on a microfluidic chip currently[33].

It was reported that BSI can achieve similar detection limit compared with SPR

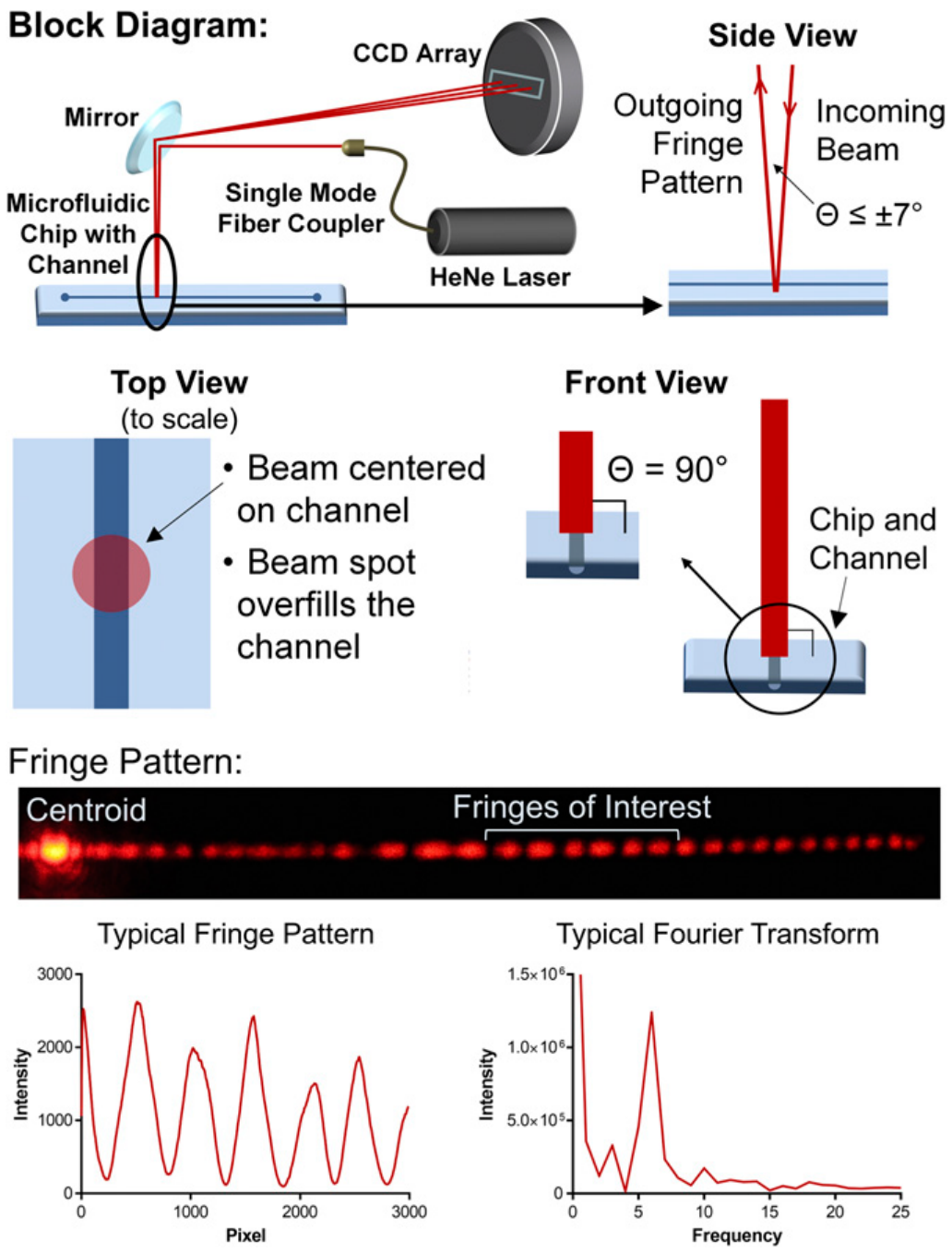

Figure 3. **BSI configuration.**

at $\Delta RI = 10^{-6}$[32, 33]. Furthermore, BSI is not a mass based method thus does not have the limitations SPR does when it comes to small molecules detection. However, as a free-solution technique, BSI can have difficulties measuring dissociation, therefore cannot get rate constants. While measuring affinity could be useful, as stated before, rate constants provides more information on drug efficacy.

Chapter 2

CHARGE-SENSITIVE OPTICAL DETECTION OF SMALL MOLECULE BINDING KINETICS IN NORMAL IONIC STRENGTH BUFFER

2.1 Introduction

Measuring molecular binding kinetics is critical to the understanding of many biological processes, including intercellular communication1, enzymatic [1, 2, 3] and metabolic activities,[4, 5, 6] and to the discovery and validation of drugs. [7, 8]To date, various detection techniques have been developed to determine the binding kinetics, which are divided into two categories, labeled and label-free detection techniques. Label-free methods for kinetic binding analysis are preferred over labeled methods, such as enzyme-linked immunosorbent assay (ELISA) [9, 10] and Microscale Thermophoresis (MST),[11] because direct detection of a molecular binding process reduces secondary effects and complexity, and more importantly, produces real-time binding kinetics. For these reasons, many label-free methods have been developed, include surface plasmon resonance (SPR),[12], biolayer interferometry (BLI),[13] backscattering interferometry (BSI),[14, 15, 16] waveguide interferometry,[17] quartz crystal microbalance (QCM), [18] and surface acoustic wave (SAW) sensors.[19, 20] These techniques have greatly contributed to the understanding of molecular binding interactions.

However, because the signal of above label-free methods scales with the mass of ligands bound to the sensor surface, quantifying the kinetics of small molecule ligand binding with large protein receptors is still challenging due to the large mass ratio between the receptors and the ligands. Small molecules represent $\sim 90\%$ of

approved drugs, and over 60% of small molecule drug targets are membrane protein receptors.[34] Purified membrane proteins need to be stabilized in an amphiphilic environment to remain functional, [35, 36] using technologies such as nanodisc that forms nanoscale patches of phospholipids surrounding the membrane proteins,[37] and virion display technology (VirD) that expresses membrane proteins on the lipid envelope of virions.[38] These complex assemblies are much larger than membrane proteins alone and so they cannot be densely packed on the sensor surface, which reduces the sensitivity and makes detection of small molecule ligands a challenge for existing mass sensitive technologies.[39]

We have developed a charge sensitive optical detection (CSOD) method[40, 41] that measures molecular binding kinetics by detecting the surface charge changes instead of mass changes. We have shown that this label-free method is capable of measuring both large and small molecules, including binding kinetics between small molecule ligands and nanodisc stabilized membrane proteins receptors.[41] However, like other charge-based detection methods,[42, 43, 44, 45, 46] CSOD faces the issue of the charge screening effect, making it difficult to detect molecular charge changes in commonly used buffers that has relatively high ionic strength. Due to this difficulty, charge based detection methods are limited to diluted buffers. However, the decreased ionic strengths could affect protein conformations and electrostatic interactions between binding pairs, thus altering the binding kinetics.[47] The restriction in the buffer condition is also a barrier for broader adoption of charge sensitive detection technology. To overcome these challenges, we report a new experiment scheme that enables CSOD to detect molecules in undiluted buffers, which is a significant advance for molecular binding kinetics measurements with the charge sensitive detection method.

2.2 Detection Principle

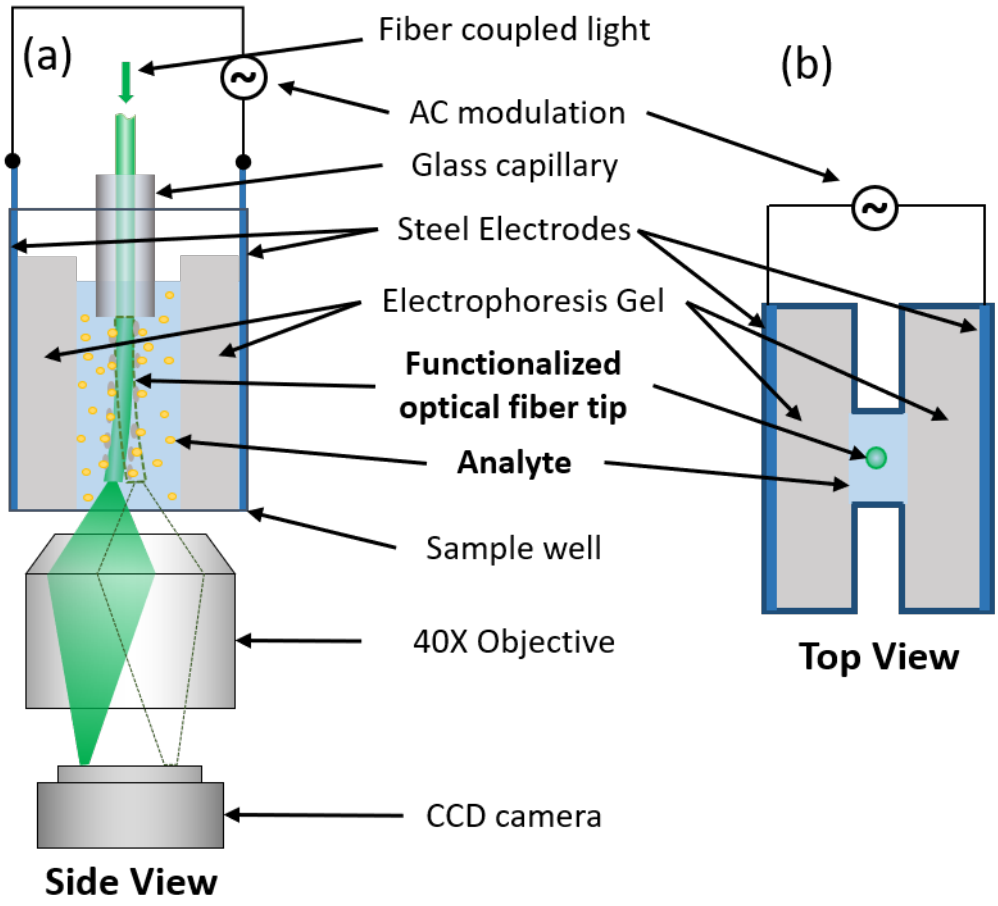

Figure 4. **Principle of the charge-sensitive optical detection in normal buffer.** (a) schematic illustration of the setup. (b) Top view of the sample well.

A schematic of CSOD system is shown in Figure 4. Details of the CSOD detection principle have been described previously.[40, 41] Briefly, a glass optical fiber functionalized with molecular receptors is dipped into a solution well. If the solution well contains charged molecular ligands, binding of the ligands to the receptors changes

the fiber surface charge. To monitor the charge change, an alternating electric field is applied perpendicular to the optical fiber and drives the fiber to oscillate. The oscillation amplitude x, at frequency ω is proportional to the surface charge of the optical fiber, given by

$$x = \frac{2\pi \left|\overrightarrow{E(\omega)}\right| \sigma r l}{\sqrt{(k_{eff} - m_{eff}\omega^2)^2 + (c\omega)^2}} \tag{2.1}$$

where $\left|\overrightarrow{E(\omega)}\right|$ is the electric field strength, c is the damping coefficient, and k_{eff},m_{eff},r and l are the effective spring constant, mass, radius and length of the optical fiber, respectively.

A key task of CSOD is thus to precisely measure the oscillation amplitude. To measure the oscillation amplitude, light is coupled into the fiber, the oscillation of the fiber tip is then tracked from the optical image of the tip as shown in Figure 5, together with a differential optical position tracking algorithm. The algorithm tracks the position of the optical fiber tip using optical imaging. The image of the fiber tip appears as a bright spot (shown in Figure 5a). The differential optical detection method determines the oscillation amplitude of the optical fiber by dividing the bright spot into two regions of interest, A and B, with a line perpendicular to the fiber oscillation direction (Figure 5b). The division line is selected such that the intensities in areas A and B are similar at the beginning. The camera is continuously monitoring $(I_A - I_B)/(I_A + I_B)$, where I_A and I_B are the intensities of regions A and B, respectively. It was shown in previous study that $(I_A - I_B)/(I_A + I_B)$ is proportional to the oscillation amplitude of the fiber as shown in Figure 6[40].

To detect binding events with CSOD, according to Equation 2.1, a change in the charge upon binding is required. Most biologically significant molecules are charged

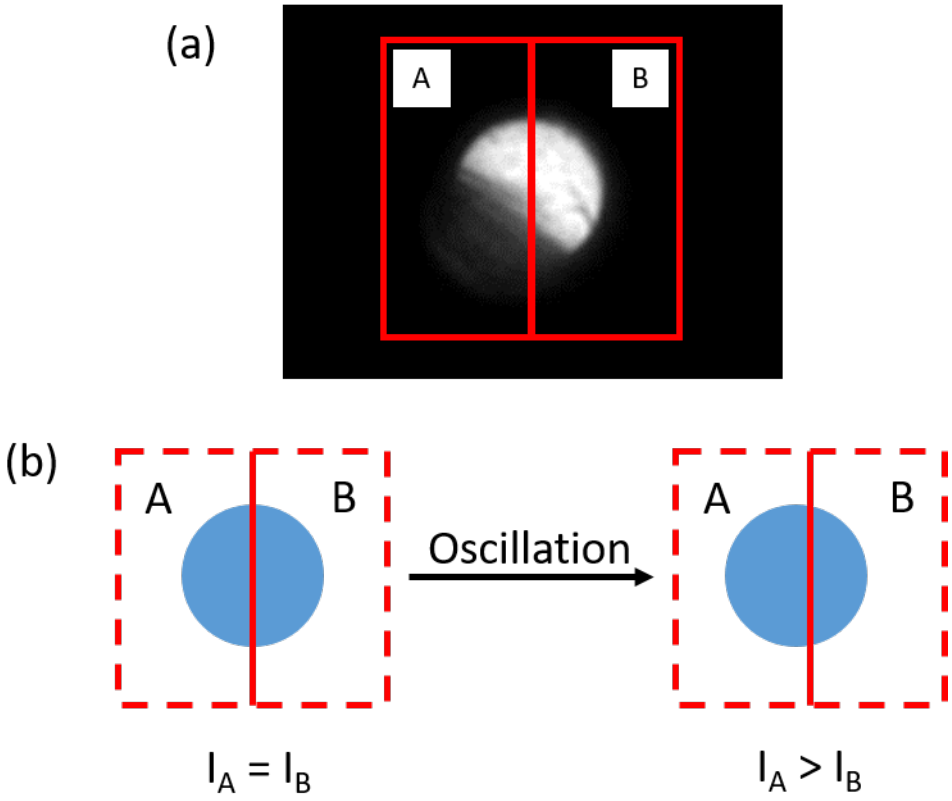

Figure 5. **Image of fiber tip.** (a) Image of the fiber tip viewed from the bottom of the microplate well. (b) Differential optical detection for accurate determination of the fiber.

or partially charged. For example, over 90% of FDA approved small molecule drugs are charged (http://www.drug-bank.ca). For molecules that are not charged, the binding of the small molecule to a protein might result in a conformation change and therefore changes the effective surface charge of the protein and makes the molecular interaction detectable by CSOD. However, in commonly used buffers for binding kinetic measurement, the effective charge of a molecule is significantly reduced due to ionic screening effect. The surface charge of the optical fiber in analyte solution is partially screened by counter ions. According to the Debye-Hückel theory[48], the

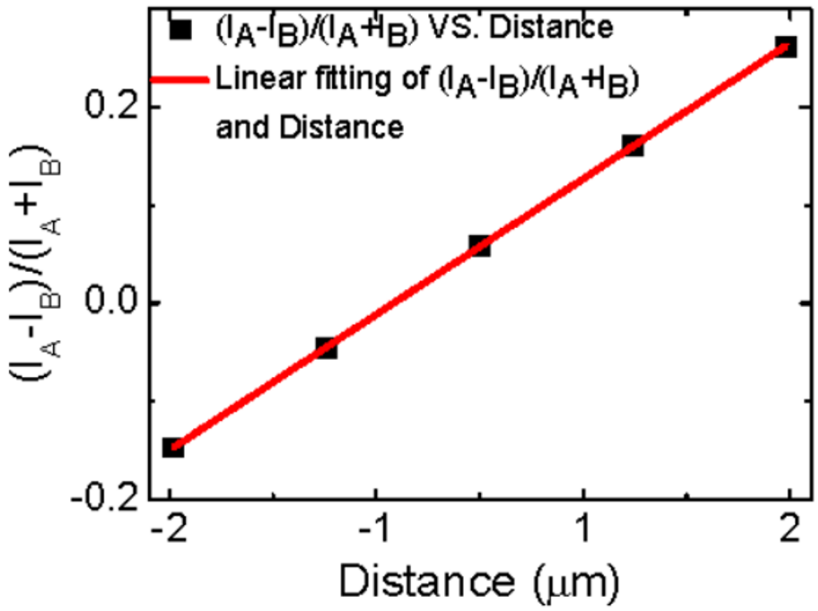

Figure 6. **Fiber oscillation amplitude calibration.** Relationship between differential intensity $(I_A - I_B)(I_A + I_B)$ and fiber movement (shifting of ROI), where the red line is a linear fit.

ratio between the effective charge and the actual charge could be estimated by:

$$\frac{\sigma_{eff}}{\sigma_{actual}} = \frac{\zeta}{\psi} = e^{-\kappa x} \tag{2.2}$$

where σ_{eff} and σ_{actual} are the effective and actual surface charge density on the fiber, ζ is the zeta potential, ψ is the potential at the surface, x is the slipping layer thickness and $\kappa^{-1}$is the Debye length, which is:

$$\kappa^{-1} = \sqrt{\frac{\epsilon\epsilon_0 k_B T}{2N_A e^2 c}} \tag{2.3}$$

Where ϵ is the dielectric constant of the solution, ϵ_0 is the permittivity of the free space, k_B is the Boltzmann constant, T is the temperature, N_A is the Avogadro number, and c is the ionic strength. From the above equations, we simulated the following result where for different slipping layer thickness the charge screening effect is shown in Figure 7.

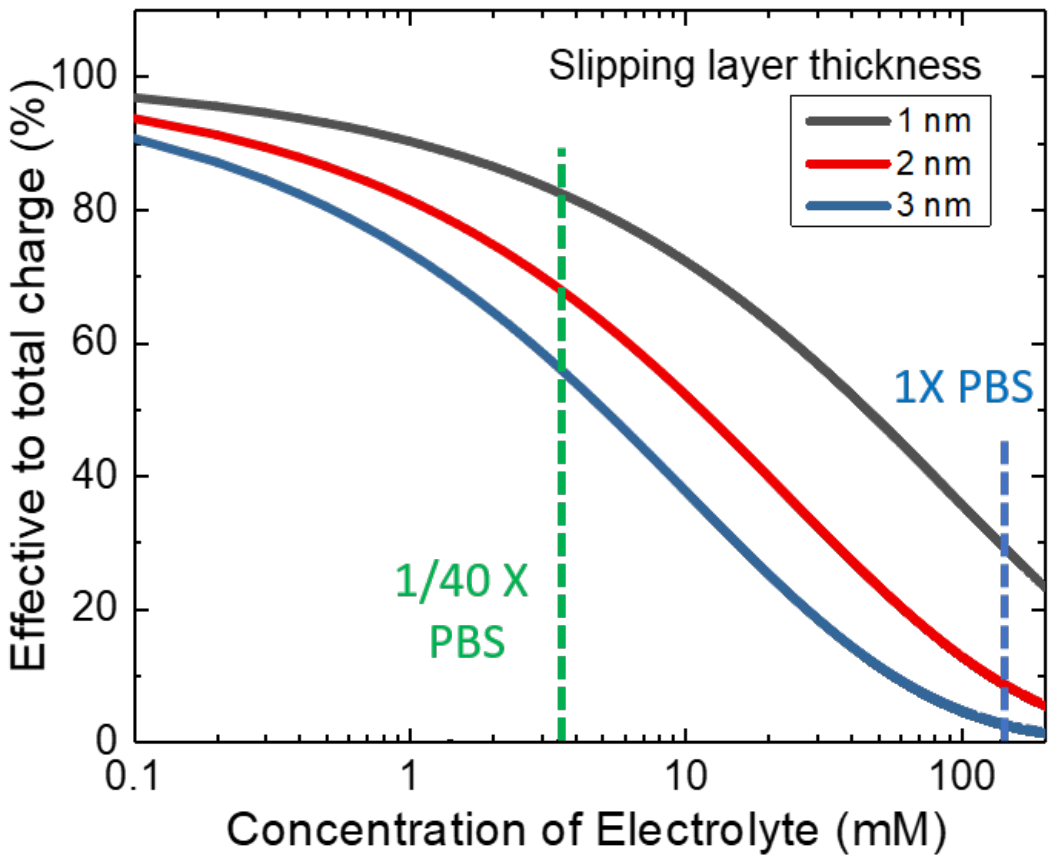

Figure 7. **Ionic screening and effect:** effective surface charge density (presented as the ratio of the effective surface charge to the actual charge) plotted as a function of electrolyte concentration. Green and blue dash lines indicate the electrolyte concentration of 40 times diluted PBS and normal ionic strength PBS, respectively.

From Figure 7, it is shown that such screening effects are dependent on the ionic concentration. For example, the effective charge in undiluted phosphate buffered saline (PBS, with a total ionic concentration of about 150 mM) is reduced to $\sim 10\%$ of the effective charge in 40 times diluted PBS. [40] The reduced effective charge reduces CSOD signal and makes it difficult to apply CSOD to cases where biologically relevant buffers are needed.

In principle, one could increase the oscillation amplitude by increasing the applied electric field. This requires a large current density at the location of the optical fiber tip, as the electric field, E, is related to current density, J, and the solution conductivity σ by

$$J = \sigma \cdot E \tag{2.4}$$

The current density is determined by the total current, I, at the electrodes, and cross-sectional area of the well at the location of the fiber tip. The current is determined by electrochemical reactions on the electrodes, which can be increased by applying a large potential difference between the electrodes. This strategy, however, leads to larger electrochemical reactions, such as hydrolysis of water, which can produce gas bubbles and the associated reaction products could interfere the molecular binding processes on the fiber surface. In addition, the gas bubbles generate overpotential that alter the electrical current density[49], and also produce mechanical perturbation to the oscillation of the fiber probe. We overcome this difficulty using an H-geometry sample well shown in Figure4 , where two large wells are connected by a narrow channel. We placed two electrodes with large surface areas in the large wells, and the optical fiber tip in the narrow channel. Because the two electrodes have large surface areas, the current densities on the electrode area are reduced for a given current, which reduces the overpotential (η) and electrochemical reactions on the electrode surface, according to the Tafel equation,which describes how the electrical current through an electrode depends on the voltage difference between the electrodes, the bulk electrolyte concentration and overpotential [50]

$$i = nFkCe^{\pm\alpha F\frac{\eta}{RT}} \tag{2.5}$$

Where n is number of electrons being transferred, F is the Faraday constant, R is

the universal gas constant, T is temperature, C is the reactive species concentration on the electrode surface, k is the rate constant for the electrode reaction, and α is the charge transfer coefficient.

α is a value between 0 and 1. For a reaction with a single rate-determining step, it is defined as:

$$\frac{\alpha}{\nu} = \left| \frac{RT}{nF} \left(\frac{\partial \ln |I|}{\partial E} \right)_{p,T,c_i^{interface}} \right| \tag{2.6}$$

Where ν is the stoichiometric number, R is the universal gas constant, T is the absolute temperature, n is the number of electrons involved in the electrode reaction, F is the Faraday constant, E is the electrode potential and I is the partial electrode current.

α signifies the fraction of the interfacial potential at an electrode-electrolyte interface that helps in lowering the free energy barrier from the electrochemical reaction. [51]

α could be evaluated experimentally by obtaining a potential-current curve [52] or a $\ln I$ - E curve (A Tafel plot)[53].

The overpotential η is the potential difference between a half-reaction's thermodynamically determined reduction potential and the potential at which the redox event is experimentally observed. For example for a hydrolysis process, overpotential is the irreversibility that has to be overcome by the potential applied before production of hydrogen and oxygen can begin.[54]

Tafel equation state that the electrical current between the electrodes are not only depends on the applied voltage but also the electrolyte concentration and overpotential. In undiluted buffer, the high ionic strength will increase the current density. Overpotential can be divided into many different subcategories that are not all well-defined. The type of overpotential that relevant to the noise level of CSOD is likely the bubble

overpotential, a form of concentration overpotential caused by the evolution of gas at electrode surface, which reduces the effective electrode area and affect the stability of the electrical current density.[49] The instability of electrical current density will affect the stability of the electrical field driving the oscillation of the CSOD sensor probe, and the bubbles can also cause mechanical perturbation to the fiber probe. Therefore, overpotential add noise to the CSOD signal.

Since overpotential scales with the current density, reduction of the current density will reduce overpotential and thus improve the signal to noise ratio of CSOD measurement. Our innovative H-shape well design with enlarged electrode surface area allows us to minimize the current density at the electrodes to reduce overpotential induced noise, while the small cross section area at the fiber probe location provide high current density thus high strength electrical field to generate sufficient fiber oscillation signal. Therefore, the H-shape design increase the overall CSOD signal to noise ratio and enable sensitive measurement in undiluted buffers.

In equation 2.5 The electric field, E, at the location of the tip (in the narrow channel) is:

$$E_{tip} = E_{electrodes} \cdot \frac{A_{electrodes}}{A_{tip}} \tag{2.7}$$

Where A is the cross-sectional area of the solution in the sample well. $A_{electrodes}$ is the area at the electrode while A_{tip} is the area at fiber tip. A COMSOL simulation of the current density distribution is shown in Figure 8. Under the same electrical field applied, in a well of a traditional 96 well plate set up with two flat electrodes, the current density at the central sensing area is only about one third of the maximum current density on the electrode area. In the contrary, the H shaped well nearly doubled the current density at the central sensing area, while reducing the maximum

current density on the electrodes to less than half of that of the sensing area. Therefore, the H shaped well has a 6 times improvement of the current density ratio between the sensing area and electrodes. Which leaves room for further increasing the electrical field while avoiding excess electrochemical reactions at the electrodes.

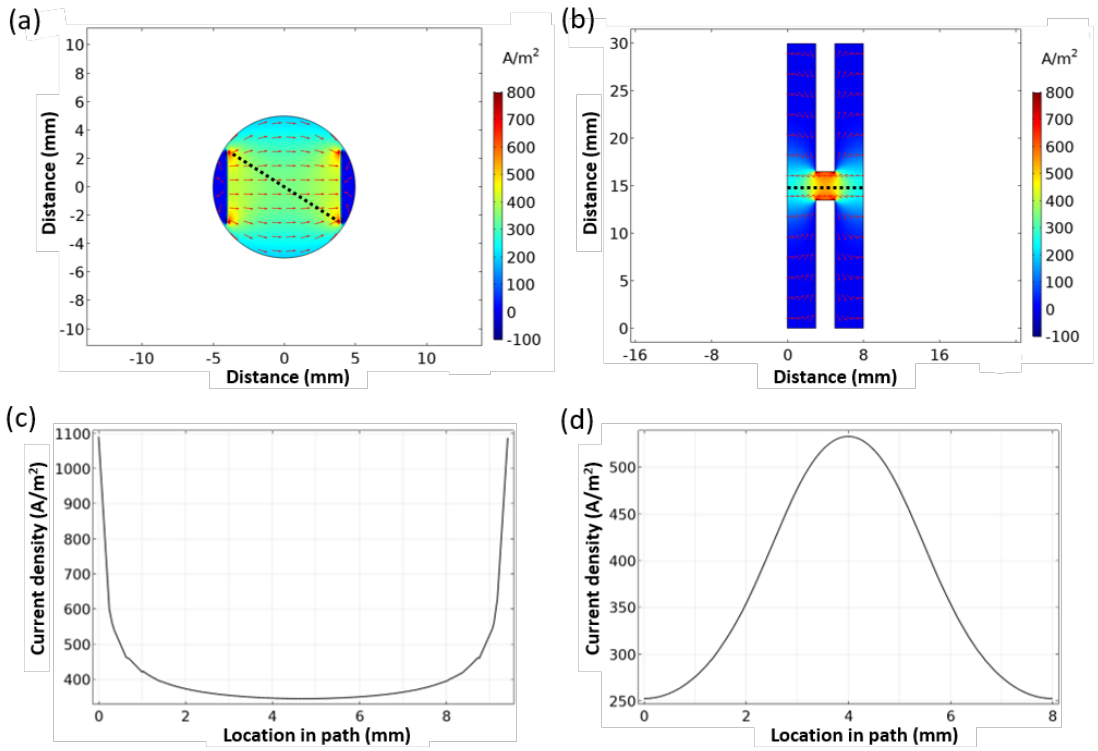

Figure 8. **COMSOL simulation results of current density distribution in two different well designs:** (a) in a well of a standard 96 well plate. (b) in an H shaped well. The red arrows indicate the direction of current density. (c) current density plotted along the black dash line in (a) where the central sensing area has a current density of 350 A/m^2 and the highest current density on electrode is 1100 A/m^2, a ratio of ~ 0.3. (d) current density plotted along the black dash line in (b) where the central sensing area has a current density of 530 A/m^2 and the highest current density on electrode is 250 A/m^2, a ratio of over 2. Therefore, the H shape design shows 6 times increase in the current density ratio between the sensing area and the electrode area. Voltage: 2V, buffer: 1X PBS solution.

To further minimize the side effects of large current density, two pieces of agarose

electrophoresis gel are placed in front of two electrodes separately. The electrophoresis gels offer two benefits: firstly, they prevent the bubbles generated from electrode reactions from entering the sensing area while maintaining the solution conductivity; secondly, they reduce the liquid surface area, providing a more stable liquid surface with less evaporation and fluctuation. In the center of the H shape sample well, a narrow (2 mm by 2 mm) tunnel filled with solution connects the gels and electrodes, providing a higher current density in the center area where the optical fiber is positioned. Therefore, we further increased the current density to 10 times higher by increasing the electrical field, while facilitating faster chemical reactions at the electrodes and producing some gas bubbles, the noise of CSOD measurement is not increased due to the physical blocking provided by electrophoresis gels. For molecular binding studies, the glass fiber tips allow the use of standard silane conjugation chemistry. In this work, the fiber tips were functionalized with 3-Glycidoxypropyldimethoxy¬methylsilane (epoxy), which can spontaneously conjugate to the primary amine groups on protein or virions.

2.3 Materials and Methods

2.3.1 Materials

Multimode optical fibers (125 μm in diameter) were purchased from Thorlabs, Inc. Phosphate-buffered saline (PBS) was purchased from Mediatech Inc. GPR55 (G protein-coupled receptor 55) and ADRB2 (beta-2 adrenergic receptor) HSV-1 virions were engineered using VirD technology[38] and provided by Prof. Heng Zhu and Prof. Prashant J. Desai at Johns Hopkins University. B2 antagonist (CA200693) was

purchased from Hellobio, Tocrifluor was purchased from Tocris. Deionized (DI) water with a resistivity of 18.2 $M\Omega \cdot cm$ filtered through a 0.45 μm filter was used in all experiments. Other chemicals were purchased from Sigma-Aldrich.

2.3.2 Charge-Sensitive Optical Detection Setup

An inverted microscope (Olympus IX-70 with 40X objective) with a CCD camera (Pike F-032, Allied Vision) was used for recording 14-bit grayscale image sequences at a frame rate of 106.5 frames per second (fps). A customized plate with 2 PDMS wells shown in Figure 1 was mounted on a motorized microscope stage (MAC 6000 modular automation controller, Ludl Electronic Products LTD.). Two steel electrodes (1cm x 3cm) were placed 1 cm apart inside the well, then blocked with agarose electrophoresis gel. A green LED (505 nm, 400 mW, Thorlabs M505L3) light was coupled into the fiber via a focusing lens. Fiber is dipped into analyte solution between the electrophoresis gels. To control the fiber and move fiber among the 2 wells, the fiber was clamped to a motorized arm (A-LSQ075B, Zaber). A sinusoidal potential was applied with a function generator (33521A, Agilent). A USB data acquisition card (USB-6229, National Instruments) was used to record voltage and current.

2.3.3 Surface Functionalization

The tip (about 1 cm) of an optical fiber thread (about 20 cm) was first soaked in acetone for 1 minute and then rinsed with DI water and dried. The polymer coating layer on the optical fiber was then stripped off with an optical fiber stripper. The bare fiber was etched by soaking it in 47% hydrofluoric acid for 29 minutes and 15

seconds. The final fiber diameter is about 15 μm. The etched fiber was later rinsed with DI water to wash off the hydrofluoric acid and then blew dried with Nitrogen. The tip was cut to about 9 mm long. Before functionalization, the optical fiber was cleaned with oxygen plasma for 3 minutes.

The etched fiber was soaked in (3-Glycidyloxypropyl)trimethoxysilane (epoxy) solution (2.5% volume percentage of epoxy in isopropanol) for 1 hour for surface functionalization. The fiber was then rinsed with PBS buffer. For BSA-antiBSA binding experiment, the epoxy modified fiber was soaked in 20 $\mu g/mL$ BSA solution (in 1X PBS) for 1 hour. For VirD ligand binding experiment, the epoxy modified fiber was soaked in VirD sample solution (10^7 virions in 1X PBS) for 1 hour.

2.3.4 Fluorescence Image

Fluorescence imaging of the CSOD fiber tip was record-ed with a microscope (Olympus IX-81) with a mercury lamp. The excitation and emission wavelengths were 543 nm and 590 nm for Tocrifluor, and 633 nm and 650 nm for B2 antagonist, respectively.

2.4 Results and Disucssion

2.4.1 Detection Principle Validation

In previous work,[40, 41] it is established that in more diluted buffer solutions (40 times diluted PBS) and lower voltage, fiber oscillation amplitude increases linearly with the increase of applied electrical voltage. To select the correct voltage range in

1X PBS, etched fiber was dipped into 1X PBS solution and the vibration amplitude is measured against different current densities corresponding to different voltages. Figure 9 shows that current density is linearly proportional to the applied voltage. Figure 10 shows that the oscillation amplitude is linearly proportional to the current density for current density smaller than 1000 A/m^2. Figure 11s shows that the noise level is relatively stable but start to increase at very high current density, which is likely caused by bubble-generated mechanical noises due to the excess reactions at the electrodes. To achieve maximum signal to noise ratio, the current density was controlled at around 1000 A/m^2, corresponding to voltage at 20V.

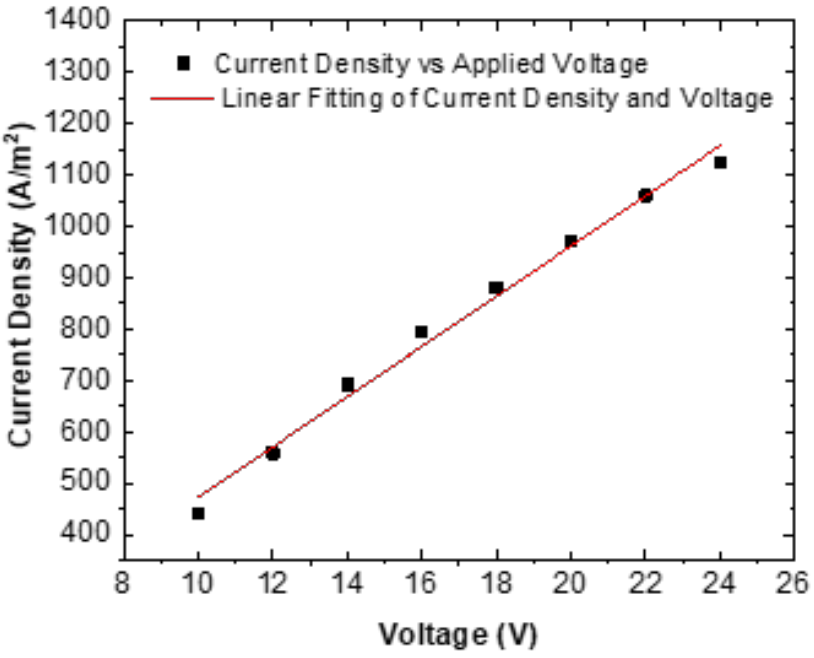

Figure 9. **Current Density change vs. applied electrical field voltage.**

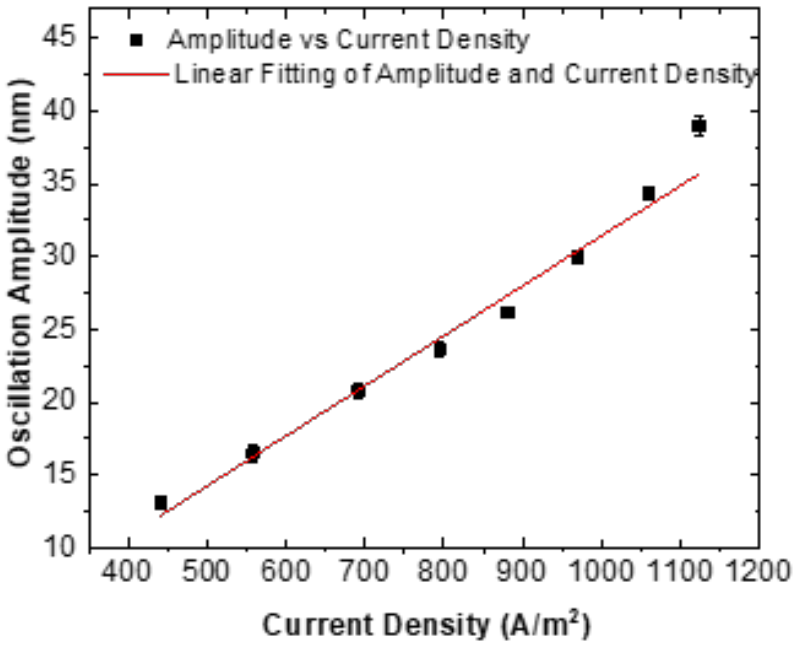

Figure 10. **Validation of the detection principle.** Fiber oscillation amplitude vs. current density at 35Hz, the black dots are the experiment data and the red line is the linear fit. Error bars are the calculated standard deviation of measurements under each current density. Fiber diameter: 14 μm, length: 8.5 mm. Buffer: 1X PBS buffer.

2.4.2 Detection of Large Molecules

To demonstrate the detection of large molecules, we modified the fiber surface with bovine serum albumin (BSA) and studied the binding kinetics of BSA antibody (anti-BSA) to BSA. The result is shown in Figure 12. BSA modified fiber tip was initially dipped into a well containing 1X PBS. Its oscillation amplitude was recorded over time as baseline test. Next, 10 μL of additional PBS was injected as a negative control. It was observed that the change of amplitude upon buffer introduction is within the noise level. Later 10 μL of 0.42 $\mu g/mL$ anti-BSA was injected into the

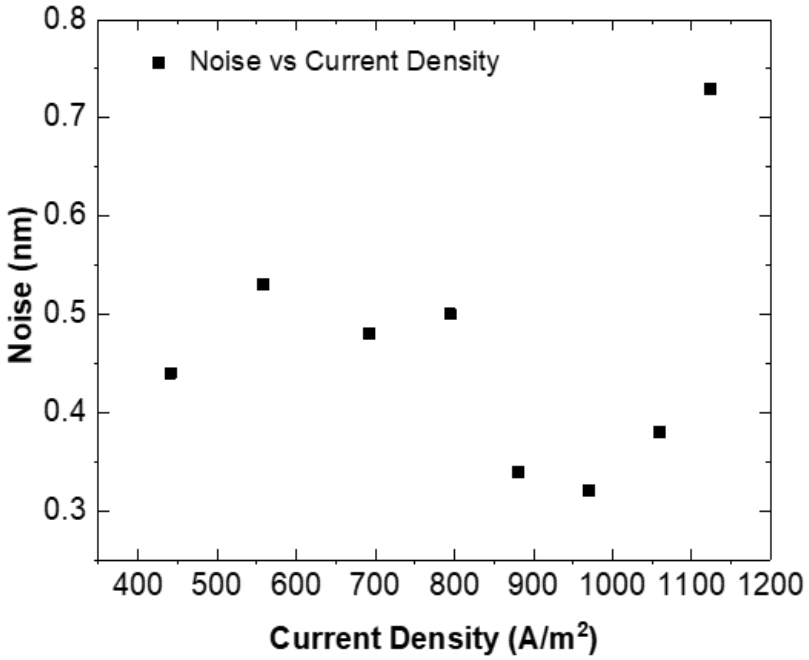

Figure 11. **Fiber oscillation noise level.** Noise level, defined as standard deviation of oscillation amplitude in one-minute duration, as a function of current density. Fiber diameter: 14 μm, length: 8.5 mm. Buffer: 1X PBS buffer.

well resulting in an anti-BSA concentration of 0.2 nM. The isoelectric point (pI) of BSA is around 5,[55] so the BSA coated fiber is negatively charged in PBS buffer. Anti-BSA with pI between 4.8 and 5.2 [56] is also negatively charged in PBS buffer. Therefore, the binding of anti-BSA to the BSA functionalized fiber probe increases the net negative charges on the fiber, resulting in increased oscillation amplitude, and eventually reached a stable state after the binding reach equilibrium. The result is comparable with that obtained in 40 times diluted PBS.[39]

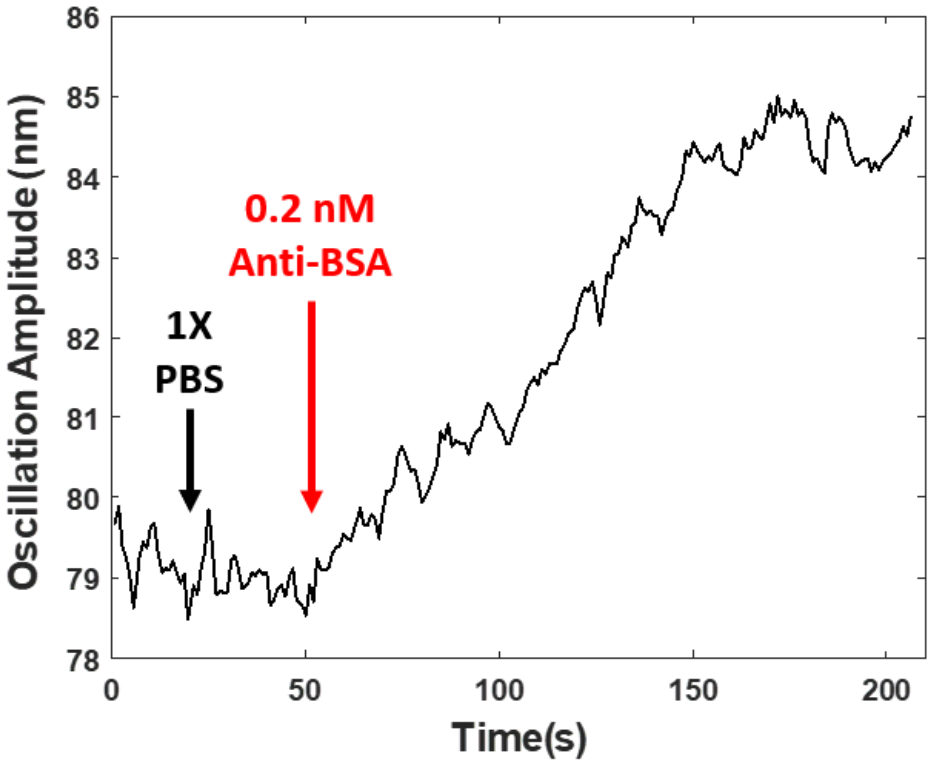

Figure 12. **Protein detection. Anti-BSA binding onto BSA-modified fiber surface.** The black arrow marks the addition of 10 μL 1X PBS buffer, the red arrow marks the addition of μL of 0.42 $\mu g/mL$ anti-BSA (in 1X PBS buffer) leading to a final concentration of 0.2 nM. Fiber diameter: 17 μm, length: 8 mm.

2.4.3 Quantification of Small Molecule Binding Kinetics to Large Membrane Protein Complex

To demonstrate small molecule detection capability in normal buffer with CSOD technology, we studied the binding kinetics between small molecule ligands and membrane protein displayed on virion surface in 1X PBS. Specifically, HSV-1 virion displayed G-protein coupled receptor (GPCR) ADRB2 and GPR55 were used.[38] ADRB2 binds adrenaline and mediates physiologic responses such as smooth muscle relaxation and bronchodilation41.The orphan receptor GPR55 is a novel cannabinoid

receptor with therapeutic potentials [57].The VirD technology provides a native-like microenvironment for GPCR, but the virion has a very large mass (around 200 MDa), and thus, the relative mass change caused by binding of a small molecule ligand (<1 kDa) is very small, with about 1000 copies of GPCR per virion coverage on average, the mass change assuming complete binding is less than 0.5%, which is a challenge for mass sensitive technologies. Although charge-based detection of small molecule binding to VirD GPCR has been realized by us recently with VirD oscillator technology,[58] it was measured in low ionic strength buffer that differs from physio-logical condition, which may alter the binding kinetics.

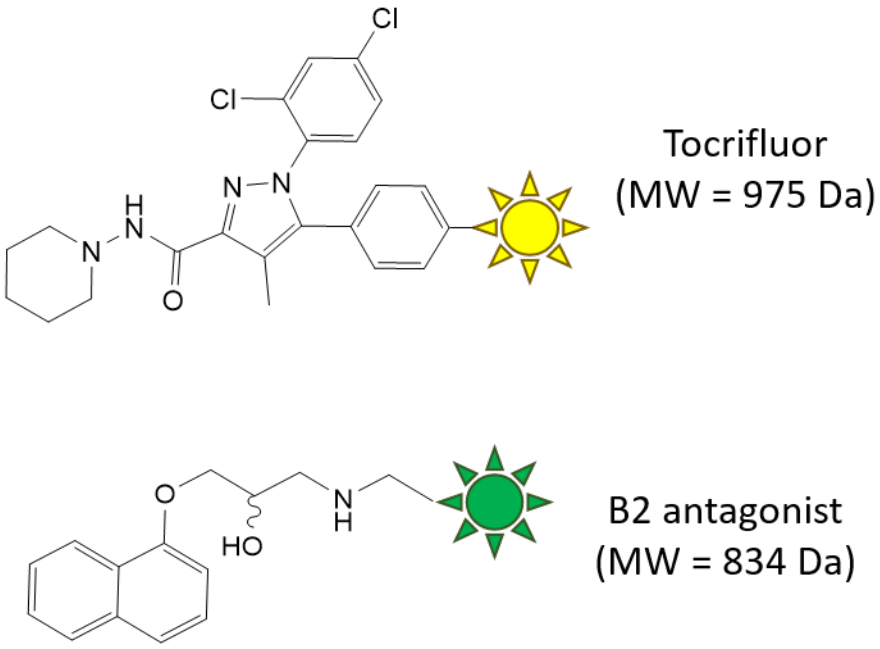

Figure 13. **Structure of small molecules.** Structures of B2 antagonist and Tocrifluor with fluorescent tags.

Virions are functionalized to fiber surface via epoxy coupling, and the binding of respective small molecule antagonists B2 antagonist and Tocrifluor are studied in 1X

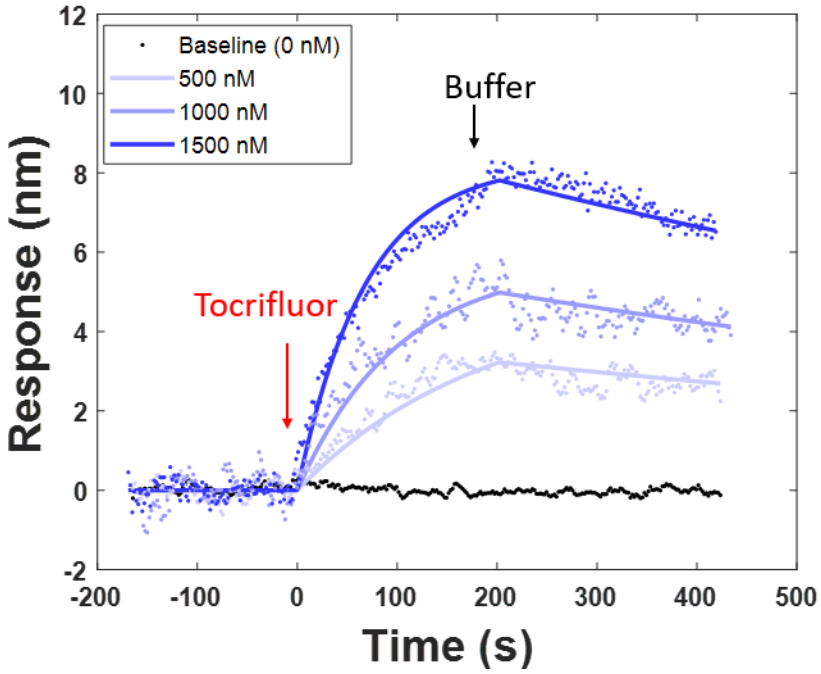

Figure 14. **Measure Tocrifluor small molecule binding kinetics to GPR55 expressed VirD.** CSOD measurements of GPR55-Tocrifluor binding kinetics. Solid lines are global fitting of data to first-order kinetics.

PBS. The structures of the fluorescent tagged molecules are shown in Figure 13. First, the virions modified fiber tip was dipped into one well filled with 1X PBS buffer to establish a baseline. Subsequently, the fiber tip was switched from the buffer well to a sample well containing ligands to measure the binding or association process. At last, the fiber tip was switched back to the buffer well for dissociation studies. Figure 14 shows the kinetic curves for GPR55 virions binding to three concentrations of Tocrifluor and a baseline with no Tocrifluor added. Solid lines are global fitting of the data with a first-order kinetic model. Figure 15 shows the kinetic curves of B2 antagonist binding to ADRB2 virions and the corresponding global fitting curves. For both binding pairs, when no ligand is introduced, the baseline level is within the noise level, showing that the oscillation amplitude change was caused by the specific binding between the ligands and their corresponding receptors. The specificity was

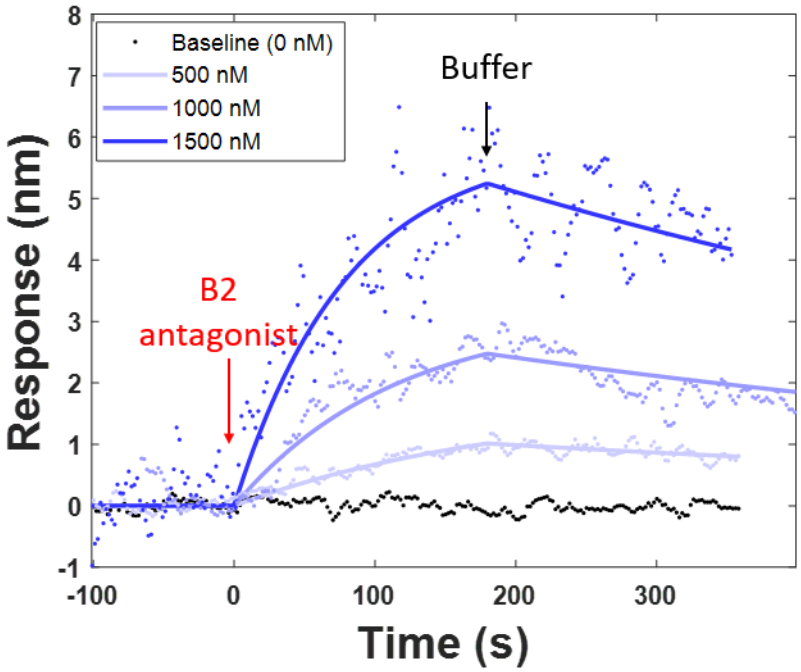

Figure 15. **Measure B2 antagonist small molecule binding kinetics to ADRB2 expressed VirD.** CSOD measurements of ADRB2-B2 antagonist binding kinetics. Solid lines are global fitting of data to first-order kinetics.

further confirmed by including an empty virion, K082 as negative control, which does not have any GPCR displayed. As shown in Figure 16, K082 binds to neither B2 antagonist nor Tocrifluor.

By fitting the kinetic curves at different concentrations globally with first-order kinetics using Scrubber (BioLogic Software Pty Ltd), the association rate constants (k_a), dissociation rate constants (k_d) as well as equilibrium constants (K_D) for both binding pairs were calculated. For Tocrifluor binding to GPR55 receptor, the kinetic constants determined from global fitting were $k_a = (9.2 \pm 0.2) \times 10^3\ M^{-1} \cdot s^{-1}$, $k_d = (8.1 \pm 0.3) \times 10^{-4}\ s^{-1}$, $K_D = 89 \pm 4\ nM$. For B2 antagonist binding to ADRB2 receptor, $k_a = (7.5 \pm 0.5) \times 10^3\ M^{-1} \cdot s^{-1}$, $k_d = (1.4 \pm 0.3) \times 10^{-3}\ s^{-1}$,

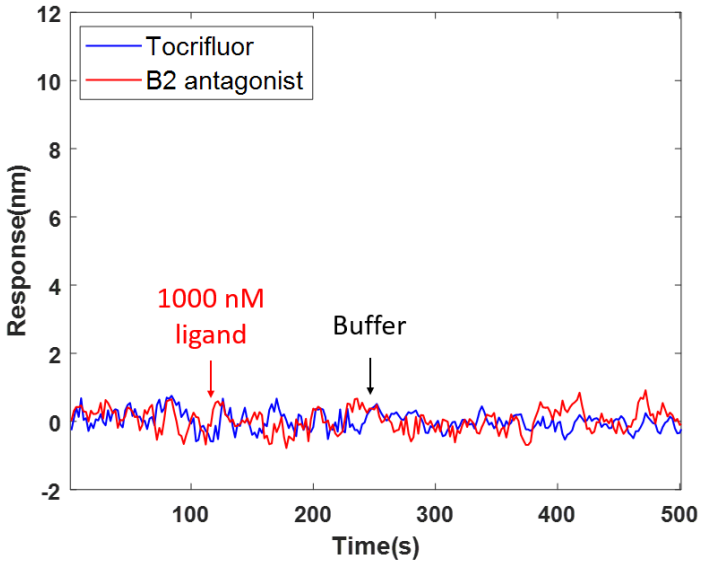

Figure 16. **Negative control of small molecules binding to VirD.** (Negative control experiment with K082 modified fiber, red arrow marks the moment of the fiber switching from buffer well to a well containing 1000 nM ligand, black arrow marks the moment of the fiber switching back to the buffer well.

$K_D = 189 \pm 10\ nM$. The $\pm$ error ranges represent standard deviation of the fitting result.

Fluorescence imaging was used to cross validate the binding events, since the two small molecule ligands are fluorescently tagged. For each binding pair studied, after kinetics studies, the fiber tips were then soaked in ligand solution again to allow association of the fluorescent tagged ligands. After which the fluorescent images were taken. Figure 17 shows the bright field image of GPR55 and ADRB2 modified fibers, the fluorescent images of the modified fibers, and the fluorescent images of fibers after their corresponding ligands are introduced. The normalized fluorescent intensities of the fibers are plotted in Figure 19a. Figure 18 shows the bright field image of negative control, empty VirD K082 modified fiber, the fluorescent image of the modified fiber, and the fluorescent images of the fiber after ligands are introduced.

Normalized fluorescent intensities are also plotted as shown in Figure 19b. The results clearly show that only the specific binding between the two ligand and receptor pairs produce visible fluorescence image on the fiber, while the empty virion without the receptors show no visible emission upon interaction with both ligands.

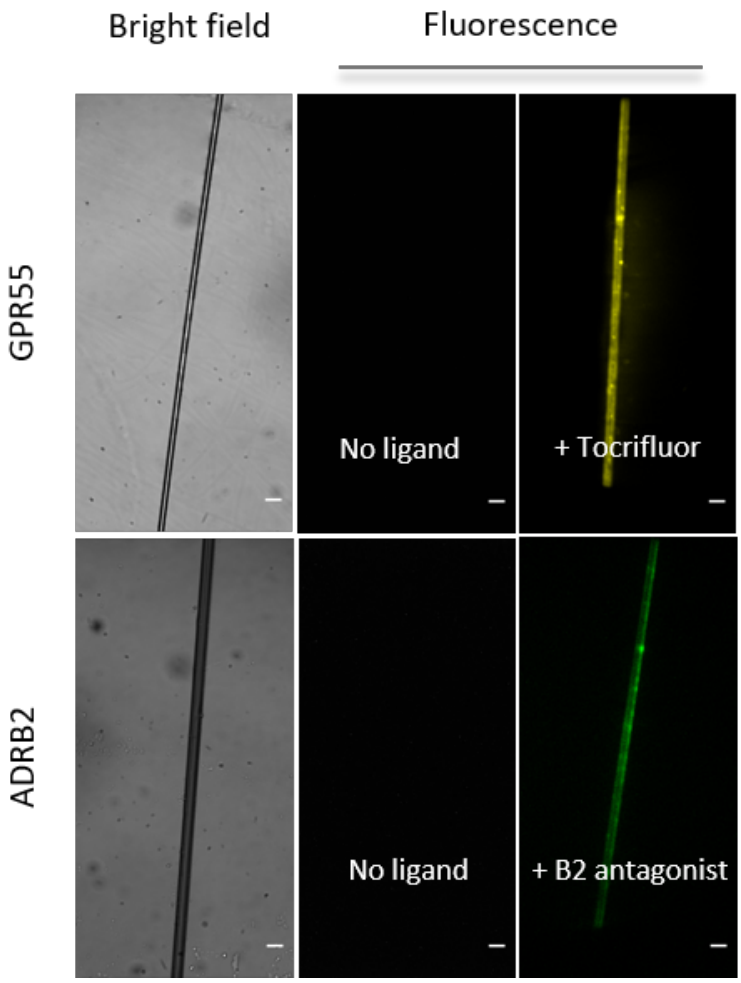

Figure 17. **Fluorescent confirmation of small molecules binding to VirD.** Bright field and fluorescent images of virions modified fibers and small molecule associated fibers. (b) Bright field and fluorescent images of negative control virions K082. (c) Normalized fluorescent intensities of GPR55 and ADRB2 modified fibers compared with Tocrifluor and B2 associated fibers. (d) Normalized fluorescence intensities of K082 modified fibers compared with ligands introduced intensities.

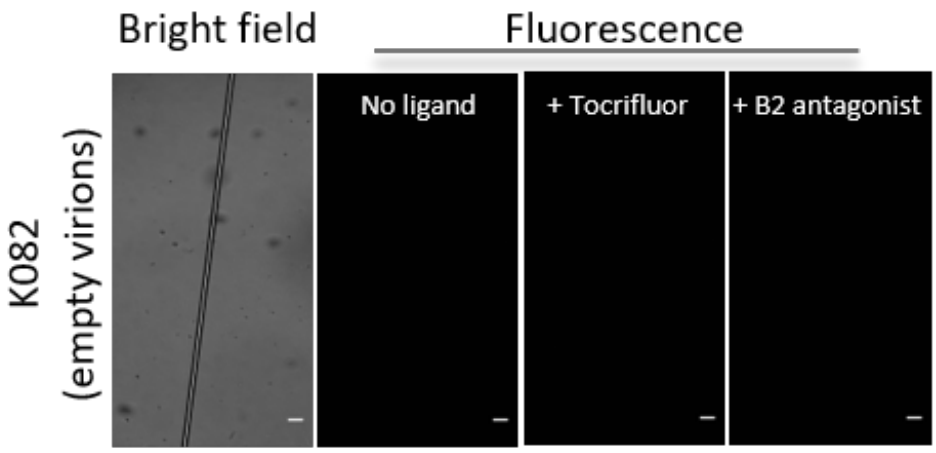

Figure 18. **Negative control experiment of fluorescent images of control virions K082.** Bright field and fluorescent images of negative control virions K082.

2.4.4 Impact of Buffer Ionic Strength on Binding Kinetics

To study the impact of buffer ionic strength on the binding kinetics, the binding results in 1X PBS are compared with results measured in a more diluted buffer solution (40 times diluted 1X PBS) for the same experiments are performed with ADRB2-B2 antagonist pair. As shown in Figure 20, the solid lines show the global fitting of the data with first-order kinetic model. Kinetic constants given by global fitting were $k_a = (8.4 \pm 0.4) \times 10^3\ M^{-1} \cdot s^{-1}$, $k_d = (2.8 \pm 0.5) \times 10^{-3}\ s^{-1}$, $K_D = 337 \pm 11\ nM$. This K_D value is very close to the virion-oscillator result of $420 \pm 27\ nM$, which was also measured in low ionic strength buffer,[48] and are higher than the value measured in 1X PBS buffer ($189pm10\ nM$). Similarly, for Tocrifluor/GPR55 pair, the K_D measured in diluted buffer by VirD oscillator method was $160 \pm 50\ nM$, also nearly double than CSOD measured value in 1x PBS ($89 \pm 4\ nM$). It has been reported that ionic strength affect the binding affinity if the interaction involves electrostatic interactions.[47] Both of the GPCRs binding pairs we measured involves electrostatic

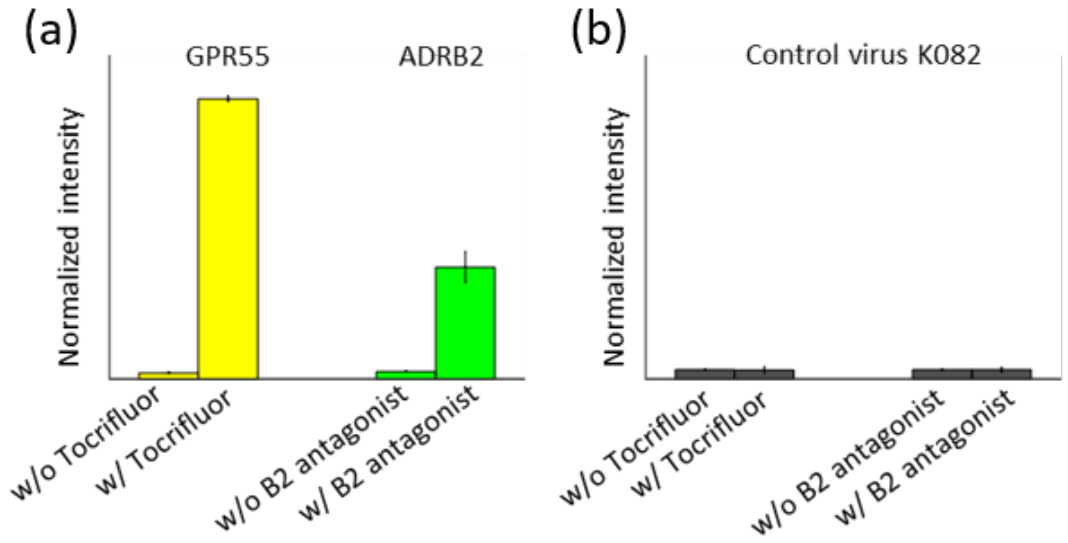

Figure 19. **Normalized florescent intensities of different experiment groups.** (a) Normalized fluorescent intensities of GPR55 and ADRB2 modified fibers compared with Tocrifluor and B2 associated fibers. (b) Normalized fluorescence intensities of K082 modified fibers compared with ligands introduced intensities.

interactions, since the reported binding site of GPR55 is hydrophilic,[59] and ADRB2 is partially hydrophilic.[60] In addition, ionic screening effect also affect local pH value near the sensor surface [61], which could also affect protein conformation and binding kinetics. Thus, it is not surprising that the affinity measured under normal and diluted PBS are different. Our results confirm that buffer ionic strength does have an impact to the binding kinetics, and therefore, the realization of charge-based detection in normal buffer is important for accurate and unbiased measurement of molecular binding kinetics.

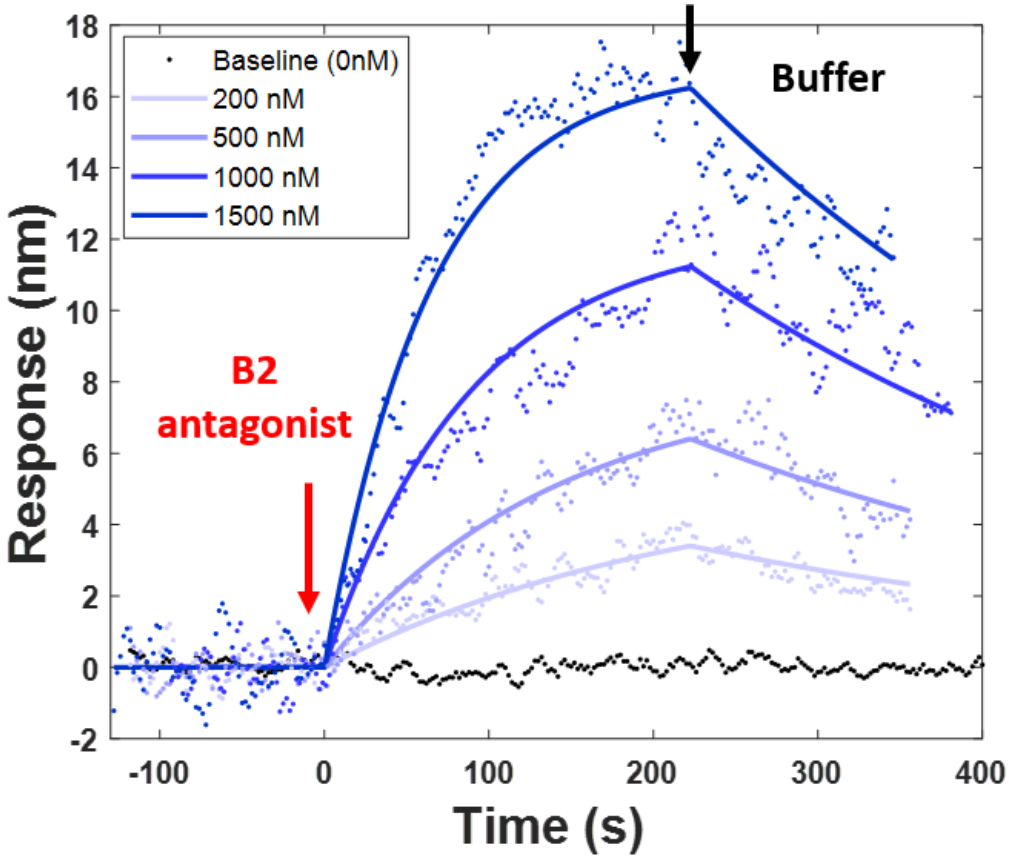

Figure 20. **CSOD measurements of ADRB2-B2 antagonist binding kinetics.** Dots are raw data and solid lines are global fitting to the first-order kinetics.

2.4.5 Signal Intensity and Optimization of Well Geometry

Note that the due to the strong ionic screening effect in normal ionic strength buffer, the signal intensity in our proof of concept setup is reduced to about half of the measurement in low ionic strength buffer while the noise remains at similar level. The signal intensity can be further improved by optimizing the well geometry, so that higher field can be applied without introducing excessive electrode reactions. Figure S4 shows simulation result of an improved well design with fan shape geometry that further increased the ratio of current density between the sensing area and electrodes

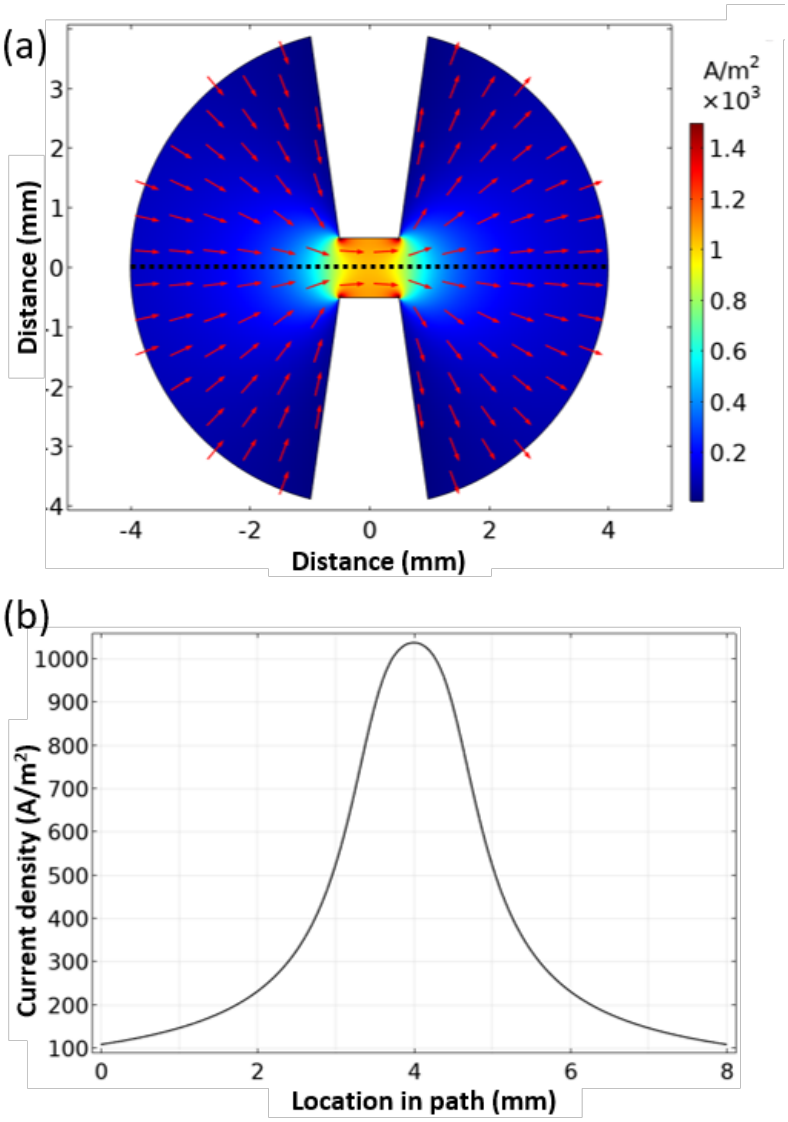

Figure 21. **COMSOL simulation results of an improved well design.** (a) current density distribution in a fan shape well. The red arrows indicate the direction of current flow. (b) current density plot along the center black dash line in (a), where the central sensing area has a current density over $1000A/m^2$, while the maximum current density at the electrode is reduced to $\sim 100A/m^2$, a ratio of 10. Therefore, compares to the H-shaped design, this fan shape design will improve another 5 times on current density ratio between the sensing area and electrodes. Voltage: 2V, buffer: 1X PBS solution

to about 10, which is 5 times higher than the H-shaped well used in the current setup. Since the signal scales with current density, while the noise remains flat as long as the electrode reaction is under control, a 5 times improvement in signal to noise ratio is expected from this design, which will exceed the CSOD performance in low ionic strength buffer measured in a regular microplate. In addition, the size of fan shape well is still comparable to a single well in the 96-well microplate. In the future, a custom designed multi-well plate with optimized well geometry will be developed for multiplexed high-throughput study.

2.4.6 Detection Limit

The noise in the oscillation amplitude of fibers is about 0.25 nm (averaged over 10 s) as shown in Figure 22[40]. In terms of charge density, the detection limit is 0.25 electrons per μm^2. Here detection limit is defined as three times the noise level. It is then calculated that for anti-BSA to BSA binding in 1X PBS, the detection limit of anti-BSA molecules is $\sim 3.75\ molecules/\mu m^2$, or 933 fg/mm^2 based on the effective charge and molecular weight of anti-BSA. However, while this is a useful estimation, some molecules, such as Tocrifluor measured above, is not charged, CSOD detects the effective surface charge changed induced by conformation change upon binding. In this case, it is hard to estimate the detection limit in terms of molecule density. Besides, it is convenient to provide detection limit in terms of lowest detectable molar concentration in kinetics measurement applications. The lowest detectable molar concentration depends upon several significant experimental factors such as the binding affinity, binding kinetics of the analyte, and the surface coverage of the capture molecules. Here, we estimate the empirical detection limit in terms of kinetics

constants based on:

$$R_{eq} = \frac{[L]R_{max}}{[L] + K_D}$$

Where $[L]$ is the ligand concentration, R_{eq} is the response at equilibrium under this ligand concentration, $R_m max$ is the total surface binding capacity, and K_D is the dissociation constant. R_{max} and K_D can be calculated based on experimental results. Based on this, the empirical detection limit in terms of molar concentrations can be estimated for molecules of interest. For example, for anti-BSA to BSA binding, CSOD can detect anti-BSA concentration as low as 24 pM, for Tocrifluor, the detection in terms of molar concentration os 17 nM, and for B2 antagonist, the detection limit is 226 nM.

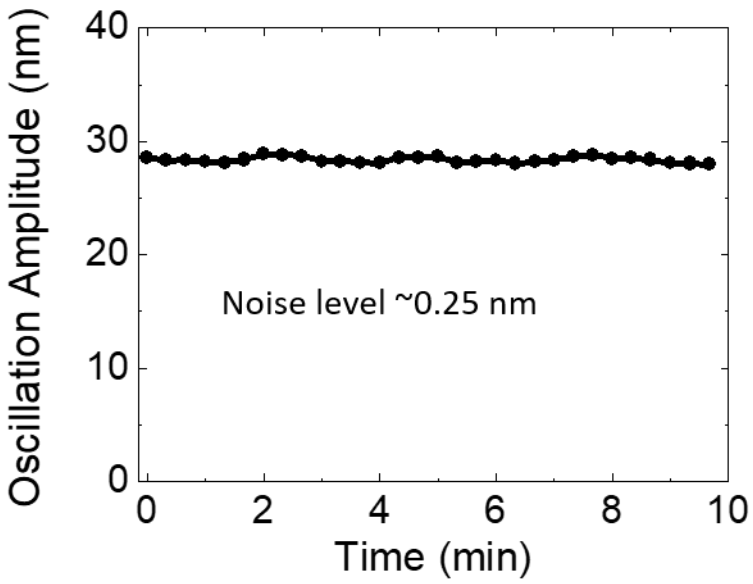

Figure 22. **Detection limit and noise analysis.** The root-mean-square of the noise level in the amplitude is 0.25 nm.

For an estimation of detection limit and dynamic range in terms of kinetics rate constants k_a, k_d and K_D, while there are many factors related, we can achieve a rough

estimation based on the systems noise level and time resolution. For CSOD system, time resolution is 1 s, and the noise level is 0.25 nm as mentioned above. Based on this and first order kinetics model, first the range of k_d is calculated. To calculated the lower range of k_d measurable, the following equation is used:

$$ln(\frac{R_0}{R_t}) = k_d(t - t_0)$$

Where R_t is the response at time t, R_0 is the response at dissociation starting time t_0. The CSOD system can measure stably for up to 20 minutes, and a reasonable assumption for R_0 for binding pairs' average maximum binding signal is about 10 nm. If within 20 minutes, the signal does not drop more than 0.75 nm (3 times the noise level), then the dissociation will be unmeasurable. From this, the lower boundary of measurable k_d is calculated to be $6 \times 10^{-5}\ s^{-1}$. The upper boundary of k_d should be calculated based on the time resolution of the CSOD system (1 s). Based on this time resolution, if the half-life of dissociation stage is less than 1 s, it becomes unmeasurable, which gives the upper limit of k_d as $0.7\ s^{-1}$. Therefore, the detection range for k_d is between $6 \times 10^{-5}\ s^{-1}$ and $0.7\ s^{-1}$

To estimate the detection range for k_a, the following equation is used:

$$R_t = R_{eq}(1 - e^{-(k_a[L]+k_d)(t-t_0)})$$

Where R_{eq} is the equilibrium response, $[L]$ is the ligand concentration. Assuming again an average R_{eq} of 10 nm, the detection limit is 0.75 nm, and the stable measurement time is still 20 minutes. For a given kinetics study, usually it is preferred to measure ligand concentration at around K_D, for most binding pairs especially involving small molecules, it is reasonable to assume that $[L] = 100\ nM$. The calculated lower limit for k_a is $50\ M^{-1}s^{-1}$. The upper limit of k_a is also related to time resolution, assuming that R_t reaches half of R_{eq} within a second, the upper limit of k_a can be

calculated to be $7 \times 10^6\ M^{-1}s{-}1$. Therefore, the detection range for k_a is between 50 $M^{-1}s^{-1}$ and $7 \times 10^6\ M^{-1}s^{-1}$.

Based on the above calculations, the detection range for K_D can be calculated using:

$$K_D = \frac{k_d}{k_a}$$

The measureable range for K_D is caculated to be: $85\ pM < K_D < 14\ mM$.

2.5 Conclusion

We developed a CSOD system with enhanced electrical field at the sensing area that allows the charge sensitive optical detection carried out in normal buffer for the first time. We demonstrated the system's capability on the detection of both large and small molecules, including quantification of binding kinetics of small molecule ligands and virion displayed GPCRs. We further compared the binding kinetics measured in normal and diluted buffer and found that the diluted buffer reduced the affinity of the bound pair, likely due to the increased electrostatic repulsion force between the negatively charged ligands and receptors. The capability of measure in normal buffer will also favor the adoption of charge sensitive detection technology for broader applications.

Chapter 3

CHARGE-SENSITIVE OPTICAL DETECTION WITH LARGE FIBER TO INCREASE SIGNAL-TO-NOISE RATIO

3.1 Introduction

During the course of research in CSOD, it came to our attention that long term stability has been an issue in CSOD measurements, the low frequency noise at the scale of kinetics interaction has been persistent. For example, in last chapter, where small molecule to virion binding was measured (Figure 23a), or in previously published experiments as shown in Figure 23b and 23c[40, 41].

In this chapter, we focus on optimization of the CSOD system toward higher stability and signal to noise ratio. From previous chapter, it was shown (Equation 2.1) that the fiber oscillation amplitude is related to electric field strength, frequency, surface charge density, and fiber dimensions (length and diameter), the relationship is given by

$$x = \frac{2\pi \left|\overrightarrow{E(\omega)}\right| \sigma r l}{\sqrt{(k_{eff} - m_{eff}\omega^2)^2 + (c\omega)^2}} \tag{3.1}$$

where $\left|\overrightarrow{E(\omega)}\right|$ is the electric field strength, c is the damping coefficient, and k_{eff},m_{eff},r and l are the effective spring constant, mass, radius and length of the optical fiber, respectively. The effective spring constant, k_{eff}, of the cylindrical optical fiber is given by[40]:

$$k_{eff} = \frac{3\pi E r^4}{4l^3} \tag{3.2}$$

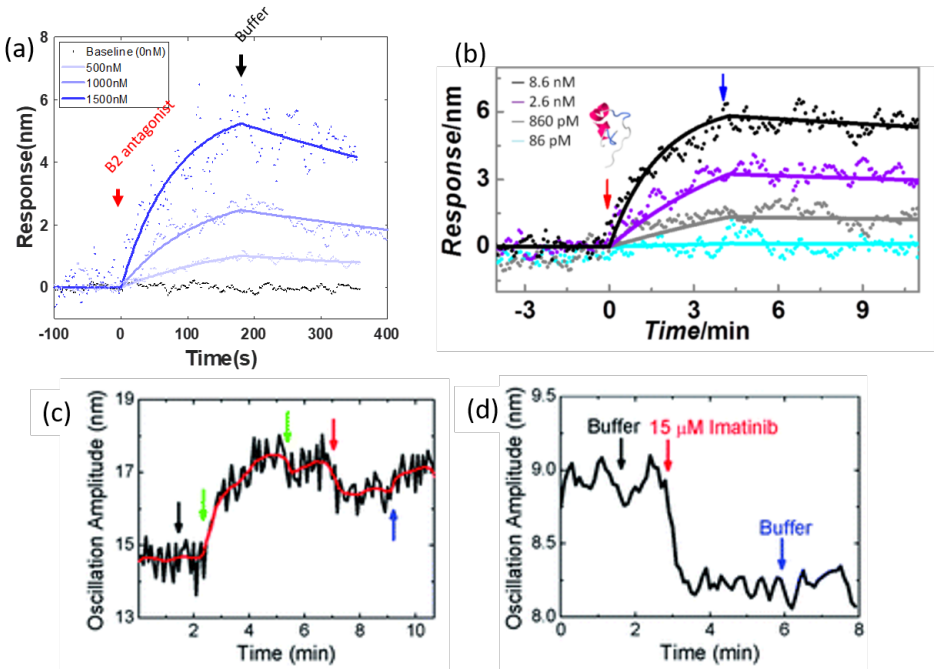

Figure 23. **Low frequency noise in CSOD.** (a) CSOD measurement of B2 antagonist binding to ADRB2 expressed virions. (b) CSOD measurement of KcsA-Kv1.3 Nanodisc-ShK binding. (c) CSOD measurement of inhibition of c-Abl with AMP-PNP (green arrows), exposure of the inhibited c-Abl to imatinib (red arrow), and positive control.

where E, r and l are the Young's modulus, radius and length of the optical fiber, respectively. The electric field applied is frequency dependent, given by

$$\left|\overrightarrow{E(\omega)}\right| = \left|\overrightarrow{E_0}\right| \frac{R_S}{R_S^2 + \frac{1}{(\omega C_{eff})^2}} \tag{3.3}$$

where R_S and C_{eff} are the solution resistance and effective interfacial capacitance respectively.

From the above equations, it is obvious that the oscillation amplitude is both frequency dependent and fiber dimension dependent. For example, it was shown previously that for a fiber with diameter of $11\mu m$ and length of $10mm$, the fiber oscillation can be measured against frequency and the experiment data fits with Equation 3.1 very closely (Figure 24[40]). This means that for a fiber with a smaller

diameter (around $15\mu m$), the optimal frequency where fiber oscillates at maximum amplitude is usually low ($< 60Hz$). However, from a noise spectrum analysis shown in Figure 25, where no electric field was added, it is obvious that there are many sources of noise in the lower frequency region, these noises could be coming from mechanical noises of the system, or electric noises in the data collection system. It is optimal to move the signal frequency to a higher frequency range and avoid the low frequency noise. To overcome these challenges and achieve higher frequency signal, we used larger diameter fiber to achieve higher resonance frequency, and we have replaced the camera with a high speed photo detector. By implementing those changes, we have optimized the CSOD detection methods to increase the signal to noise ratio (SNR) and moved toward high-throughput detection.

3.2 Methods

3.2.1 Materials

Multimode optical fibers (125 μm in diameter, FG105UCA, Thorlabs) were purchased from Thorlabs, Inc. Phosphate-buffered saline (PBS) was purchased from Mediatech Inc. Deionized (DI) water with a resistivity of 18.2 $M\Omega \cdot cm$ filtered through a 0.45 μm filter was used in all experiments. Other chemicals were purchased from Sigma-Aldrich.

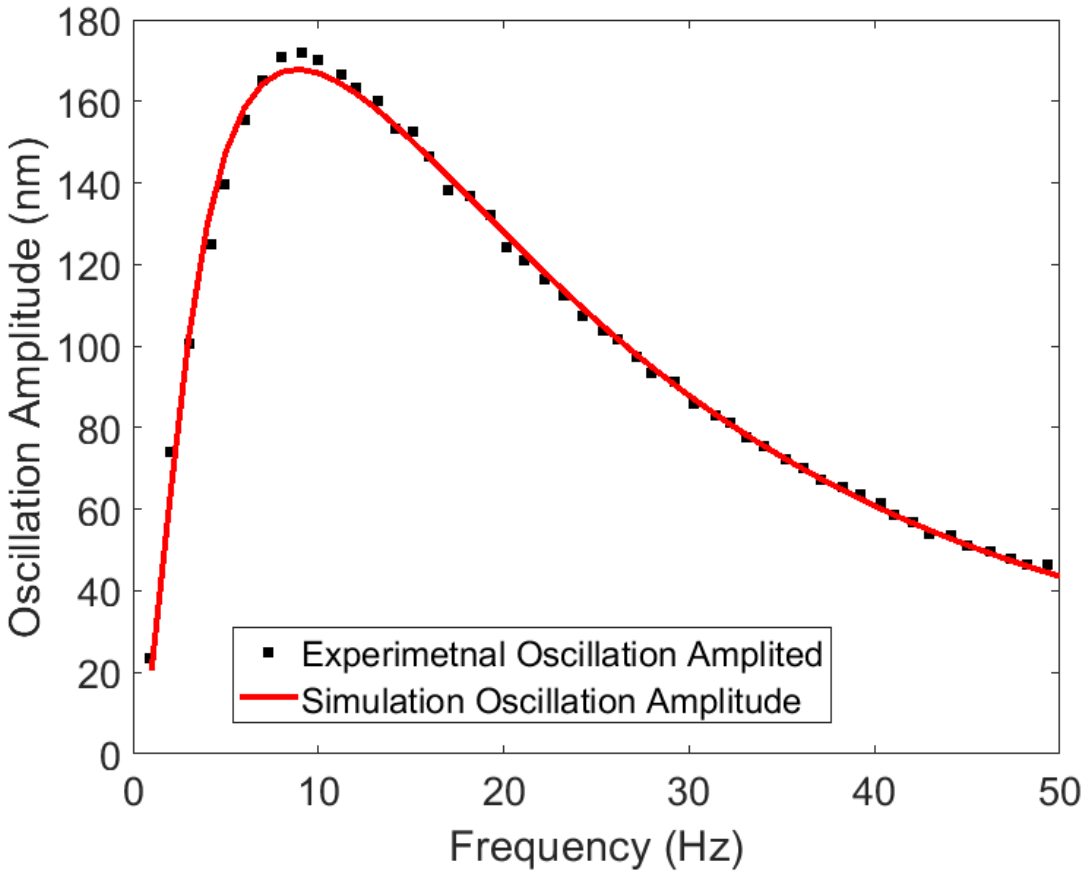

Figure 24. **Fiber oscillation amplitude vs. frequency.** The black dots are experimental data and the red line is the prediction of eqn 3.1. Fiber diameter: 11 μm, length: 8.5 mm. Buffer: 40 times diluted 1X PBS buffer.

3.2.2 Charge-Sensitive Optical Detection Setup

An inverted microscope (Olympus IX-70) with 40X and 10X objective, and a quadra-cell position sensitive photodetector (PDQ80A, Thorlabs) was used for CSOD detection. A 96-well microplate with a pair of steel electrodes (1 cm $\times$ 0.6 cm, 0.8 cm distance) inside the wells were mount on a motorized microscope stage (BioPrecision2, Ludl Electronic Products LTD., Hawthorne, NY). Light from a laser (532 nm, 20 mW, Prometheus, Coherent, Santa Clara, CA) or a green LED (505 nm, 400 mW,

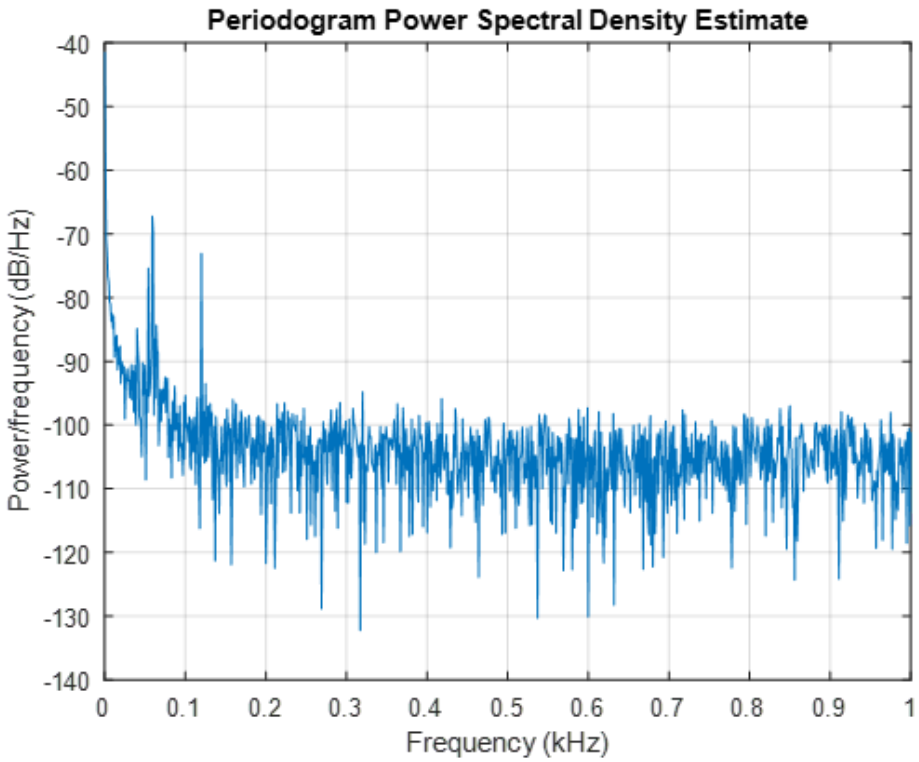

Figure 25. **CSOD system noise analysis.** Image of fiber tip collected at 2000 frames per second without electric field added.

Thorlabs M505L3) was coupled into the fiber via a focusing lens. was coupled into the fiber via an objective lens (2X, NA 0.06, Olympus). To move the fiber probe between wells, the fiber was clamped to a motorized arm (A-LSQ075B, Zaber) to lift the fiber up and down. A sinusoidal potential was applied with a function generator (33521A, Agilent). A USB data acquisition card (USB-6228, National Instruments) was used to record the output of the photodetector.

3.2.3 Surface Functionalization

The tip (about 1 cm) of an optical fiber thread (about 20 cm) was first soaked in acetone for 30 seconds and then rinsed with DI water and dried. The polymer

coating layer on the optical fiber was then stripped off with an optical fiber stripper. The bare fiber was etched by soaking it in 47% hydrofluoric acid for 30 seconds for a diameter of $\sim 120\mu m$. The etched fiber was later rinsed with DI water to wash off the hydrofluoric acid and then blown dried with Nitrogen. The tip was cut to about 9 mm long. Before functionalization, the optical fiber was cleaned with oxygen plasma for 3 minutes.

The etched fiber was soaked in (3-Glycidyloxypropyl)trimethoxysilane (epoxy) solution (2.5% volume percentage of epoxy in isopropanol) for 1 hour for surface functionalization. The fiber was then rinsed with PBS buffer. For BSA-antiBSA binding experiment, the epoxy modified fiber was soaked in 20 $\mu g/mL$ BSA solution (in 1X PBS) for 1 hour.

3.3 Results

3.3.1 Detection Principle

To validate the detection principle, it is essential to examine equation 3.1. According to eqn 3.1, the oscillation amplitude is Frequency dependent. Figure 26 plots a frequency of the oscillation amplitude of a fiber with length $l = 9.8\ mm$ and diameter $d = 105.6\ \mu m$, which shows a broad peak near 600 Hz, with calculated $k_eff = 4.5\ N \cdot m^{-1}$, $m_{eff} = 166\ ng$ and fitting parameter $c = 1.3 \times 10^{-4} N \cdot m^{-1}$. Compared to the fiber with $d = 11\ \mu m$ shown in Figure 25 which has a peak at near 10 Hz, with calculated larger diameter fiber moves the signal frequency to higher frequency region and away from the low frequency noise.

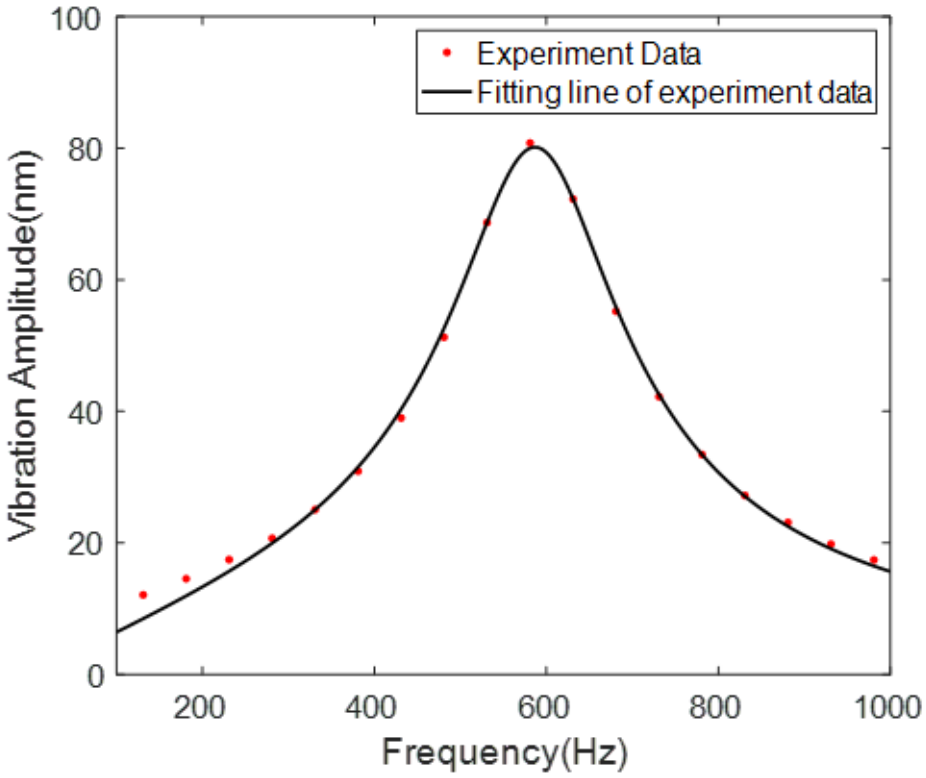

Figure 26. **Large Fiber oscillation amplitude's frequency dependency** The black dots are experimental data and the red line is the prediction of eqn 3.1. Fiber diameter: 105.6 μm, length: 9.8 mm. Buffer: 40 times diluted 1X PBS buffer

3.3.2 Long term stability

To test the long term stability of larger diameter fiber compared with smaller diameter fiber, a small fiber with diameter 13.8 μm and length of 9.0 mm, and a large fiber with diameter 112.0 μm and length of 10.0 mm were used. Bare fiber vibration in pH=10 NaOH solution was tested for 10 minutes. As shown in Figure 27, the average signal for small fiber is 24.96 nm with noise (calculated from the standard deviation of all the data points) of 0.51 nm, while the average signal for large fiber is 44.33 nm and noise is 0.25 nm, the SNR increase from $\sim$ 49 to $\sim$ 177, with a

4-fold increase. When considering the long term stability, low frequency drift had been an issue in CSOD measurement, as can be seen in Figure 27a, there are some low frequency noise in the curve. As shown in Figure 25. When using a large fiber as shown in Figure 27b, the low frequency noise is significantly less.

3.3.3 Calibration of quandrant-cell detector

A quadra-cell position sensitive photodetector (PDQ80A, Thorlabs) and a CMOS camera (Mikrotron EoSens 3CXP) was used for data collection. The displacement of the optical fiber was calibrated using the following procedure. A region of interest (ROI) including the image of the fiber tip was selected as shown in Figure 5. The ROI was divided into A and B, and then shifted by using a piezo stage to mimic the fiber movement (Figure S2a). For data collection on quadrant-cell detector as shown in Figure 28, the differential intensity at each position was determined by the detector output. The differential response is calculated as:

$$\begin{aligned} Response &= \frac{(Q1+Q3)-(Q2+Q4)}{(Q1+Q3)+(Q2+Q4)} \\ &= \frac{X_A - X_B}{X_A + X_B} \end{aligned}$$

where Q1, Q2, Q3, and Q4 are quadrant-cell detector outputs from the 4 cells respectively, X_A and X_B are outputs from 2 regions of interests. From the data collected. Figure 29a plots the differential intensity vs. fiber position, which shows a linear relation in the dynamic range which serves as the calibration curve, while Figure 29b plots the differential signal vs. fiber position for quadrant-cell detector. From the results, it is obvious that camera has a larger dynamic range but they have similar sensitivity, with camera having a calibration factor (slop of curve) of 1.7 and

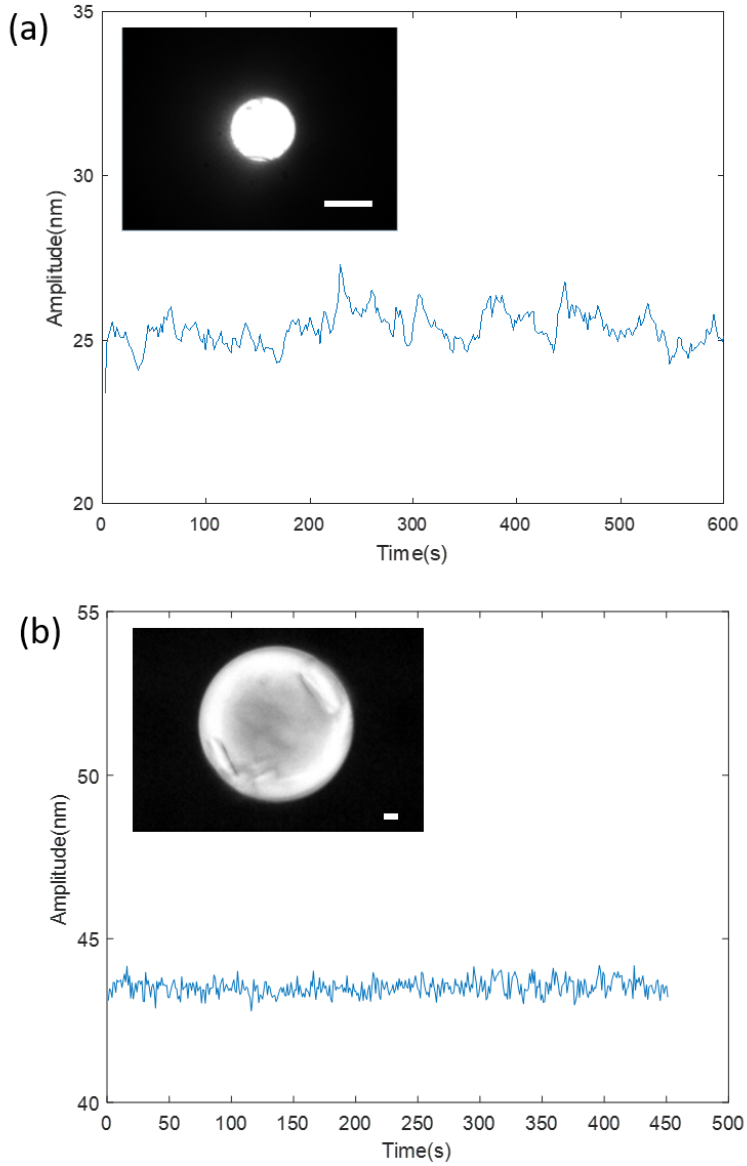

Figure 27. **Demonstration of long term stability.** (a). Small fiber with diameter 13.8 μm and length 9.0 mm, signal at 35 Hz. (b). Large fiber with diameter 112.0 μm and length 10.0 mm, signal at 481 Hz. The scale bar is 10 μm

quadrant-cell 1.9. For the purpose of CSOD, as the fiber movement is usually in the nanometer range, the dynamic range of either detector will suffice.

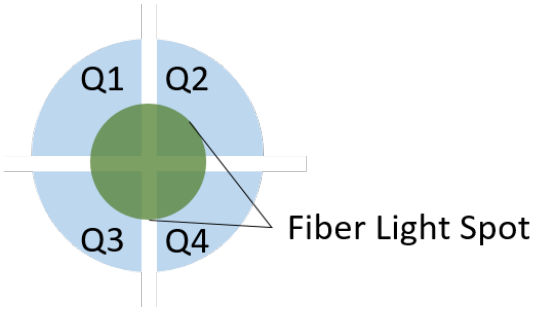

Figure 28. **Quadrant-cell detector.** The quadrant-cell detector with fiber tip shone on the detector. The detector consists of 4 different detection regions.

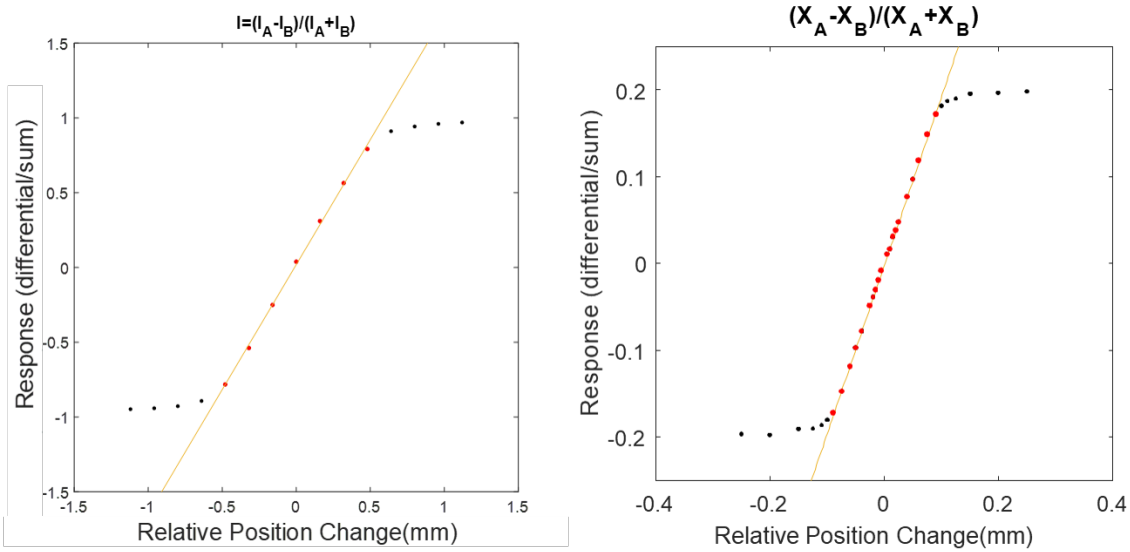

Figure 29. **Calibration of oscillation amplitude.** (a)For camera, relationship between differential intensity $(I_A - I_B)/(I_A + I_B)$ and fiber movement, where the yellow line is a linear fit to the experimental data (dots). (b)For quadrant-cell detector, relationship between differential response $(X_A - X_B)/(X_A + X_B)$ and fiber movement, where the yellow line is a linear fit to the experimental data (dots).

3.3.4 Protein to protein binding

To demonstrate the detection of large molecules, we modify the fiber surface with bovine serum albumin (BSA) and studied the binding kinetics of BSA antibody (anti-BSA) to BSA. The result is shown in Figure 30a. BSA modified fiber tip was initially dipped into a well containing 1X PBS. Its oscillation amplitude was recorded over time as baseline test. Next, 10 μL of additional PBS was injected as a negative control. It was observed that the change of amplitude upon buffer introduction is within the noise level. Later 10 μL of 0.42 $\mu g/mL$ anti-BSA was injected into the well resulting in an anti-BSA concentration of 0.2 nM. The anti-BSA to BSA binding measured using a small fiber is shown in Figure 12 as well as in Figure 30b for reference. It should be noted that in kinetics studies, the change in signal is the actual signal we measure. Here, it is shown that while the change in signal upon binding is similar (~ 6 nm), using a larger fiber greatly lowered the noise, and improved the SNR about 3 times.

3.4 Conclusion and discussion

We have optimized the CSOD detection method for better signal to noise ratio and long term stability by using a larger fiber combined with quadrant-cell detector to move the signal frequency to a higher frequency range, in doing so, we reduced the system noise existent in the lower frequency region and increased the fiber's mechanical stability. Combined with photo-sensitive detector, CSOD has a high potential for automated high throughput applications.

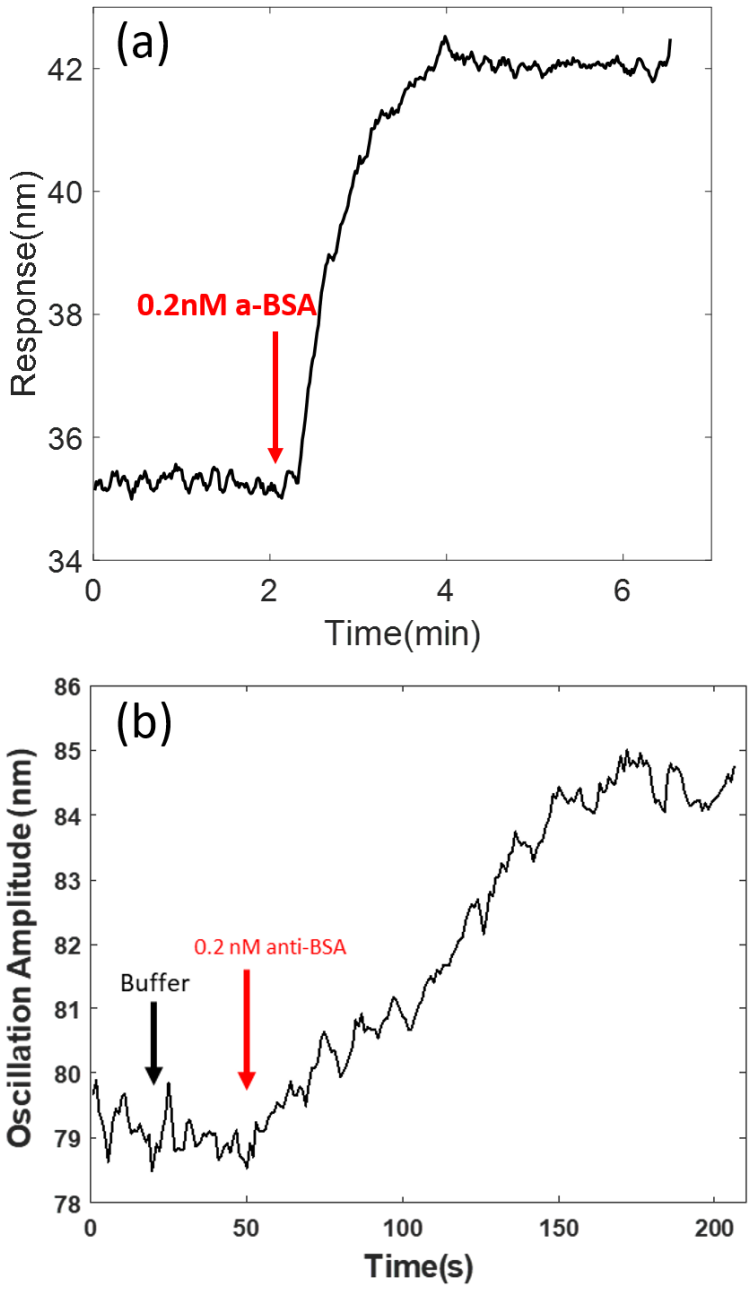

Figure 30. **Anti-BSA binding onto BSA-modified fiber surface.** The black arrow marks the addition of 10 μL 1X PBS buffer, the red arrow marks the addition of μL of 0.42 $\mu g/mL$ anti-BSA (in 1X PBS buffer) leading to a final concentration of 0.2 nM. (a). Fiber diameter: 88 μm, length: 10 mm. (b). Fiber diameter: 17 μm, length: 8 mm.

Chapter 4

CHARGE SENSITIVE OPTICAL DETECTION OF BINDING KINETICS BETWEEN PHAGE DISPLAYED PEPTIDE LIGANDS AND PROTEIN TARGETS

4.1 Introduction

The global peptide therapeutics market is one of the fastest growing segments in the pharmaceutical industry right now. With the market valued at $17.5 billion in 2015 and expected to gain $47 billion in revenues by 2025 [62]. Compared to small molecule drugs, peptides have greater efficacy, selectivity and specificity with lower risks of systemic toxicity and complications. Compared to other biological drug candidates such as antibodies and proteins, peptides are cheaper to manufacture, and they are smaller in molecule size so that it's easier for peptides to penetration into organs or tumors. Peptides also offer higher activity per unit mass with greater stability while compared with other biological drugs [63]. Phage display technology is one of the most widely used *in vitro* display technologies that offers high transformation efficiency with unique peptide clones, besides, higher number of copies can be displayed on phage than in other in vitro display technologies [64].

For phage display technologies, one of the bottlenecks is to triage hundreds of lead molecules for follow up characterization. As of right now, ELISA [65] is the only commonly used method for triaging clones while the displayed peptides are still on phage surface. However, many peptides are displayed in multivalent form and thus ELISA signal only reflects a combination of valency and affinity. In this case, only

qualitative data is provided. To find the best drug candidates out of hundreds of positive peptides screened of out a phage displayed peptide library, binding kinetics data between the peptide and the target protein is needed. In current practice, candidate peptides need to be custom synthesized for binding kinetics measurement, and the process is costly and time consuming.

It is a challenge for using conventional label-free detection methods to measure phage displayed peptide binding kinetics directly, such as Surface Plasmon Resonance (SPR)[12] or Bio-Layer Interferometry (BLI)[13]. SPR has been used to determine the affinity of phage displayed peptides[66]. However, direct measurements of binding kinetics of peptides displayed on the phage proves to be difficult [67], the reasons are the following: 1) the huge molecular mass of phage making the loading of phage onto the sensor surface shifting the baseline out of detection range; 2) the surface density of the displayed peptides is limited by the expression level and the huge mass ratio between the phage and the peptide; 3) if loading the target protein on to the sensor surface, the multi-valency nature of phage expressed peptides making the sensor response curve reflects the collective effect of multi-valency binding kinetics instead of one to one first order binding kinetics. While electrochemical detection methods have been used in phage display technology, they focus on studying the capturing of E. coli or other bacterial cells using phage [68, 69, 70]. It is still challenging to measure the binding kinetics of phage displayed peptides or antibodies without synthesis or purification of the peptides or antibodies.

We have developed a charge sensitive optical detection (CSOD) method that measures molecular interaction kinetics by detecting the binding induced charge changes, which can overcome the mass sensitive limit.[40, 41] In this work, we report

an experiment scheme that combines CSOD with phage display technology to enable rapid quantification of peptide binding kinetics directly on the whole phages.

4.2 Detection Principle

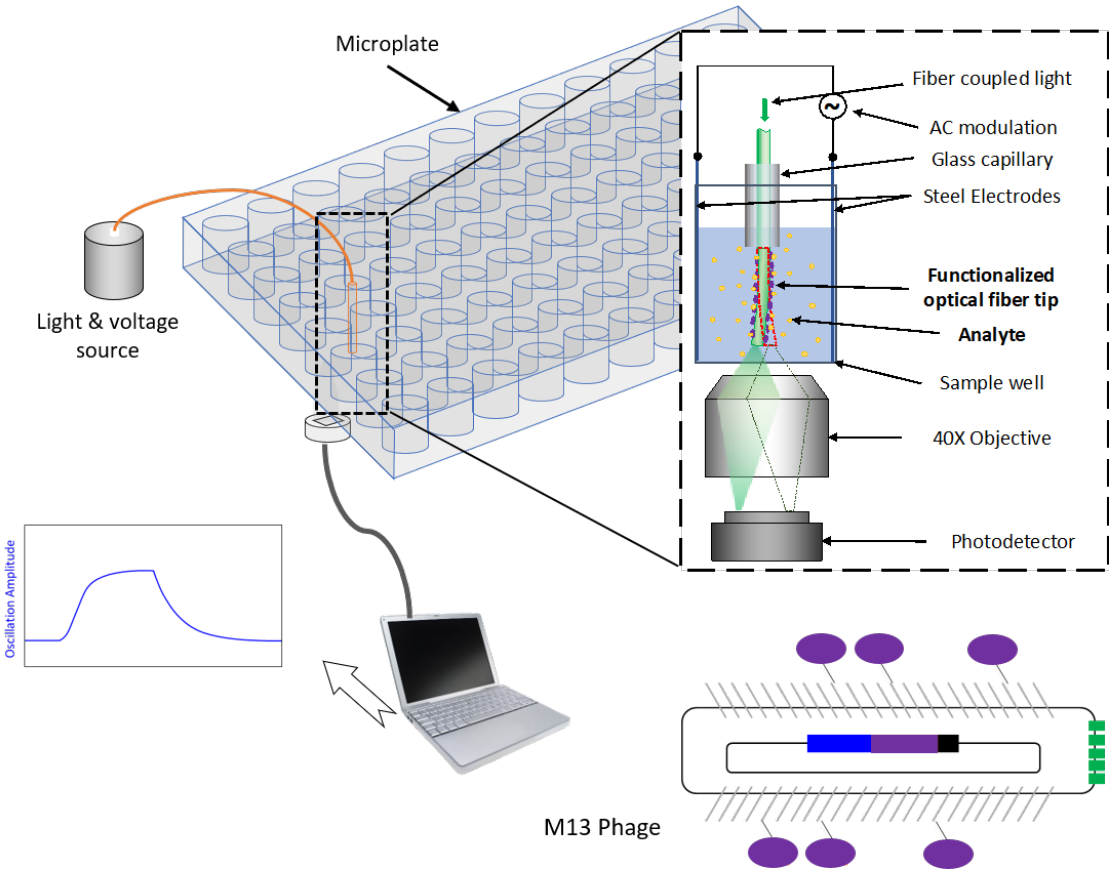

Figure 31. **Schematic of charge-sensitive optical detection of binding kinetics between M13 phage displayed peptides and the protein target.**

A schematic of the CSOD system is shown in Figure 31. Details of the CSOD principle have been described previously[40]. Briefly, a glass optical fiber (diameter $\sim 120\mu m$) with tip (length $\sim 10mm$) functionalized with peptide displayed phage samples is dipped into a microplate well. If the solution well contains molecular ligands

with charge or charged functional groups, binding of the ligands to the phages changes the net charge on the fiber surface. To monitor the charge change, an alternating electric field is applied perpendicular to the optical fiber and drives the fiber to oscillate. The oscillation amplitude is proportional to the surface charge of the optical fiber. To measure the oscillation amplitude, light is coupled into the fiber, the oscillation of the fiber is tracked using a quadrant-cell position sensitive photodetector. The output of the detector is converted to oscillation amplitude by FFT processing of the differential signal as shown in Figure 32.

4.3 Materials and Methods

4.3.1 Materials

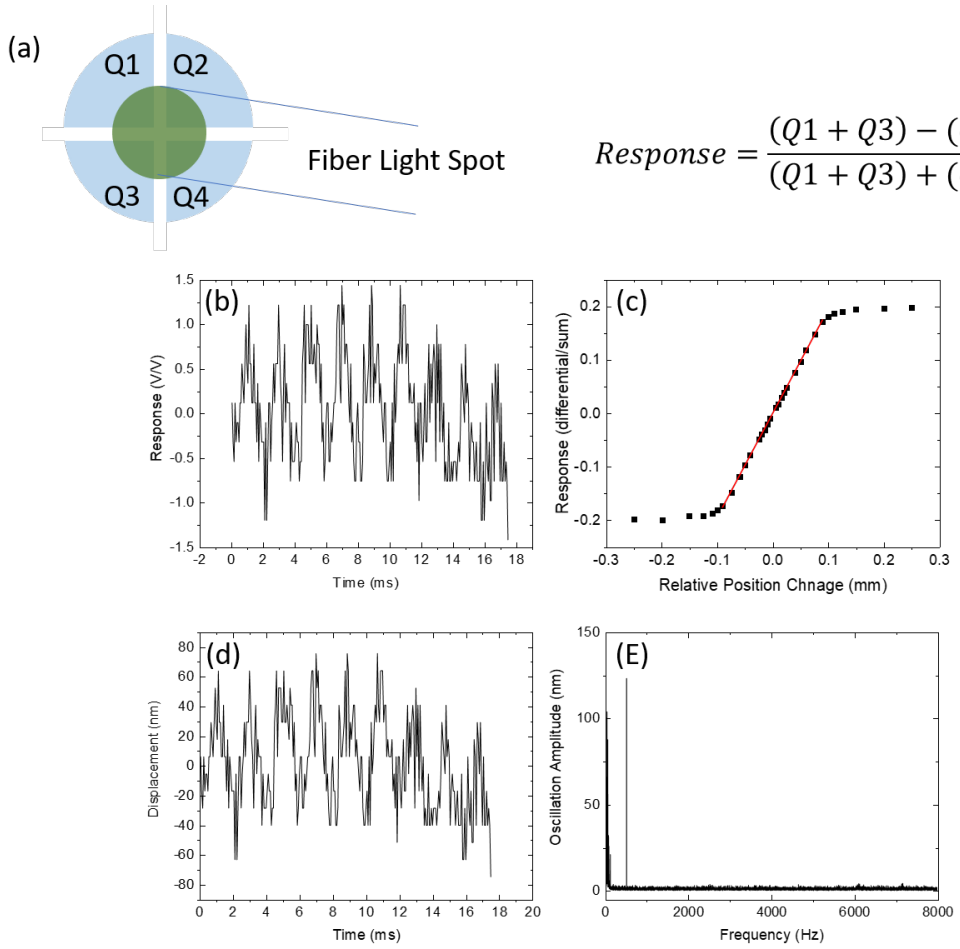

Figure 32. **CSOD data processing workflow.** (a) Schematic shows the light out of the fiber tip projected on the center of the quadrant cell detector, where the sensor response is calculated with the equation shown on the right. Q1 to Q4 are the signals collected by the quadrant cell detector. (b) Representative measured response plotted against time with a sampling rate of 16,000 data points per second. (c) The calibration curve and linear region of the quadrant cell detector. (d) The calibrated fiber oscillation amplitudes over time. (e) The fast Fourier transform (FFT) result of fiber oscillation amplitude in 1 second, where the peak at 511 Hz clearly shows the fiber vibrates at the set frequency.

Table 1. Phage Samples and Descriptions

			Displayed peptide sequence														
sample ID	**sample name**	**note**			**1**	**2**	**3**	**4**	**5**	**6**	**7**	**8**	**9**	**10**	**11**	**12**	**13**	**Signal peptide**
1A	no SG pep2-8AA-2202	negative control			T	V	A	T	S	A	E	E	Y	L	D	W	V	MKIKTGARILALSALTTMMFSASAYA
1B	no SG pep2-8AA-2202	negative control			T	V	A	T	S	A	E	E	Y	L	D	W	V	MKIKTGARILALSALTTMMFSASAYA
2A	no SG pep2-8-2202	positive			T	V	F	T	S	W	E	E	Y	L	D	W	V	MKIKTGARILALSALTTMMFSASAYA
2B	no SG pep2-8-2202	positive			T	V	F	T	S	W	E	E	Y	L	D	W	V	MKIKTGARILALSALTTMMFSASAYA
3A	no SG pep2-8AA-2478	negative control			T	V	A	T	S	A	E	E	Y	L	D	W	V	MKKNIAFLLASMFVFSIATNAYA
3B	no SG pep2-8AA-2478	negative control			T	V	A	T	S	A	E	E	Y	L	D	W	V	MKKNIAFLLASMFVFSIATNAYA
4A	no SG pep2-8-2478	positive			T	V	F	T	S	W	E	E	Y	L	D	W	V	MKKNIAFLLASMFVFSIATNAYA
4B	no SG pep2-8-2478	positive			T	V	F	T	S	W	E	E	Y	L	D	W	V	MKKNIAFLLASMFVFSIATNAYA
5A	SG pep2-8-2478	positive	S	G	T	V	F	T	S	W	E	E	Y	L	D	W	V	MKKNIAFLLASMFVFSIATNAYA
5B	SG pep2-8-2478	positive	S	G	T	V	F	T	S	W	E	E	Y	L	D	W	V	MKKNIAFLLASMFVFSIATNAYA

Multimode optical fibers (125 μm in diameter, FG105UCA, Thorlabs) were purchased from Thorlabs, Inc. Phosphate-buffered saline (PBS) was purchased from Mediatech Inc. M13 phage displayed peptides as well as the drug target PCSK9 protein were provide by Dr. Yingnan Zhang at Genentech. 7 Different phage samples were used as listed in table 1. Deionized (DI) water with a resistivity of 18.2 $M\Omega \cdot cm^{-1}$ filtered through a 0.45 μm filter was used in all experiments. Other chemicals were purchased from Sigma-Aldrich.

4.3.2 Generation of M13 phage displayed peptides

The sequence of peptides listed in Table 1 was fused to the N-terminus of M13 major coat protein (p8) with two different type of secretion signal peptides proceeding at N-terminus (Table 1) using Kunkel mutagenesis[71], with or without SG extension at the N-terminus of the peptide. Peptides with double mutations of F3A:W6A are served as negative controls. The resulting constructs were transformed to E. *Coli*. XL1 blue and single colonies grown in 1 mL 2YT supplemented with 50 $\mu g/mL$ carbenicillin, 10 $\mu g/ml$ Tetracycline and M13 KO7 helper phage at 37°C for 2 h. After addition of Kanamycin (25 mug/mL) and 6 h incubation at 37°C the culture was transferred to 30 mL 2YT supplemented with 50 mug/mL carbenicillin and 25 mug/mL Kanamycin and grown at 37°C overnight. Phage were harvested and purified using standard protocol[65].

4.3.3 Charge-Sensitive Optical Detection Setup

An inverted microscope (Olympus IX-70) with 40X objective, and a quadra-cell position sensitive photodetector (PDQ80A, Thorlabs) was used for CSOD detection. A 96-well microplate with a pair of steel electrodes (1 cm $\times$ 0.6 cm, 0.8 cm distance) inside the wells were mount on a motorized microscope stage (BioPrecision2, Ludl Electronic Products LTD., Hawthorne, NY). Light from a laser (532 nm, 20 mW, Prometheus, Coherent, Santa Clara, CA) was coupled into the fiber via an objective lens (2X, NA 0.06, Olympus). To move the fiber probe between wells, the fiber was clamped to a motorized arm (A-LSQ075B, Zaber) to lift the fiber up and down. A sinusoidal potential was applied with a function generator (33521A, Agilent). A USB data acquisition card (USB-6228, National Instruments) was used to record the output of the photodetector.

4.3.4 Surface Functionalization

The tip (about 1 cm) of an optical fiber thread (about 20 cm) was first soaked in acetone for 1 minute and then rinsed with DI water and dried. The polymer coating layer on the optical fiber was then stripped off with an optical fiber stripper. The bare fiber was etched by soaking it in 47% hydrofluoric acid for 30 seconds for a diameter of $\sim 120\mu m$. The etched fiber was later rinsed with DI water to wash off the hydrofluoric acid and then blew dried with Nitrogen. The tip was cut to about 9mm long. Before functionalization, the optical fiber was cleaned with oxygen plasma for 3 minutes.

The etched fiber was soaked in (3-Glycidyloxypropyl)trimethoxysilane (epoxy) solution (2.5% volume percentage of epoxy in isopropanol) for 1 hour for surface

functionalization. The fiber was then rinsed with PBS buffer. The epoxy modified fiber was soaked in M13 phage sample solution (10^7 phage particles in 1X PBS) for 1 hour.

4.4 Results and Discussion

Protein convertase subtilisin/kexin type 9 (PCSK9) regulates plasma LDL cholesterol levels by degrading liver LDL receptors[72, 73, 74]. PCSK9 acts by binding to the EGF(A) domain of LDL receptor on the cell surface via its catalytic domain[75]. Previously, a peptide, designated as Pep2-8, that inhibit PCSK9 binding to the EGF(A) domain of LDL receptor are effective in lowering LDL cholesterol[76]. The binding kinetics between PCSK9 protein and phage displayed pep2-8 are measured using CSOD technology. Pep2-8 displayed M13 phage samples were functionalized to fiber surface via epoxy coupling. The binding of PCSK9 protein to the phage displaying different formats of pep2-8 are studied in 40 times diluted PBS buffer. For each measurement, a based line was first established by dipping the functionalized fiber tip into a well with buffer, then the fiber was switched to another well contains PCSK9 protein solution to measure the association curve for 150 to 300 s. Finally, the fiber was moved back to the buffer well and dissociation process was recorded. The measured binding kinetics curves are shown in Figure 33. The samples are labelled on the top right corner of each plot. By fitting the kinetic curves at different concentrations globally with first-order kinetics, the association rate constants (k_a), dissociation rate constants (k_d) and equilibrium constants (K_D) for all samples are summarized in Table 2. To confirm the binding specificity, negative controls were

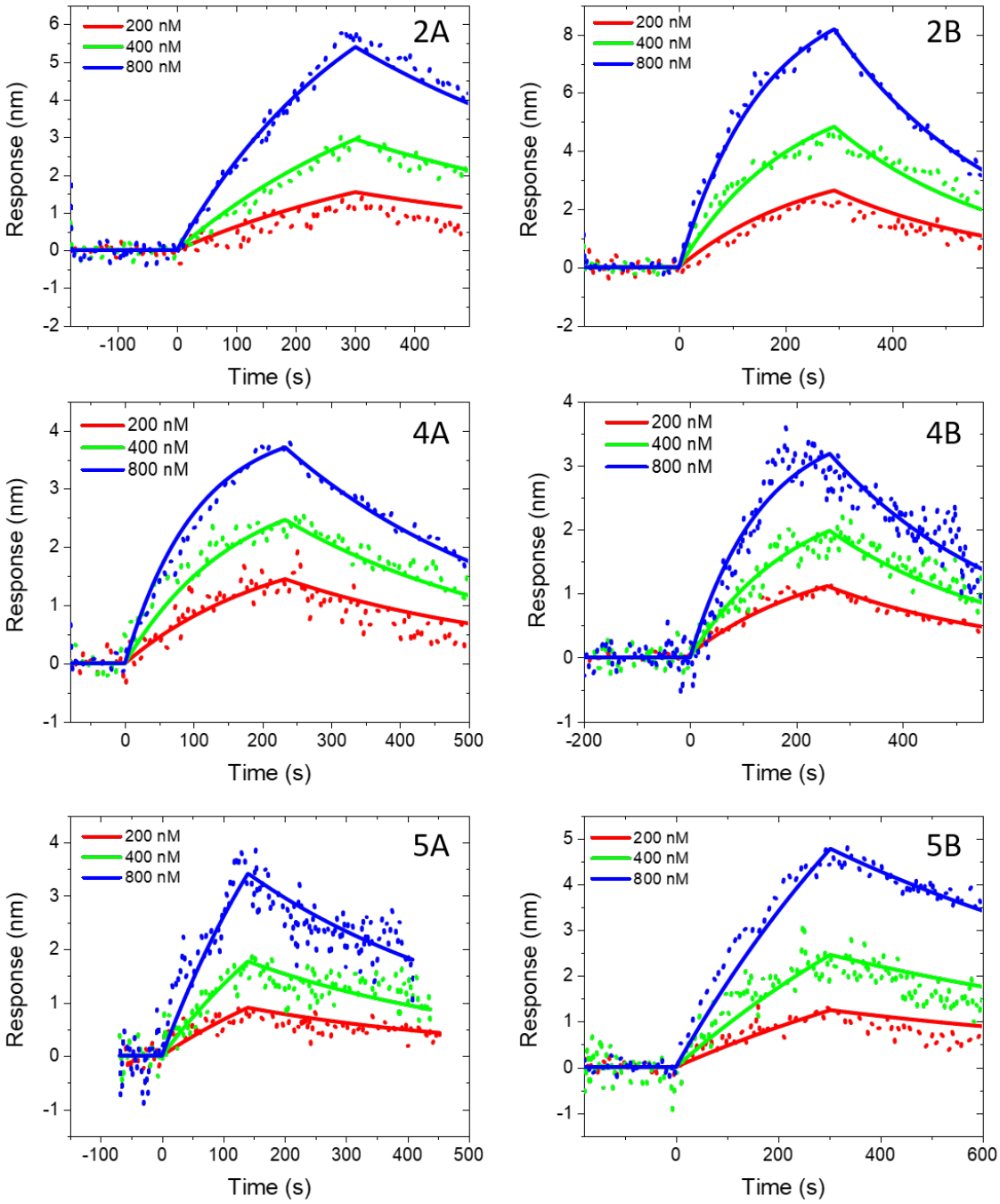

Figure 33. **CSOD measurement results of PCSK9 binding to different peptides displayed on M13 phage surface.** Sample IDs are labeled on the top right corner of each plot.

Figure 33. The fiber probes were switched from a well contains buffer to a well containing PCSK9 at 0 s for measurement of association process, and then switched back to the buffer well at the time indicated by the arrow for measurement of dissociation process.

included. Sample group 1 and 3 are negative controls with displayed peptides that does not bind to PCSK9 protein. As shown in Figure 34, PCSK9 does not bind to any negative sample.

Table 2. Kinetic and Equilibrium Constants of PCSK9 Binding to Phage Surface Displayed Peptides

Sample	Description	$k_a\ (M^{-1} \cdot s^{-1})$	$k_d\ (s^{-1})$	$K_D\ (\mu M)$
2A	no SG pep2-8-2202	1.69×10^3	1.71×10^{-3}	1.01
2B	no SG pep2-8-2202	3.84×10^3	3.21×10^{-3}	0.84
4A	no SG pep2-8-2478	8.63×10^3	2.81×10^{-3}	0.33
4B	no SG pep2-8-2478	5.64×10^3	2.91×10^{-3}	0.52
5A	SG pep2-8-2478	1.34×10^3	2.62×10^{-3}	1.96
5B	SG pep2-8-2478	0.5×10^3	1.12×10^{-3}	2.20

From the kinetics results shown in Table 2, for each sample group, while the peptide displayed on phage surface is the same, there is some sample variation, which is consistent with the slight difference in kinetic constants. It is shown that for different peptides, measured equilibrium constants are different. This is expected as different peptides have different structures and thus have different binding kinetics to PCSK9 protein. Based on the measured results suitable peptides with higher affinity as well as appropriate k_a and k_d can be selected. Previously, the affinity between Pep2-8 and PCSK9 were measured by biolayer interferometry and the determined K_D was $0.66 \pm 0.11 \mu M$. This affinity was consistent with the IC50 of $0.81 \pm 0.08 \mu M$ measured by a competition ELISA where the binding of biotinylated PCSK9 to plate-

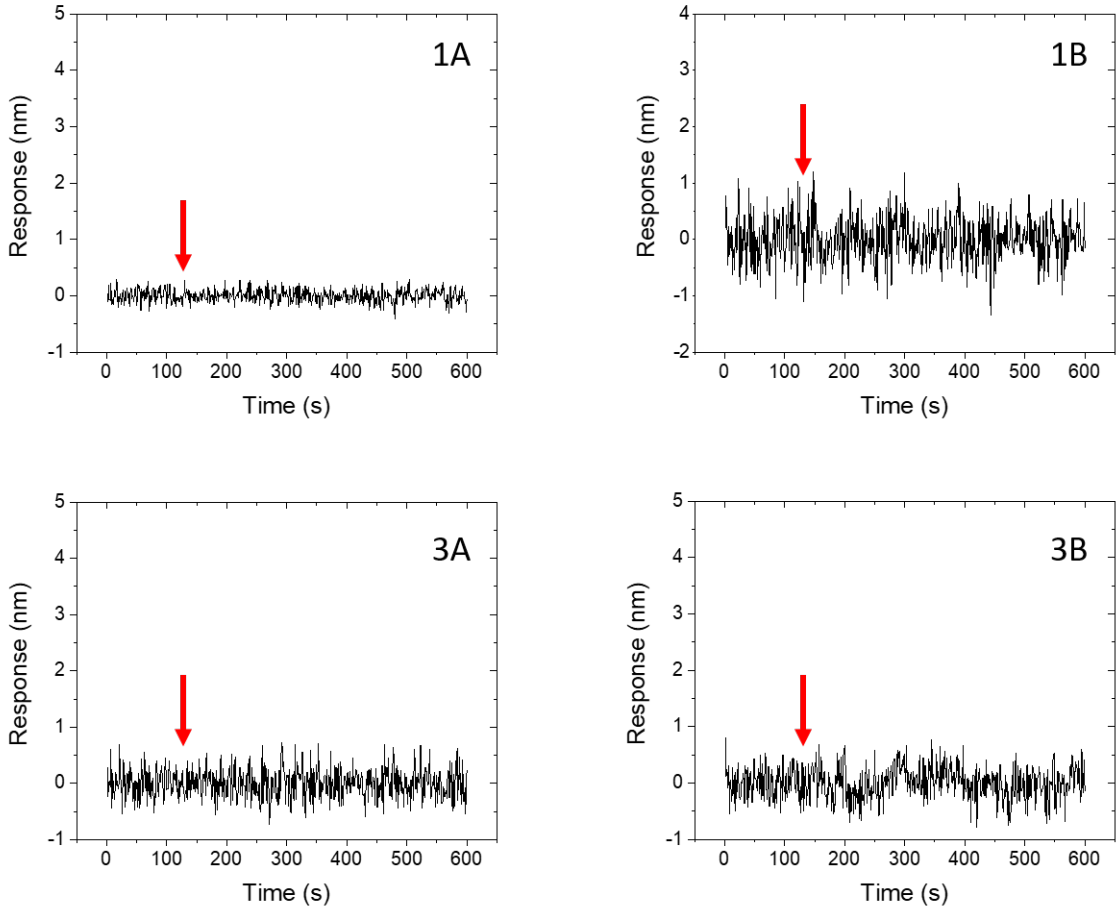

Figure 34. **CSOD measurements of PCSK9 binding to negative samples.** Sample IDs are labeled on the top right corner of each plot. Read arrows indicate a change from buffer to 1000 μM PCSK9 concentration.

coated LDLR being competed off by synthesized Pep2-819[76]. Overall, the affinities measured by CSOD were roughly consistent with previously measured K_D and IC50 for pep2-8, with 2 folds variation between phage clones with two different secretion signal peptides, as well as 2 folds affinity drop with SG extension at N-terminus.

4.5 Conclusion

We used demonstrated CSOD system technology for direct testing quantification of phage displayed peptides binding kinetics to a specific drug target. We have shown that CSOD can be used to distinguish different binding kinetics of different peptides displayed by phage display technology. The kinetic data were validated by the SPR measured purified peptide data. This method can be incorporated into a diversity display pipeline and increase the productivity of library screening.

Chapter 5

CRITICAL ANGLE REFLECTION IMAGING FOR QUANTIFICATION OF MOLECULAR INTERACTIONS ON GLASS SURFACE

5.1 Introduction

Molecular interactions are ubiquitous in biological systems and important to the understanding of molecular biology and drug discovery. Surface plasmon resonance (SPR) is the most widely used label-free techniques in pharmaceuticals and research labs for measuring molecular binding kinetics.[77, 78, 79] Owing to the sharp response to the refractive index change on the surface, the high sensitivity of SPR enables the detection of biomolecules,[79] small molecules,[80] viruses,[81] and cells.[82, 83] To generate SPR on the surface, the sensor chip (glass slide) must be coated with a metal film (typically gold), which is laborious and increases the operation cost. The gold film is not required for glass-based biosensors, such as interferometers [84, 85, 86] microring and microsphere resonators [87, 88, 89]. However, these sensors are made through microfabrication and still labor consuming. Reflectometry based on measuring phase shift can directly quantify binding kinetics on a cover glass,[90, 91] but due to the instrumentation complexity and moderate sensitivity, it is not as competitive as SPR. It is desirable to develop new simple and sensitive techniques for molecular interaction measurements.

The sensitivity of most label-free optical biosensors originates from the response of the probe light to the refractive index change on the sensor surface.[92] For example, in SPR, the reflectivity of the light is significantly reduced at a specific incident angle

when the light energy resonates with the surface plasmons in the gold film, and the resonance angle is highly sensitive to the refractive index changes near the surface. By measuring the resonance angle shift, we can measure molecular interactions on the surface that changes the local refractive index. Inspired by this principle, we thought that the molecular interactions induced refractive index changes can also be detected on bare glass when the incident angle is close to the critical angle. Because the critical angle is also refractive index dependent, therefore, the critical angle shift should be a measure of the refractive index change near the glass surface. Indeed, previous studies have shown that 10-6 refractive index change can be resolved on the glass-water interface by measuring the reflectivity near the critical angle.[93] However, this method has never been developed into a biosensing technique to the best of our knowledge. Although total internal reflection-based methods have been used for measuring binding kinetics [84, 85, 88, 91], imaging nanoparticles [94] and obtaining infrared spectra of molecules and cells[95, 96], the incident light in these methods is set above the critical angle, where the reflectivity is saturated and the refractive index sensitivity is totally lost.

Taking advantage of the refractive index-dependent nature of the critical angle, we developed a technique called critical angle reflection (CAR) imaging to measure the molecular interactions on a glass surface. CAR presents several unique features compared to SPR. Firstly, the sensitivity of CAR increases with incident angle and can be higher than SPR as the angle approaches the critical angle, allowing CAR to measure small molecules that are challenging for SPR. Also, CAR uses bare cover glass, which is simpler, more robust and compatible with fluorescence measurement than gold coated cover glass used by SPR, allowing simultaneous measurement of binding kinetics and fluorescence or total internal reflection fluorescence (TIRF). Due to the

similarity in detection principle, CAR measurements can be readily implemented in existing SPR setups without the need of additional hardware. We measured the binding of proteins, nucleic acids, and small molecules, and performed cell-based measurements to demonstrate the advantages of CAR on a commercial SPR imaging setup and a home built objective-based SPR microscope. We anticipate CAR will broaden the capability of SPR with increased sensitivity, concurrent fluorescence imaging, glass surface chemistry and lower sensor fabrication cost.

5.2 Methods

5.2.1 Experimental Setup

The SPR and CAR measurements for principle demonstration (Figure 35) and protein, miRNA, and small molecule detections (Figures 39 and 43) were conducted using a commercial prism-based SPR imaging system (SPRm 200, Biosensing Instrument Inc., Tempe, Arizona) with a 690 nM, 1 mW laser, and a custom installed USB3 CMOS camera (MQ003MG-CM, XIMEA, Germany). The incident angle is controlled via a motor attached to the light source with an accuracy of 5.5 millidegrees and scanning range from 40 to 76 degrees. The system has 20× magnification. Samples were delivered to the system via an autosampler (BI autosampler, Biosensing Instrument Inc.). The SPR instrument can be directly used for CAR measurement without any modification. The only difference is using a glass sensor chip instead of the gold coated glass chip and lowering the incident angle from $\sim$ 70 degrees (SPR angle) to $\sim$ 61 degrees (critical angle).

All the cell-related experiments including CAR, SPR, transmitted and fluorescence

measurements (Figures 48, 50 and 52) were performed on an objective-based SPR microscope setup, which consisted of an inverted microscope (Olympus IX-81) and a 60× (NA 1.49) oil-immersion objective. The light source for CAR and SPR imaging was a superluminescent light emitting diode (SLED) (SLD-260-HP-TOW-PD-670, Superlum, Ireland) with 670 nm wavelength and 1 mW power set by a SLED current driver (PILOT4-AC, Superlum). The SLED was mounted on a translation stage (PT3, Thorlabs) with a motorized actuator (Z825B, Thorlabs) for adjusting incident angle. The angle accuracy was determined to be ∼10 millidegrees. The light source for transmitted and fluorescence imaging were the stocking halogen and mercury lamp of the microscope, respectively. The excitation and emission wavelength used for imaging Alexa Fluor 488 labelled WGA were 488 nm and 518 nm, respectively, and the power density on the sample was $\sim 0.1\ mW/cm^2$. A CMOS camera (ORCA-Flash 4.0, Hamamatsu) was used to record the images. A gravity-based drug perfusion system (SF-77B, Warner Instruments, Connecticut) was used for delivering analytes to the cells.

5.2.2 Materials

Cover glass (No.1) for CAR measurements were purchased from VWR. The cover glass was coated with 1.5 nm Cr followed by 43 nm gold using an e-beam evaporator for SPR measurements. Dextran coated SPR sensor chips were purchased from Biosensing Instrument Inc. (3-glycidyloxypropyl)trimethoxylsilane, N-hydroxysulfosuccinimide sodium salt (NHS), N-(3-dimethylaminopropyl)-N′-ethylcarbodiimide hydrochloride (EDC), O-(2-Carboxyethyl)-O′-(2-mercaptoethyl)heptaethylene glycol (SH-PEG8-COOH), bovine serum albumin (BSA), carbonic anhydrase lysozyme

II from bovine erythrocytes (CAII), furosemide, sulpiride, methylsulfonamide, and acetylcholine perchlorate were purchased from Sigma-Aldrich. Mouse anti-cattle bovine serum albumin monoclonal antibody (anti-BSA) was purchased from MyBioSource. MicroRNA-21 (5′-UAG CUU AUC AGA CUG AUG UUG A-3′) and biotinylated complementary DNA with A5 spacer (5′ biotin-AAAAA TCA ACA TCA GTC TGA TAA GCT A-3′) were purchased from Integrated DNA Technologies. Streptavidin, methyl-PEG_4-thiol (MT(PEG)4), and wheat germ agglutinin (WGA) with Alexa Fluor 488 tag were purchased from Thermo Fisher Scientific. Phosphate buffered saline (PBS) was purchased from Corning. Deionized water with resistivity of 18.2 $M\Omega \cdot cm$ was used in all experiments.

5.2.3 Surface Functionalization

The gold surface was rinsed with ethanol and water each for three times and then annealed with hydrogen flame. The cleaned chips were incubated in 0.2 mM SH-PEG8-COOH and 0.2 mM MT(PEG)4 in PBS overnight. Then the -COOH groups were activated by incubating in a mixture of 50 mM NHS and 200 mM EDC for 20 minutes. 5 μM BSA, 2.2 μM CAII, or 6 μM streptavidin was applied to the surface immediately and incubated for one hour. The remaining activated sites were quenched with 20 mM ethanolamine for 10 minutes. Finally, the CAII and streptavidin functionalized surfaces were incubated with 1 mg/mL BSA solution to block non-specific binding sites. To immobilize cDNA on the surface, 33 μM biotinylated cDNA was applied to the streptavidin functionalized surface and incubated for one hour.

The glass chip was rinsed with ethanol and water for three times. Then the chips were dried with N_2, treated with oxygen plasma, and incubated in 1% (3-

glycidyloxypropyl) trimethoxylsilane in isopropanol overnight. After rinsed with isopropanol and DI water, the chips were immediately incubated with 5 μM BSA, 2.2 μM CAII, or 6 μM streptavidin for one hour. Next, 20 mM ethanolamine was used to quench the unreacted sites for 5 minutes, and 1 mg/mL BSA was applied to the CAII and streptavidin coated chips for 10 minutes to block non-specific sites. cDNA was immobilized on the streptavidin coated surface by incubation in 33 μM biotinylated cDNA solution for one hour.

5.2.4 Cell Culture

HeLa, SH-EP1, and SH-EP1$_\alpha 4\beta 2$ cells were obtained from the American Type Culture Collection. The cells were cultured in Dulbecco's modified eagle medium (Lonza) with 10% fetal bovine serum (Invitrogen) and 1% penicillin and streptomycin in a humidified incubator at 37 °C with 5% CO_2. The cells were harvested at 75% confluence, transferred to glass or gold coated glass chips, and cultured overnight before experiments. The glass and gold surfaces were pretreated with 0.3 mg/mL collagen type IV (Sigma-Aldrich) to improve cell attachment to the surface. For experiments using fixed cells, the cells were fixed with 4% paraformaldehyde solution (Santa Cruz Biotechnology) for 20 minutes, washed with PBS and immediately placed on instrument for measurement.

5.2.5 Simulation and Data Processing

WinSpall 3.01 (http://res-tec.de/downloads.html, Resonant Technologies GmbH, Germany) was used to calculate the reflectivity as a function of incident angle for CAR and SPR.

For all SPR and CAR detections using the prism-based setup, the images were initially recorded at 100 frames per second and then averaged over every one second by software (ImageAnalysis, Biosensing Instrument Inc.). For SPR and CAR measurements on the microscope-based setup, the images were recorded at 10 frames per second and averaged over every one second. The averaged CAR and SPR images were processed with Fiji34 to obtain reflectivity change. Then reflectivity was converted to refractive index unit (RIU) using the ethanol calibration curves (Figure 35c and Figure 37b). The unit RIU was finally converted to resonance unit (RU) by 1 RU = 106 RIU, which is often used in SPR sensorgrams for result presentation. If needed, RU can be used to estimate mass density or surface coverage of the molecule being measured (1 RU $\sim$ 1 pg/mm^2).(the biacore ref.) After unit conversion, the response curve fitting and binding kinetics constant calculation were carried out with ImageAnalysis and Scrubber (BioLogic Software).

5.3 Results

5.3.1 Detection Principle

The CAR imaging setup is the same as a Kretschmann SPR imaging setup, [97] where a detection camera is set to focused at the sample layer on the glass surface to

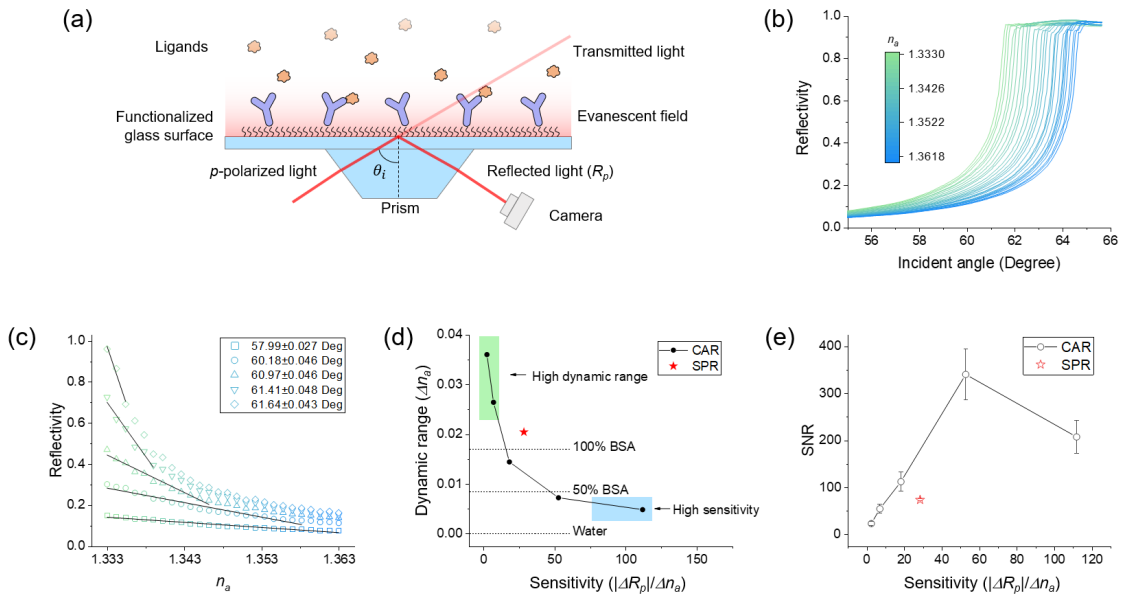

Figure 35. **Detection principle of CAR.** (a) Experimental setup and surface chemistry. A protein functionalized cover glass is placed on a prism-based SPR imaging setup with index matching oil. The incident angle θ_i of a p-polarized light is set at slightly below the critical angle. Upon ligands binding to the proteins, the intensity of the reflected light changes and is detected by a camera. (b) Measured reflectivity change as a function of incident angle. The refractive index (n_a) on the surface is adjusted by serially adding ethanol to water to make n_a ranges from 1.3330 (pure water) to 1.3630 (50% ethanol in water). (c) Measured reflectivity as a function of n_a at five representative incident angles with data obtained from (b). The solid lines show the linear regions (defined by $R^2 > 0.97$, where R^2 is the coefficient of determination) of the curves. (d) Tunable sensitivity and dynamic range of CAR. The black dots show the sensitivity and dynamic range determined at the five representative angles in (c), where the sensitivity and dynamic range are the slope and the range of the linear regions, respectively. The red star marks the sensitivity and dynamic range of SPR, which is not adjustable. To facilitate comparison, the refractive index change induced by the binding of a full layer of BSA (100% BSA), half layer of BSA (50% BSA), and pure water (Water) are marked by the dashed lines. (e) Measured signal-to-noise ratio of SPR and CAR at the five representative angles. Noise is defined as 1 minute of root mean square of baseline signal.

collect the reflected light, where the incident light is collimated (Figure 35a). The contrast of the image comes from change of reflectivity by the refractive index changes on or near the sensing surface. There are two adjustments in experimental conditions from SPR: (1) The sensor chip is a bare cover glass instead of a gold coated cover glass; and (2) the incident light is set at slightly below the critical angle, whereas in SPR imaging the incident angle is normally set to slightly below the SPR resonance angle, which is a couple degrees higher than the critical angle. To perform measurements, the glass surface is functionalized with receptor molecules to capture the ligands in the solution, and upon ligand binding, the refractive index near the surface changes, leading to a change in the reflected light intensity. By measuring the intensity change with a camera, the receptor-ligand interaction can be monitored in real-time.

The detection principle of CAR with p- or s-polarized light can be described by Fresnel equation with similar format. We use the equations for p-polarized light below as an example. When a p-polarized light is introduced into a glass prism at an incident angle θ_i and reflected at the interface between the glass and the aqueous solution, as shown in Figure 35a, the reflectivity (power reflection coefficient) R_p is given by [98]:

$$R_p = \left| \frac{n_g \sqrt{1 - \left(\frac{n_g}{n_a} \sin\theta_i\right)^2} - n_a \cos\theta_i}{n_g \sqrt{1 - \left(\frac{n_g}{n_a} \sin\theta_i\right)^2} + n_a \cos\theta_i} \right| \tag{5.1}$$

where n_g is the refractive index of glass, and n_a is refractive index of aqueous solution. R_p increases with the incident angle, and reaches maximum value of 1 at critical angle θ_c, where

$$\theta_c = \sin^{-1}\left(\frac{n_a}{n_g}\right) \tag{5.2}$$

Scanning θ_i from below to above θ_c shows that R_p increases faster as θ_i approaches θ_c and finally reaches total internal reflection at θ_c (Figure 35b). The sensitivity of

CAR arises from the rapid reflectivity change (ΔR_p) near θ_c caused by the refractive index change in the aqueous solution near glass surface (Δn_a) due to molecular binding. Since most of molecules have higher refractive index than water, molecular binding event at the glass surface usually increases the effective refractive index of aqueous solution above glass surface ($\Delta n_a > 0$) and results in right-shift of the curve, which will lower the reflectivity ($\Delta R_p < 0$) if θ_i is fixed at an angle slightly lower than θ_c. For a given Δn_a, $|\Delta R_p|$ becomes larger as the θ_i gets closer to θ_c. The experimental results were verified by simulation (Figure 36). This unique feature allows us to tune the sensitivity ($|\Delta R_p|/\Delta n_a$) by changing θ_i (Figure 35c). In contrary, the sensitivity of SPR is fixed for θ_i in the normal measurement range (Figure 37).

To evaluate the performance of CAR as a sensing method, we compared its sensitivity and dynamic range with those of SPR using the same instrument. We used p-polarized light as the incident light in both CAR and SPR for the comparison because SPR can only be generated by p-polarized light. The sensitivity and dynamic range are defined as the absolute value of slope and linear range of R_p vs. n_a plot at given angles (Figure 35c and Figure 37), respectively. The units for dynamic range and sensitivity are RIU (refractive index unit) and RIU^{-1}. The results for CAR and SPR are plotted in Figure 35d. At low angles, CAR presents low sensitivity, but the dynamic range can be at least 2 times greater than SPR. At high angles, CAR is 5 times more sensitive than SPR, but the dynamic range is 4 times lower. Theoretically, the sensitivity and dynamic range of CAR approaches infinity and zero respectively as the incident angle reaching the critical angle, however, the accuracy of incident angle is limited by diffraction of the incident light, and thus the exact

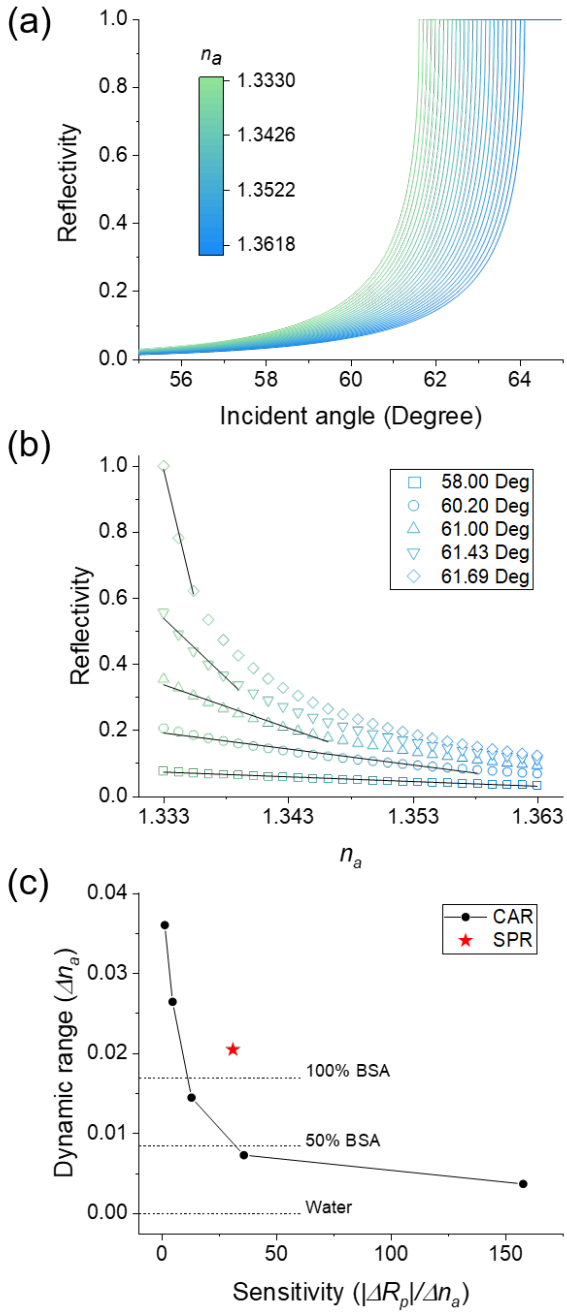

Figure 36. **Simulation results of CAR.** (a) Relationship between reflectivity and incident angle at different aqueous solution refractive indices (n_a).

Figure 36. (b) Reflectivity vs. n_a at five representative incident angles. The black lines are fittings of the linear regions ($R^2 > 0.97$). (c) Sensitivity and dynamic range of CAR at the five representative angles (black dots). Sensitivity and dynamic range are determined by the slope and the linear range of the black lines in (b). The red star marks the theoretical sensitivity and dynamic range of SPR. The simulation is shown in Figure 37.

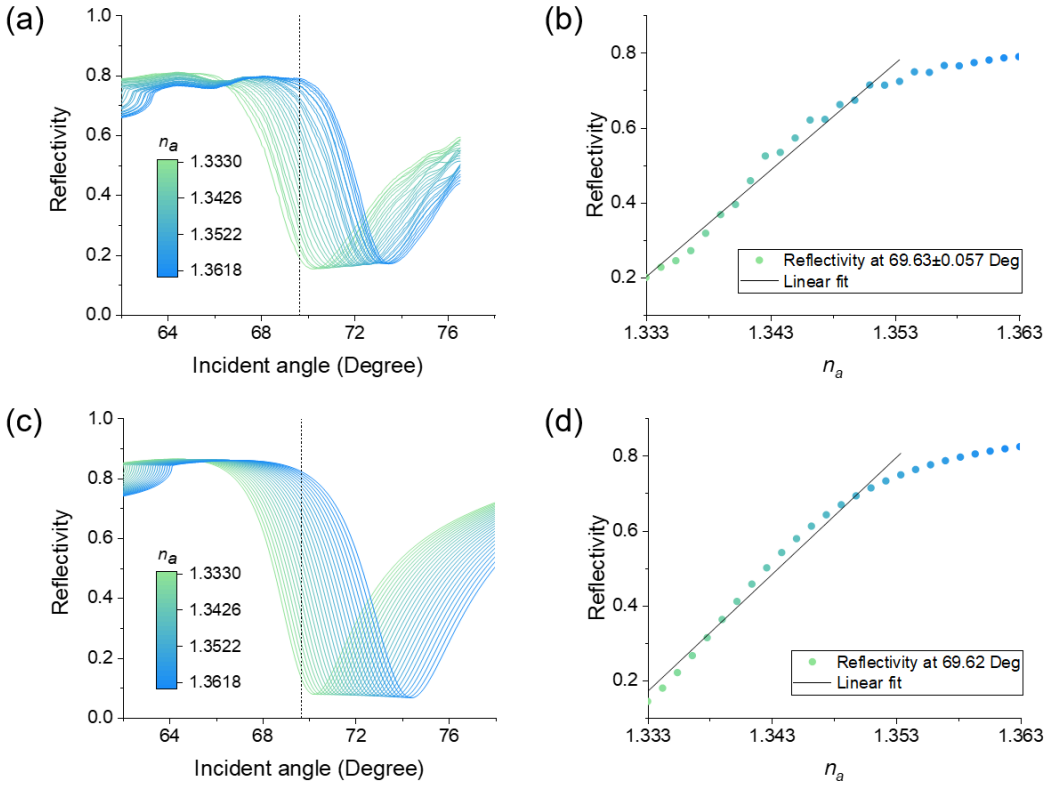

Figure 37. **Experimental and simulated SPR responses.** (a) Measured reflectivity as a function of incident angle at different aqueous solution refractive indices (n_a). (b) Reflectivity vs. n_a at 69.63 degrees (marked by the vertical dash line in a). The black line is fitting of the linear region ($R^2 > 0.97$). The sensitivity and the dynamic range of SPR are determined by the slope and the linear range of the black line. (c) Simulated SPR reflectivity at different incident angles and n_a. (d) Reflectivity vs. n_a plot at 69.62 degrees (marked by the vertical dash line in c) obtained from the simulated data in c. The black line is fitting of the linear region ($R^2 > 0.97$), from which the theoretical sensitivity and dynamic range are calculated.

critical angle is hardly accessible. [93, 99] The reduced dynamic range at high angles is still sufficient to measure the binding of medium sized proteins, for example, bovine serum albumin (BSA, 66 kDa) at up to 25% surface coverage. In between the low and the high angles, CAR has similar sensitivity and dynamic range as SPR. We also measured the signal-to-noise ratio (SNR) of CAR (Figure 35e). The incident light was set at five representative angles, and 1% ethanol was added to water to generate a refractive index increase (Figure 38). The ethanol induced reflectivity change and baseline fluctuation were defined as the signal and noise, respectively. The maximum SNR of CAR is ~ 5 times higher than SPR, suggesting CAR is more sensitive to smaller molecules than SPR. Similar sensitivity and dynamic range can be achieved by CAR with s-polarization (see Discussion).

To demonstrate the capability of CAR in measuring binding kinetics, we first measured the binding of bovine serum albumin antibody (anti-BSA) to bovine serum albumin (BSA), which is often chosen as a model binding pair in SPR (Figure 39a). BSA was immobilized on the surface of a cover glass (see Methods). Because anti-BSA is a large biomolecule (150 kDa), we tuned CAR sensitivity to medium sensitivity (25 RIU^{-1}, close to SPR) by setting the incident angle at 61.1 degrees. In the experiment, different concentrations of anti-BSA were serially injected over the BSA coated surface (Figure 39b). Binding of anti-BSA to BSA increased the refractive index on the sensing surface. After anti-BSA binding in each cycle, buffer was introduced to the surface to induce the dissociation of anti-BSA from BSA. For ease of comparison with SPR, we converted the refractive index change in CAR (unit: RIU) to resonance unit (RU), a unit typically used in SPR, by 1 RU = 10^6 RIU (see Methods).

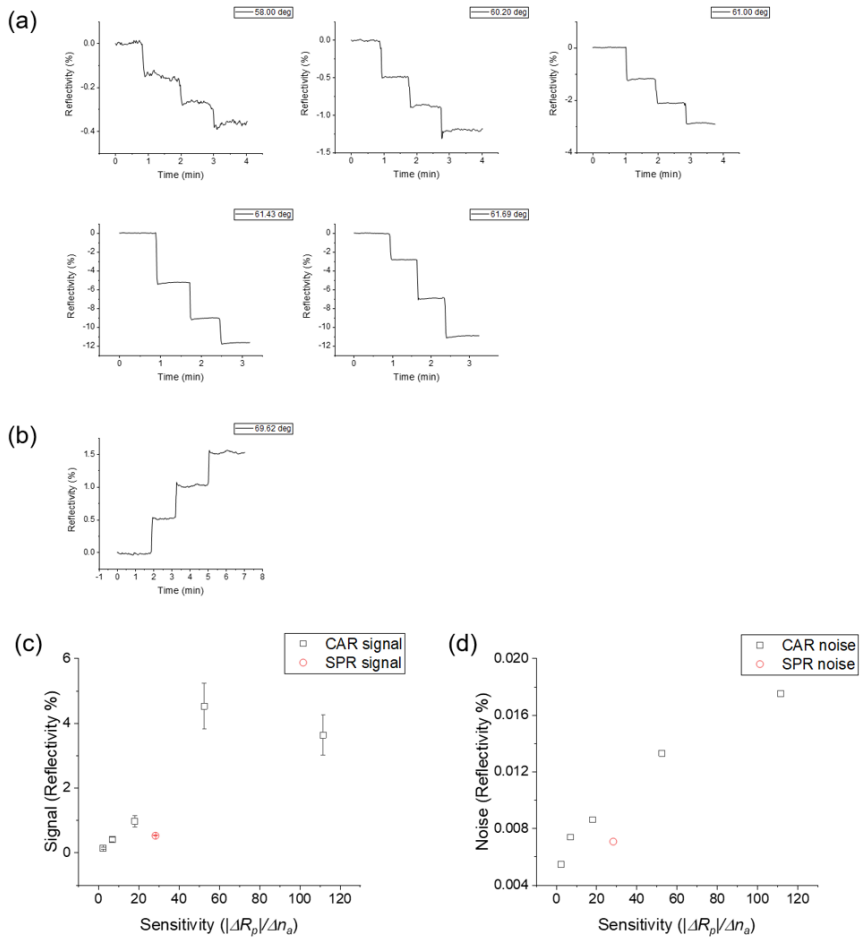

Figure 38. **Measuring the SNR for CAR and SPR.** (a) Determining the SNR for CAR at five representative angles. 1% ethanol (final concentration) is added to water for three times, which leads to three reflectivity drops. The average value of the three responses is defined as the signal, and the standard deviation of the baseline (over 1 minute) is defined as the noise. (b) Determining the SNR for SPR. 1% ethanol (final concentration) is added to water for three times. The signal and noise are calculated the same way as in (a). (c) Signal of CAR and SPR. The error bar represents the standard deviation of three measurements. (d) Noise of CAR and SPR.

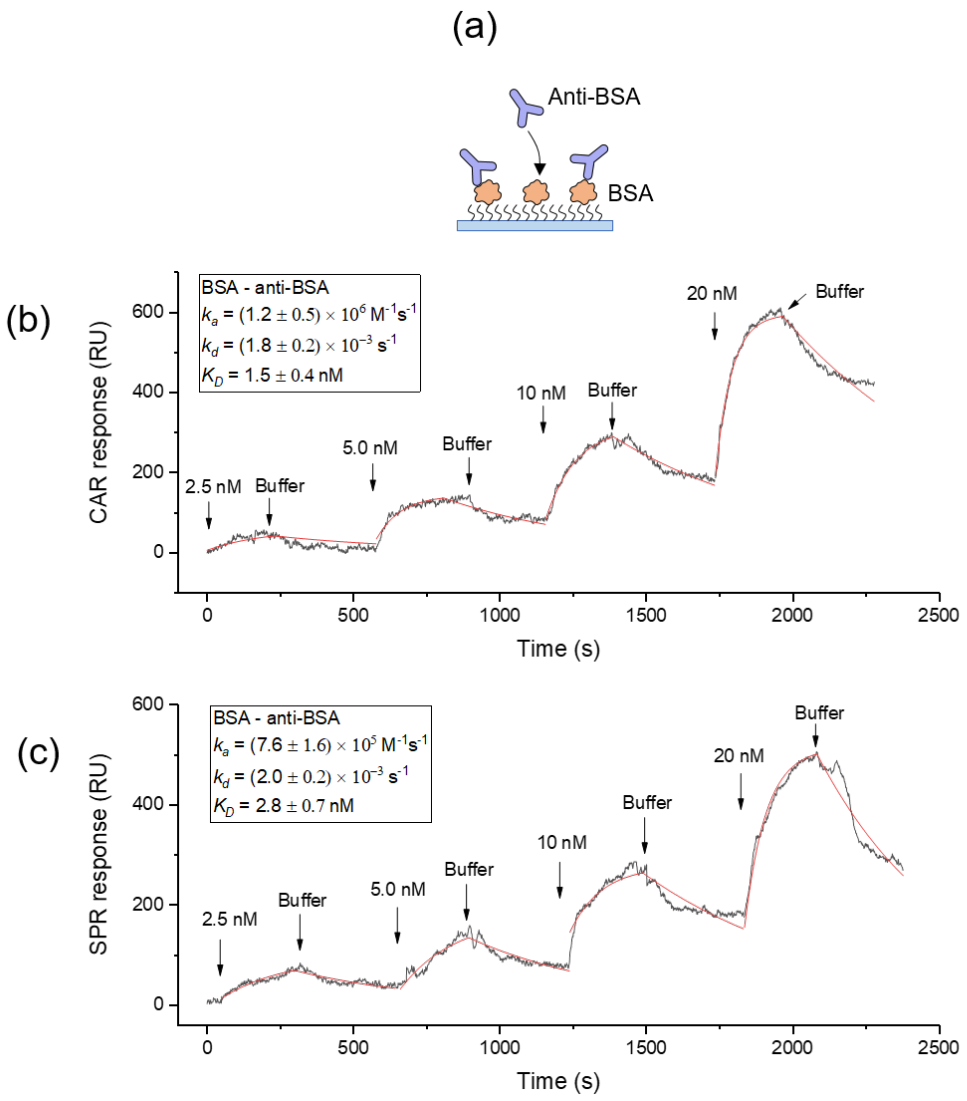

Figure 39. **Anti-BSA binding to BSA detection.** (a) Anti-BSA binding to BSA. BSA is immobilized on a glass or gold surface for CAR or SPR measurements. (b) Measuring anti-BSA – BSA binding kinetics with CAR. The incident angle was set at 61.1 degrees with a sensitivity of 25 RIU^{-1}. Anti-BSA with different concentrations and buffer were sequentially flowed over the BSA coated surface. The CAR response (black curve) was fitted to the first order of kinetics (red curve). Note that 1 RU = 106 RIU = 1 pg/mm^2 of mass density. (c) Measuring anti-BSA to BSA binding kinetics with SPR. The experimental conditions were the same as the CAR measurement.

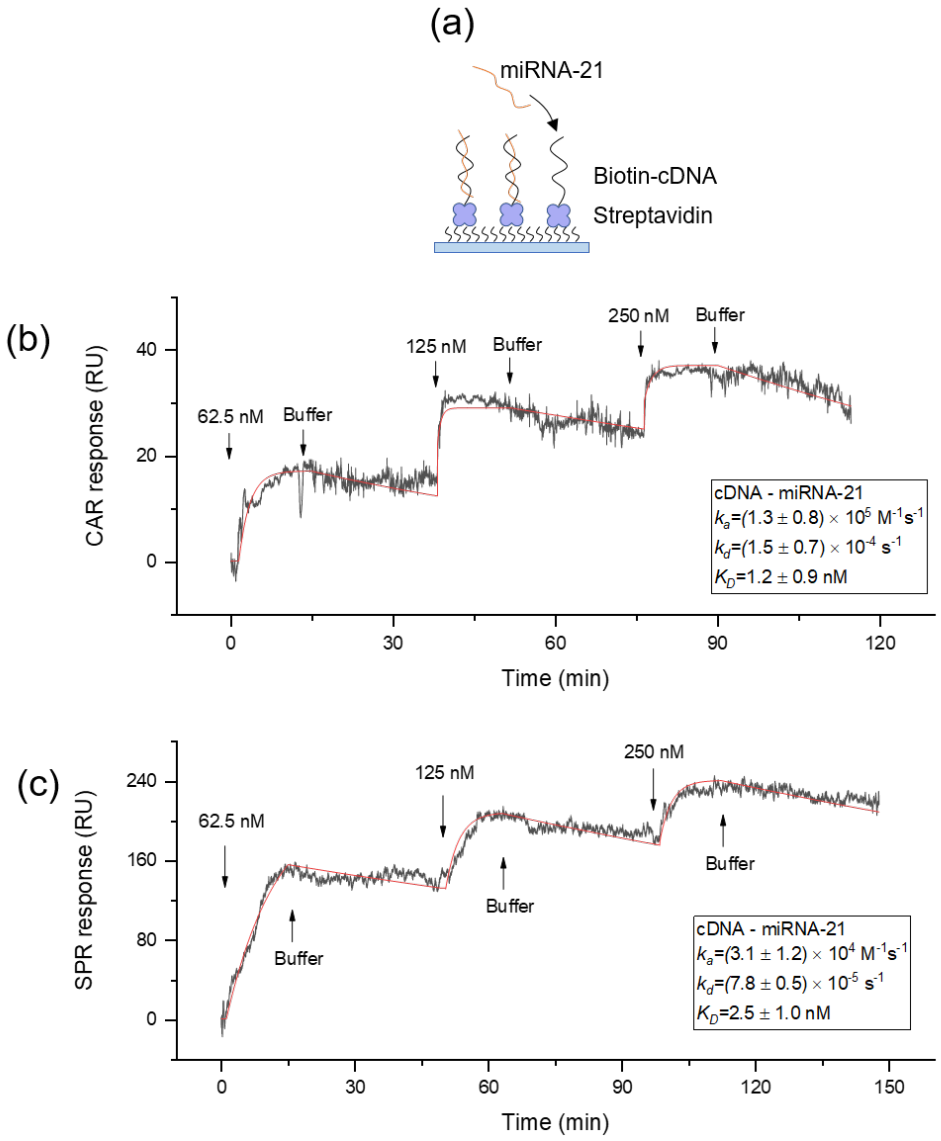

Figure 40. **mi-RNA binding to cNDA.** (a) miRNA-21 binding to cDNA. The biotinylated cDNA was immobilized on a streptavidin coated glass or gold surface via streptavidin-biotin conjugation. The miRNA-21 to cDNA binding was measured with CAR (b) and SPR (c), and the curves (black) were fitted to the first order of kinetics (red curves). The CAR incident angle was set at 61.4 degrees with a sensitivity of 50 RIU^{-1}.

By fitting the CAR response curves to first order binding kinetics, the association rate constant k_a, dissociation rate constant k_d, and equilibrium constant K_D were determined to be $(1.2\pm0.5)\times10^6\ M^{-1}\cot s^{-1}$, $(1.8\pm0.2)\times10^{-3}\ s^{-1}$, and $1.5\pm0.4\ nM$, respectively. Similar kinetic constants were obtained by measuring the interaction under low and high CAR sensitivities (Figure 41), indicating incident angle does not affect measurement result. To validate the results, we measured the binding pair again with SPR on a gold surface modified with BSA. By fitting the binding curves (Figure 39c), the kinetic constants were determined, with $k_a = (7.6 \pm 1.6) \times 105\ M^{-1} \cdot s^{-1}$, $k_d = (2.0 \pm 0.2) \times 10^{-3}\ s^{-1}$, and $K_D = 2.8 \pm 0.7\ nM$. The kinetic constants obtained from CAR and SPR were close, suggesting CAR as an accurate method for binding kinetics measurements.

As an additional example, we measured the binding of a nucleic acid, microRNA-21 (miRNA-21), which is a biomarker for various cancers,[98] to its complementary DNA (cDNA). The molecular weight of miRNA-21 is 7 kDa, much smaller than proteins, so we set θ_i at a higher angle (61.4 degrees) to increase the sensitivity to $50\ RIU^{-1}$. The glass surface was first modified with streptavidin, and then biotinylated cDNA was immobilized on the surface via biotin-streptavidin conjugation (Figure 39d). We flowed miRNA-21 and buffer sequentially to the surface to measure the association and dissociation of miRNA-21. The CAR response was recorded, and the kinetic constants were obtained by fitting the response curves (Figure 39e). The same interaction was also measured with SPR, and the results are shown in Figure 39f. In principle, the SNR of CAR in the experiment should be several times higher than SPR (Figure 35e), but the results were not as expected. One reason was because of the difference in cDNA surface coverage on glass and gold. We monitored the immobilization of streptavidin and biotinylated cDNA on glass and gold using CAR and SPR respectively and found

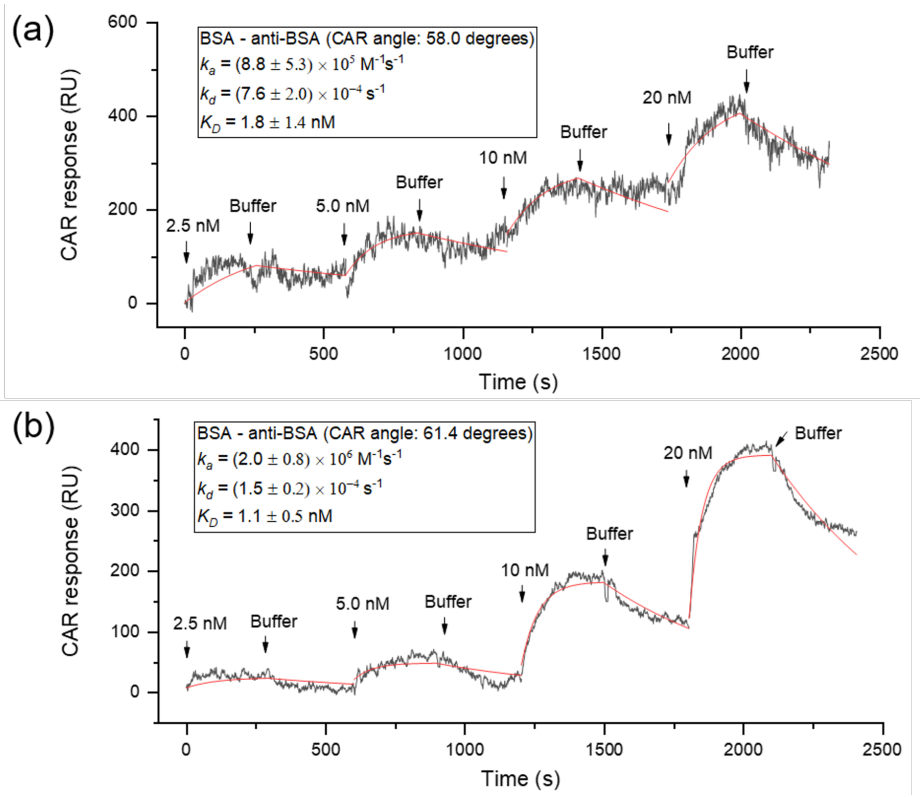

Figure 41. **Measuring anti-BSA binding to BSA at different CAR incident angles.** The incident angle was set at (a) low angle (58.0 degrees) and (b) high angle (61.4 degrees).

that the cDNA coverage on gold was 3.6 times as much as that on glass (Figure 42). Another reason for the unexpected noise in CAR was that the streptavidin sample had some small aggregates that could not be tightly immobilized on the surface, which were washed off and tumbling around the surface in the following miRNA-21 measurement. This phenomenon was only observed in CAR because CAR is more sensitive to particles in bulk solution (see Discussion).

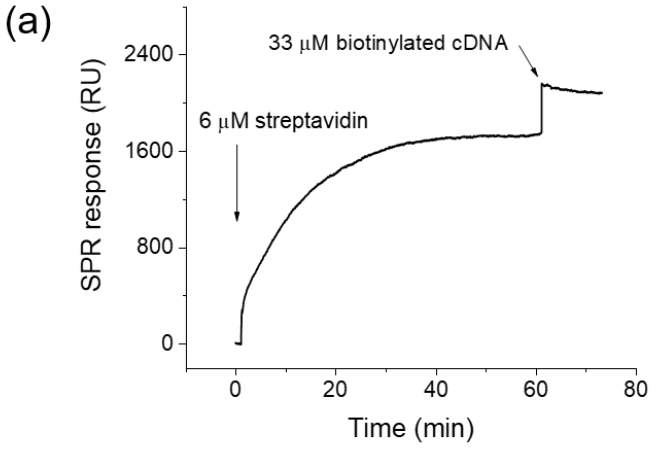

SPR

Sensitivity: $\frac{|\Delta R_p|}{\Delta n_a} \approx 25$

Streptavidin coverage: 1.7×10^{10} molecules/mm^2 (63%)

cDNA coverage: 2.5×10^{10} molecules/mm^2

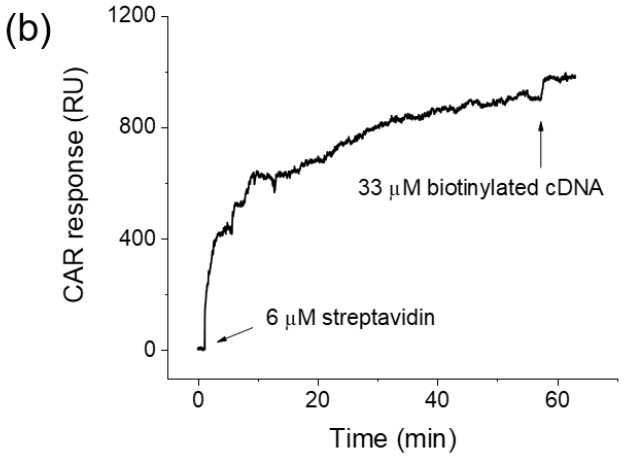

CAR @ ~61.4 degrees

Sensitivity: $\frac{|\Delta R_p|}{\Delta n_a} \approx 50$

Streptavidin coverage: 9.0×10^{9} molecules/mm^2 (33%)

cDNA coverage: 7.0×10^{9} molecules/mm^2

Figure 42. **Surface coverage of streptavidin and cDNA measured with SPR and CAR.** An NHS/EDC activated gold surface was placed on the SPR setup. 6 μM streptavidin was flowed to the surface to induce immobilization of the streptavidin. Then 33 μM biotinylated cDNA was introduced which bound to the surface via biotin-streptavidin conjugation.

Figure 42. (b) Immobilization of streptavidin on an epoxy activated glass surface followed by cDNA conjugation. The concentrations of streptavidin and cDNA are the same as (a). CAR angle was parked at ∼61.4 degrees with a medium-high sensitivity. Note that the fluctuations between 5-12 minutes are due to the floating impurities in solution.

5.3.2 Small Molecule Detection

At higher incident angle close to the critical angle, the enhanced sensitivity and SNR enable CAR to measure smaller molecules that are challenging for SPR. To address this advantage, we measured the interaction between carbonic anhydrase II (CAII) and its small molecule ligands: furosemide (331 Da), sulpiride (341 Da), and methylsulfonamide (95 Da) (Figure 43a). CAII is an enzyme responsible for the catalysis of CO2 hydration, and is found to be related to glaucoma, altitude sickness, obesity and tumor growth.[100] To perform the measurement, we set θ_i at 61.6 degrees with a sensitivity of 112 RIU^{-1}. CAII was immobilized on a glass surface at 5.8% coverage (Figure 44), and the small molecules were flowed over the surface. The binding of each small molecule ligand was measured at several different concentrations and globally fitted to the first order kinetics. The results are shown in Figures 43b-d. The small molecules were also measured with SPR on a gold surface with 6.5% CAII coverage (Figure 44) using the same experimental conditions, but no obvious signal could be found (Figures 43e-g). We note that both the glass surface and the gold surface used for this measurement were modified with a monolayer of protein receptors for fair comparison.

Modifying a three-dimensional matrix such as dextran can further improve the density of the receptors and hence mass change per unit area upon ligand binding.

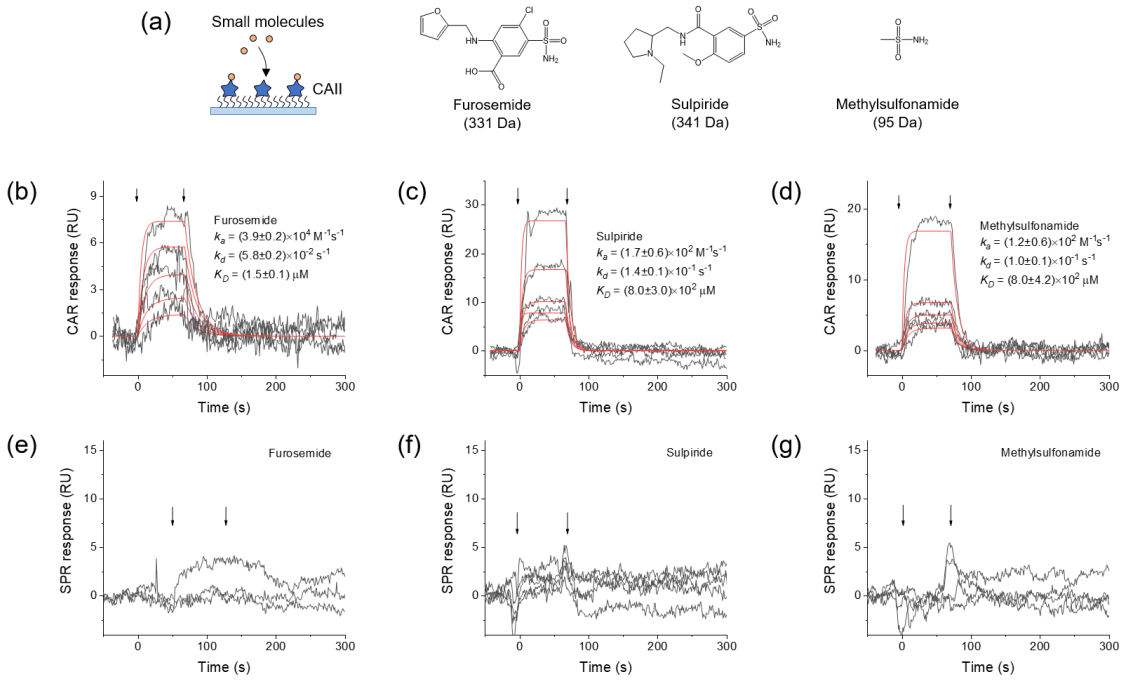

Figure 43. **Measuring the binding kinetics of small molecule ligands to CAII.** a) CAII was immobilized on glass for CAR and gold surface for SPR measurements. Three different small molecules, furosemide (331 Da), sulpiride (341 Da), and methylsulfonamide (95 Da), were flowed over the CAII functionalized chip. (b-d) CAR response curves for furosemide, sulpiride, and methylsulfonamide binding (black curves). The incident angle was set at 61.6 degrees with a sensitivity of 112 RIU^{-1}. The two arrows mark the starting point of association and dissociation, respectively. The red curves are global fittings of the data to the first order binding kinetics. Furosemide concentrations: 234 nM, 469 nM, 938 nM, 1.88 μM, and 3.75 μM; Sulpiride concentrations: 62.5 μM, 125 μM, 250 μM, 500 μM, and 1 mM; Methylsulfonamide concentrations: 156 μM, 312 μM, 625 μM, 1.25 mM, and 2.50 mM. (e-g) Same interactions were measured with SPR but no clear response was observed. The CAII surface coverages were 6.5% and 5.8% for the gold and the glass surfaces, respectively.

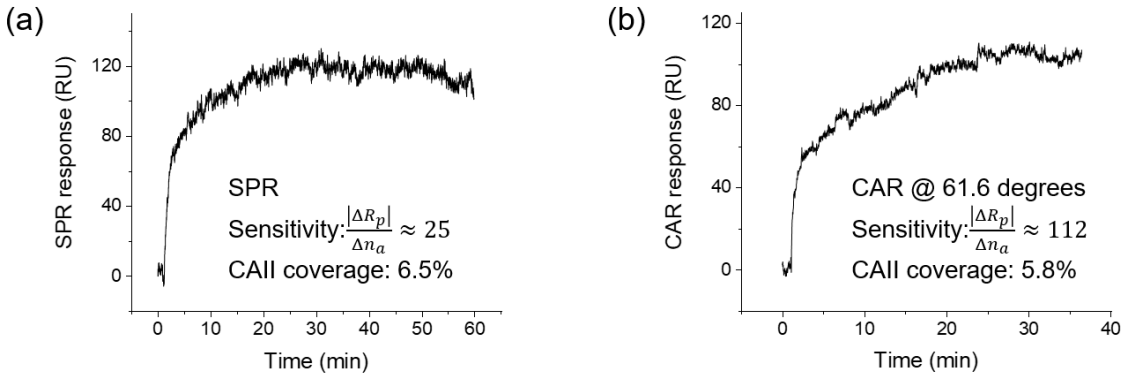

Figure 44. **Surface coverage of CAII on gold and glass surfaces.** CAII immobilization process is monitored by SPR (a) and CAR (b). For CAR measurement, the incident angle is parked at 61.6 degrees, which has a sensitivity of $\sim 112\ RIU^{-1}$. The coverage is estimated to be 6.5% and 5.8% on gold and glass surfaces, respectively. 6 nm is used as the diameter of CAII molecules for the coverage estimation.

Previous studies4 show that the same interactions can be measured with SPR using a dextran coated gold surface, however, the kinetic rate constants were up to 20 times faster than our CAR results. To investigate the discrepancy, we used the same dextran sensor chip and measured the small molecule binding again with SPR. The dextran chip indeed amplified the binding signal. After fitting the kinetics curves, we found that the kinetic rate constants were consistent with our CAR results (Figure 45). Next, we checked the diffusion within the sample delivery system, because slow sample diffusion to the sensor surface can distort the binding curve and lead to false slower kinetics. We examined the sample diffusion time by flowing in 1% ethanol solution (Figure 46), which ideally should generate a sudden change in reflectivity. In reality, the diffusion time is about 5 s, but still much faster than the time scale of association ($\sim$30 s, Figures 43b-d). Therefore, it is not likely that the kinetics is slowed down by diffusion. Also, by fitting the equilibrium state of the interaction (Figure 47), which is not affected by diffusion, K_D is determined to be 1.82 μM, 782 μM and 1.1 mM

for furosemide, sulpiride and methylsulfonamide, consistent with the real-time values. Based on the above analysis, we conclude that the measured kinetic constants are real, and the discrepancy from literature value could be due to different CAII protein sources.

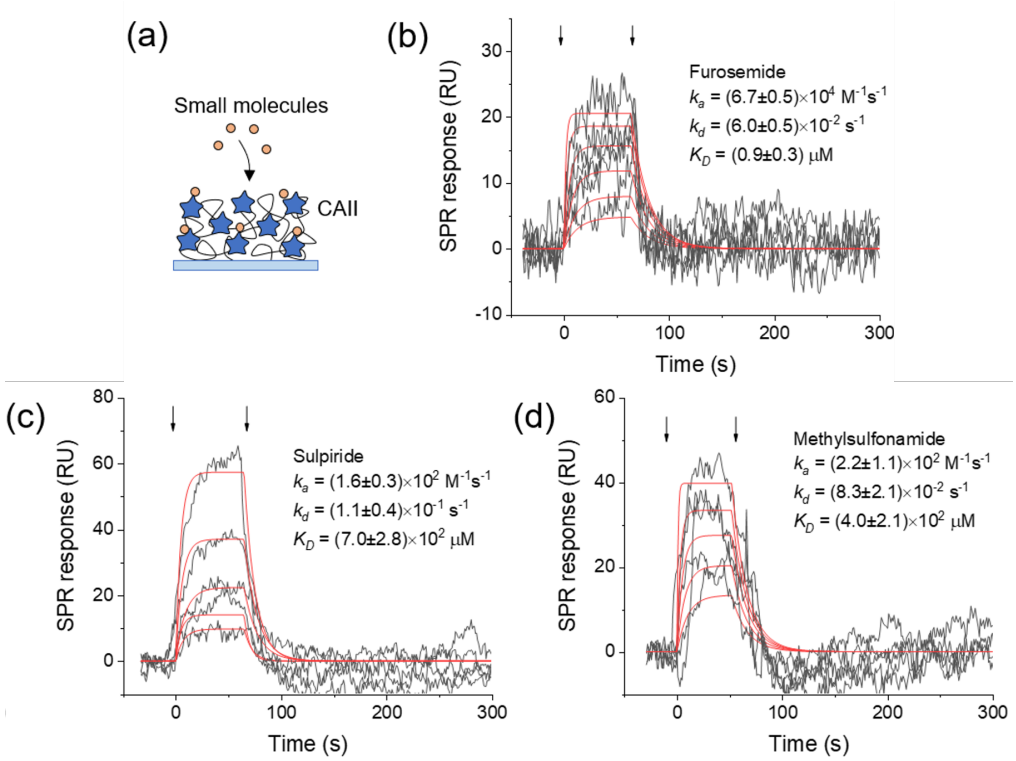

Figure 45. **Measuring small molecules binding to CAII on dextran coated gold surface with SPR.** CAII was immobilized on the dextran using NHS/EDC chemistry. Furosemide (331 Da), sulpiride (341 Da), and methylsulfonamide (95 Da), were flowed over the CAII functionalized surface. (b-d) SPR sensor response curves (black) and fittings (red) for the three small molecules. Furosemide concentrations: 238 nM, 475 nM, 938 nM, 1.88 μM, 3.75 μM, and 7.50 μM; Sulpiride concentrations: 62.5 μM, 125 μM, 250 μM, 500 μM, and 1.00 mM; Methylsulfonamide concentrations: 78.0 μM, 156 μM, 312 μM, 625 μM, and 2.50 mM. Note that the noise level of our result is higher than that in reference [80], which is due to instrument difference. Our SPR instrument is designed for imaging purpose, which does not have a reference flow channel for drift correction.

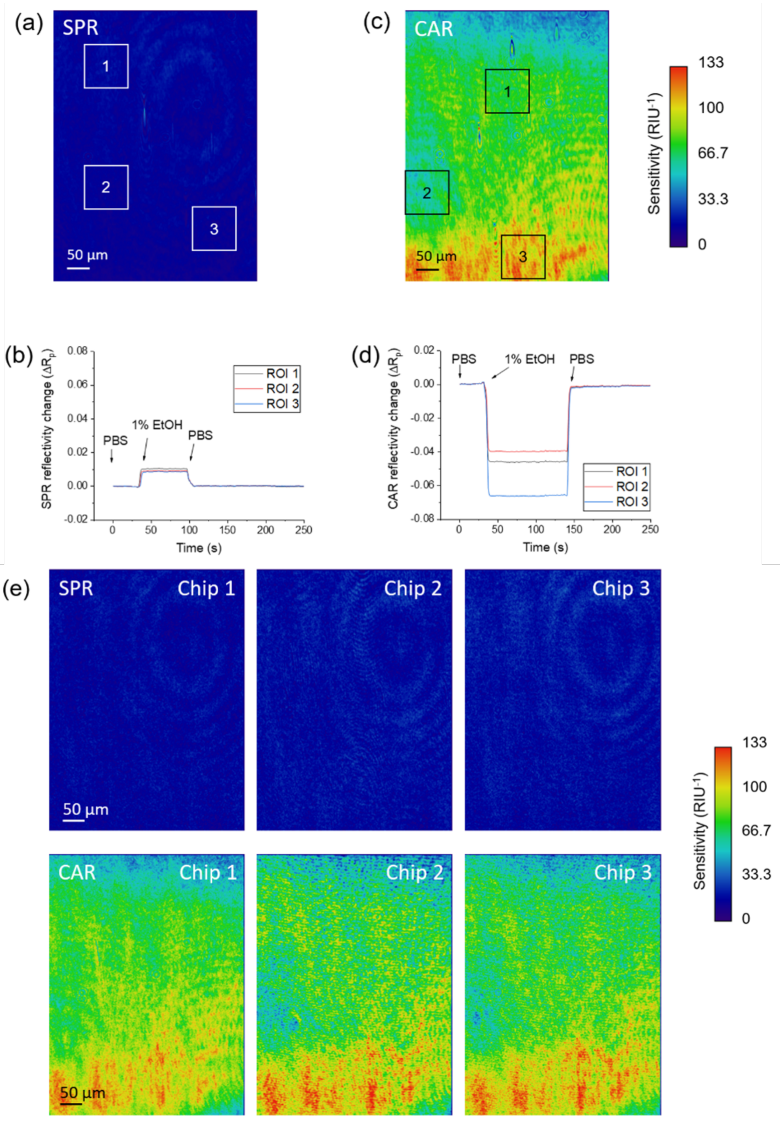

Figure 46. **Surface sensitivity distribution of CAR and SPR.** (a) Spatial distribution of SPR sensitivity obtained by subtracting the images before and after 1% ethanol (final concentration) injection. (b) SPR response (reflectivity change) of the three regions of interests (ROIs) upon 1% ethanol injection.

Figure 46. (c) CAR sensitivity is highly dependent on the incident angle. The angle was parked at 61.5 degrees. The image shows the difference between before and after 1% ethanol injection, from which the sensitivity is calculated. The spatial distribution of sensitivity is non-uniform in vertical direction due to the slight difference in incident angle. (d) CAR response (reflectivity change) of the three ROIs upon 1% ethanol injection. The autosampler including the sample loop has a diffusion delay of less than 10 seconds. (e) Repeatability of the spatial sensitivity distribution. The experiments in (a) and (c) were repeated three times respectively using three different sensor chips and similar patterns were observed, implying the non-uniformity was due to instrument rather than sample.

5.3.3 CAR Imaging of Glycoprotein - Lectin Interaction on Cells

SPR imaging is known for measuring the binding kinetics between cell membrane protein and ligand directly on the cells without the need of protein extraction and purification.[82, 101] Here we demonstrate that CAR imaging is also capable of cell-based measurement. We studied wheat germ agglutinin (WGA) as an example and measured its interaction with glycoproteins on HeLa cells. WGA is a lectin that can specifically bind to N-acetylglucosamine structures in the sugar chain of glycoproteins. Investigating the interactions between lectin and glycoprotein is important for understanding the role of glycoprotein in many biological processes, including cell recognition, adhesion, growth and differentiation.[102]

We first used SPR to measure glycoprotein-WGA interaction on fixed HeLa cells (Figure 48a). The cells were cultured on a gold surface and fixed right before the measurement (Figure 48b). We flowed PBS buffer over the surface to establish a baseline and then introduced 50 μg/ml WGA (Figure 48c). Binding of WGA to the glycoproteins increased the surface refractive index and caused the SPR signal to increase. After the association process, PBS buffer was flowed in again

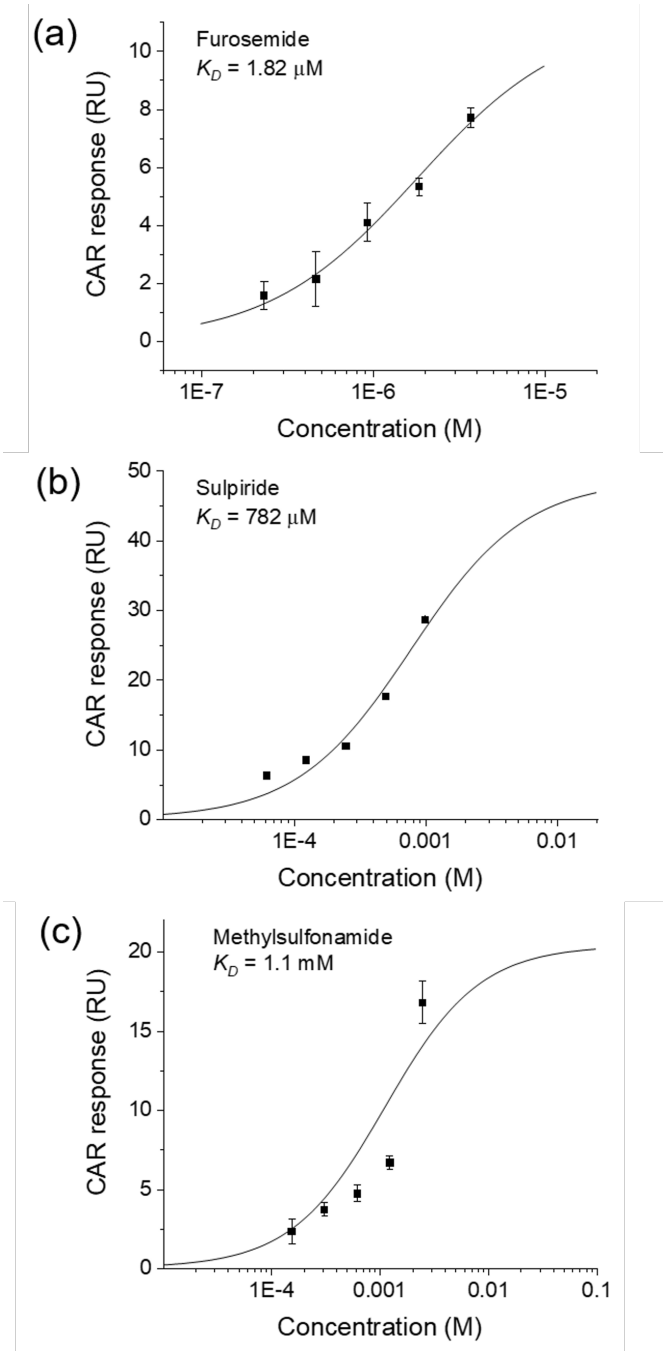

Figure 47. **Equilibrium analysis of furosemide, sulpiride and methylsulfonamide binding to CAII.** The dissociation constants (K_D) are determined by fitting of the data (solid lines), which are 1.82 μM, 782 μM and 1.1 mM, respectively. The error bar represents standard deviation of the maximum response for each concentration in Figure 43.

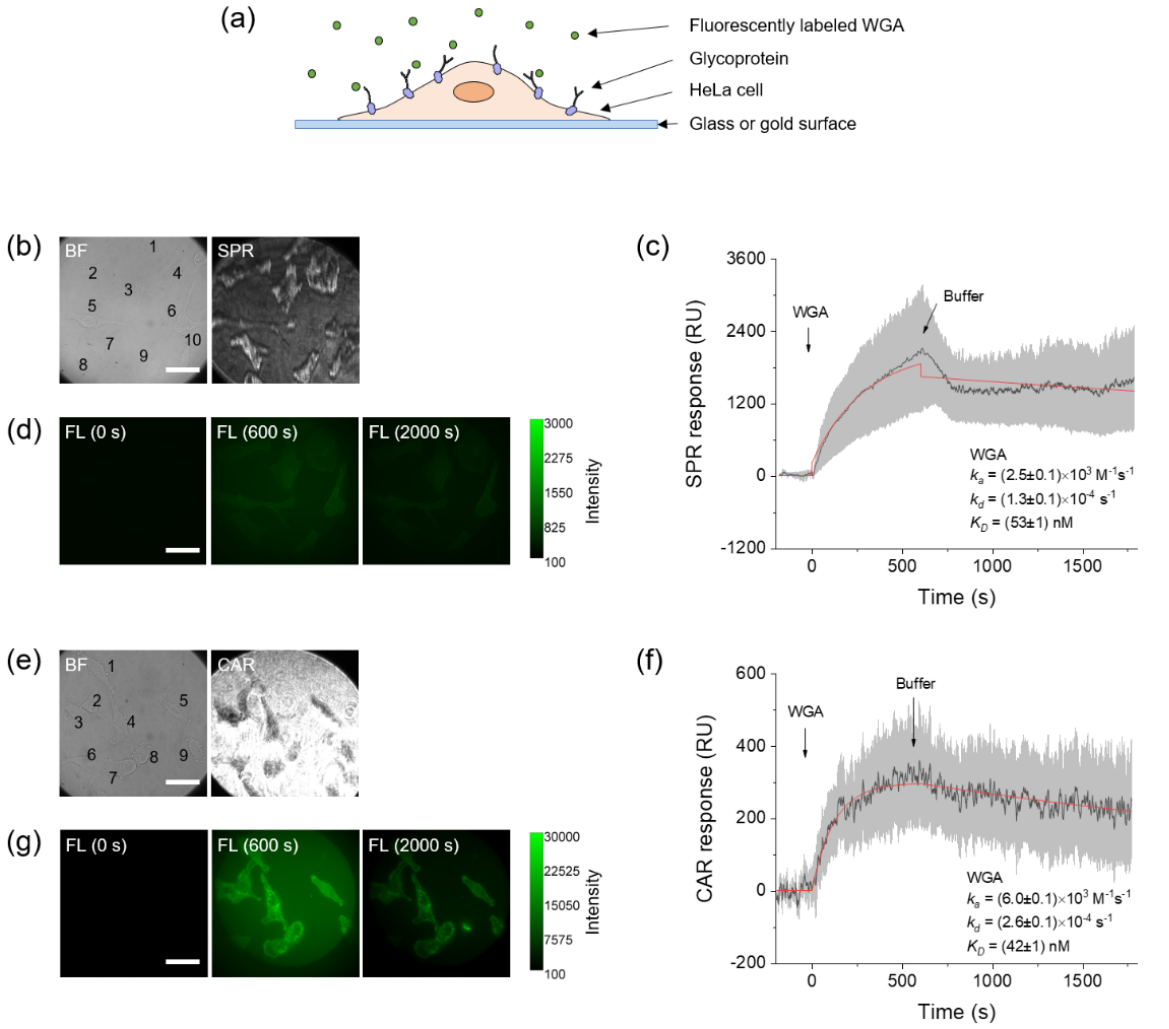

Figure 48. **Measuring WGA binding to glycoproteins on fixed HeLa cells.** (a) HeLa cells were grown on a glass or gold surface for CAR or SPR measurements. The cells were fixed with 4% paraldehyde prior to measurements. Alexa Fluor 488-labeled WGA was flowed over the cells and allowed to bind to the glycoproteins on the cell membrane. (b) Bright field (BF) and SPR images of 10 cells on gold surface. (c) Glycoprotein-WGA binding kinetics measured by SPR. WGA concentration was 50 μg/ml. The black curve and gray shadows are the average SPR signal and standard deviation of the 10 cells (see Figure 49a for details), respectively. The red curve is fitting of the data to the first order kinetics.

Figure 48. (d) Fluorescence (FL) images of the cells captured before WGA binding (0 s), after WGA binding (600 s) and after WGA dissociation (2000 s). Exposure time, 0.1 s. (e) BF and CAR images of 9 cells on glass surface. (f) Glycoprotein-WGA binding kinetics measured by CAR. WGA concentration was 50 μg/ml. The black curve and gray shadows are the average CAR signal and standard deviation of 8 out of the 9 cells (see Figure 49b for details), respectively. The red curve is fitting of the data to the first order kinetics. (g) Fluorescence images of the cells captured before WGA binding (0 s), after WGA binding (600 s) and after WGA dissociation (2000 s). Exposure time, 0.1 s. All the scale bars represent 5 μm.

to induce dissociation of WGA from the cells. The average SPR response of 10 cells was fitted to the first order kinetics, and k_a, k_d, and K_D were determined to be $(2.5 \pm 0.1) \times 10^3\ M^{-1} \cdot s^{-1}$, $(1.3 \pm 0.1) \times 10^{-4}\ s^{-1}$, and $53 \pm 1\ nM$, respectively. The WGA was labeled with Alexa Fluor 488, allowing us to verify the binding using fluorescence. Three fluorescence images were captured at different phases of the binding process: at the baseline, after association, and after dissociation (Figure 48d) respectively. The fluorescence change, although weak, confirmed that the SPR signal was due to the binding.

Next, we used CAR imaging to repeat the glycoprotein-WGA binding measurement. The cells were cultured on a glass surface, and the bright field image and the corresponding CAR image of 9 cells are shown in Figure 48e. The cells show dark patterns because they have higher refractive index than the background. θ_i was set at $\sim$61.0 degrees with similar sensitivity to SPR. Kinetic constants for WGA were determined from the average CAR response of the 9 cells, with $k_a = (6.0 \pm 0.1) \times 10^3\ M^{-1} \cdot s^{-1}$, $k_d = (2.6 \pm 0.1) \times 10^{-4}\ s^{-1}$, and $K_D = 42 \pm 1\ nM$, respectively (Figure 48f). The minor disagreement in kinetic constants might reflect different surfaces and different light illumination depth between SPR and CAR (more in Discussion). Fluorescence images captured during the CAR measurement confirmed the binding of WGA (Figure

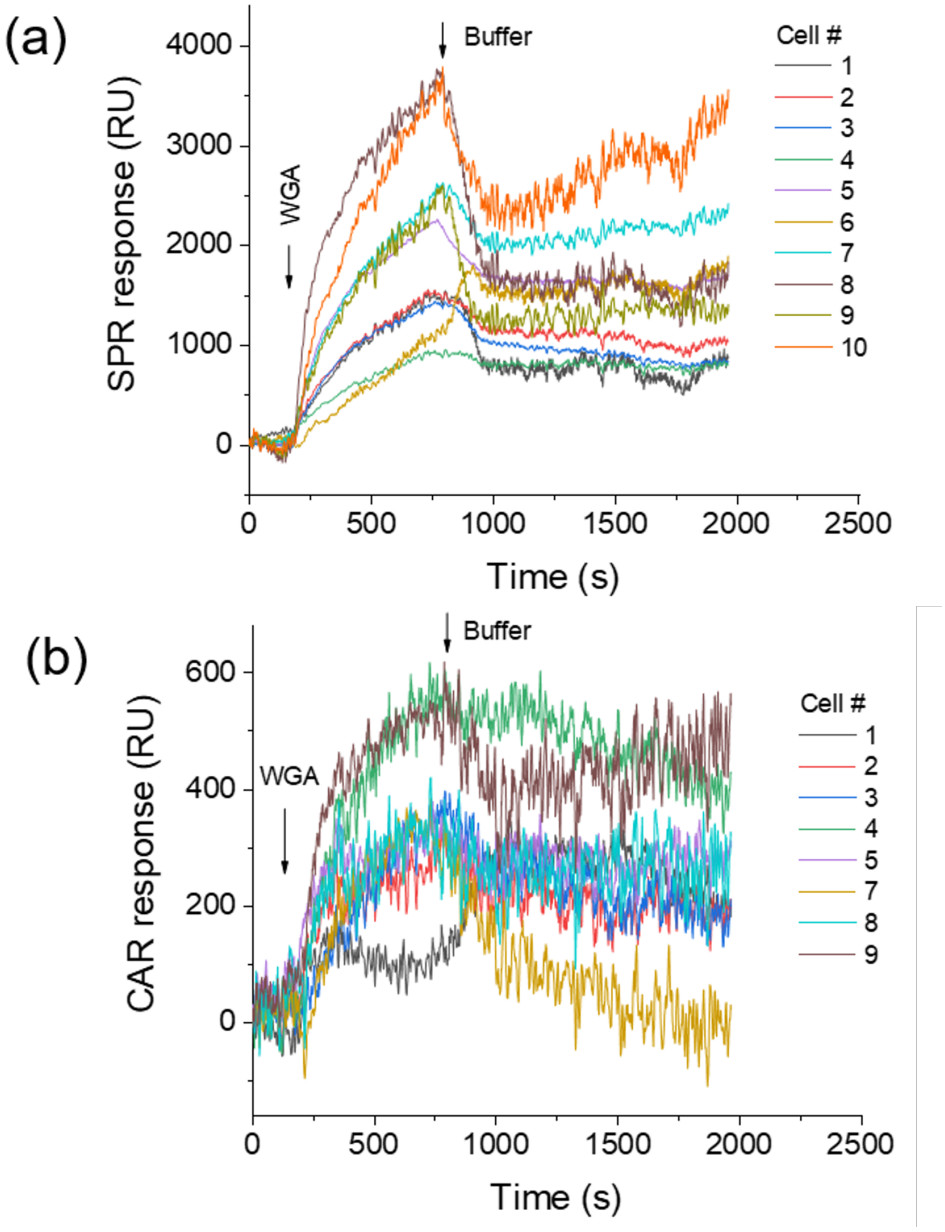

Figure 49. **WGA binding curves of individual fixed HeLa cells measured by SPR (a) and CAR (b).**

48g). Notably, the fluorescence intensity on glass is over 30 times stronger than that on the gold surface, which is expected because the gold film obstructs the transmission of the lights and quenches the fluorescence. For this reason, we believe CAR is more compatible with fluorescence than SPR, and suitable for measuring biological samples that need simultaneous fluorescent labelling.

5.3.4 CAR Imaging of Ion Channel- Small Molecule Interaction on Cells

Most drugs are small molecules, and over 50% drug targets are membrane proteins.[103] SPR imaging can measure interactions directly on cells, but the sensitivity is inadequate for small molecule ligands. This weakness can be compensated by CAR owing to its tunable sensitivity. To demonstrate this capability, we measured the binding kinetics between acetylcholine (182 Da), a small molecule neurotransmitter, and nicotinic acetylcholine receptor (nAChR), an ion channel membrane protein which is responsible for neurotransmission and drug addiction.[104] nAChR was expressed on brain neuroblastoma SH-EP1 cells by transfecting the cells with human $\alpha 4\beta 2$ receptor (SH-EP1_$\alpha 4\beta 2$).[105] In this experiment, we set θ_i at high-sensitivity region (61.6 degrees), and flowed acetylcholine solution over the cells (Figure 50a). The averaged CAR responses of several cells were fitted globally as shown in Figure 50b. The binding of acetylcholine induced negative change to the refractive index on the cell membrane. Although the binding of acetylcholine added mass to the surface, the binding also triggered cell membrane deformation and associated mass movement,[105, 106] which may reduce the effective refractive index on the sensor surface (more in Discussion). The kinetic constants were close to those measured by a cellular membrane

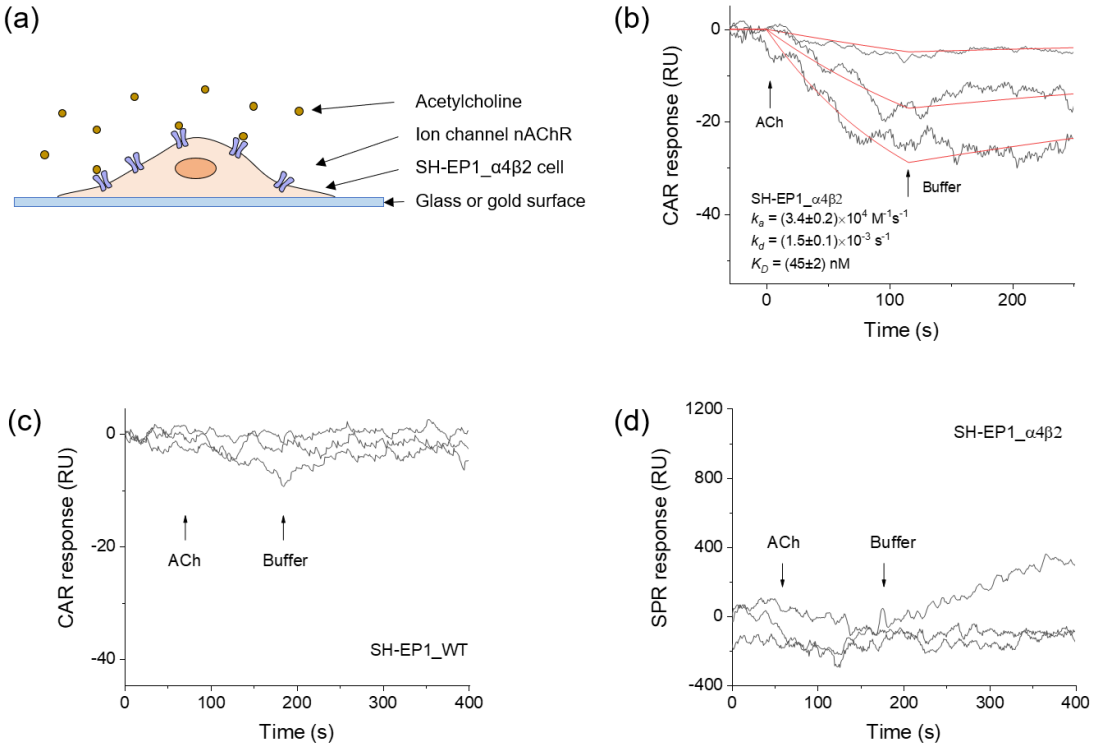

Figure 50. **Measuring acetylcholine binding to nAChR on SH-EP1_$\alpha 4\beta 2$ cells.** (a) SH-EP1_$\alpha 4\beta 2$ cells were grown on a glass or gold surface for CAR or SPR measurements. The cells were fixed with 4% paraldehyde before the measurement. (b) Acetylcholine (ACh) binding to SH-EP1_$\alpha 4\beta 2$ cells measured by CAR. CAR angle was set at 61.6 degrees with a sensitivity of 112 RIU^{-1}. The binding kinetic curves (black) were obtained by averaging the CAR response of 7 cells and globally fitted to the first order kinetics (red) (see Figure 51b for the response of individual cells). Acetylcholine concentrations: 25 nM, 100 nM and 200 nM. (c) Control experiments using wild type SH-EP1 cells which have no nAChR. Acetylcholine and PBS buffer were flowed to the cells as indicated by the arrows. No clear CAR response was observed (see Figure 51d for individual cells). Acetylcholine concentrations: 50 nM, 100 nM and 200 nM. (d) Measuring acetylcholine binding to SH-EP1_$\alpha 4\beta 2$ cells using SPR. No response was observed due to insufficient sensitivity of SPR (see Figure 51f for individual cells). Acetylcholine concentrations: 50 nM, 100 nM and 200 nM.

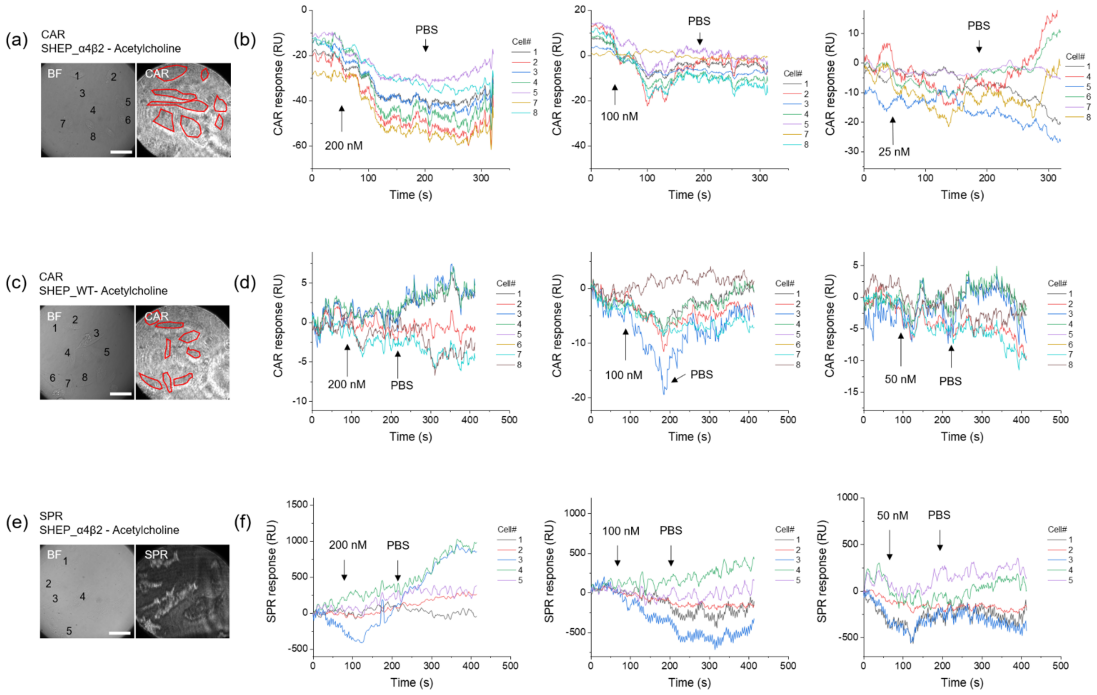

Figure 51. **Measuring acetylcholine-nAChR interaction with CAR and SPR.** (a) Bright field (BF) and CAR images of 8 SH-EP1_$\alpha 4\beta 2$ cells. The incident angle of CAR was parked at 61.6 degrees with high sensitivity of 112 RIU^{-1}. Because the angle was close to the critical angle, the cells (marked in red) only had little difference from the glass background which already reached critical angle. (b) CAR response of the cells upon flowing 200 nM (left), 100 nM (middle) and 25 nM (right) acetylcholine. (c) Control experiments: BF and CAR images of 8 wild type SH-EP1 cells. (d) CAR response of the cells upon flowing 200 nM (left), 100 nM (middle) and 50 nM (right) acetylcholine. (e) Measuring acetylcholine binding with SPR. BF and SPR images of 5 SH-EP1_$\alpha 4\beta 2$ cells. (f) SPR response of the cells upon flowing 200 nM (left), 100 nM (middle) and 50 nM (right) acetylcholine.

deformation detection method.[105, 106] To verify that the CAR signal was indeed due to acetylcholine binding, we performed a control experiment using wild type SH-EP1 cells which does not have nAChR. The CAR response was negligible (Figure 50c). The acetylcholine-nAChR interaction was also measured using SH-EP1_$\alpha 4\beta 2$ cells with SPR, which showed no measurable response due to insufficient sensitivity (Figure 50d).

5.4 Discussion

CAR presents several technical advances compared to SPR in terms of tunable sensitivity and dynamic range, fluorescence capability, and robust glass sensor surface. In this section, we further explore the difference between CAR and SPR and discuss potential benefits and limitations of CAR.

5.4.1 Sensing Distance

CAR has deeper sensing range than SPR, which can be explained by the imaging principles of SPR and CAR. SPR occurs above critical angle, and the evanescent field is coupled by the excited surface plasmon, which concentrates the field in the vicinity of the surface (100-200 nm). In CAR, the evanescent field of CAR is much less confined to the surface in the absence of surface plasmon (Figure 52a). Also, as the incident light is below the critical angle, allowing a portion of light go beyond evanescent field range to further distances. An observation in our experiment shows a good example. We found many moving parabolic patterns inside live cells under

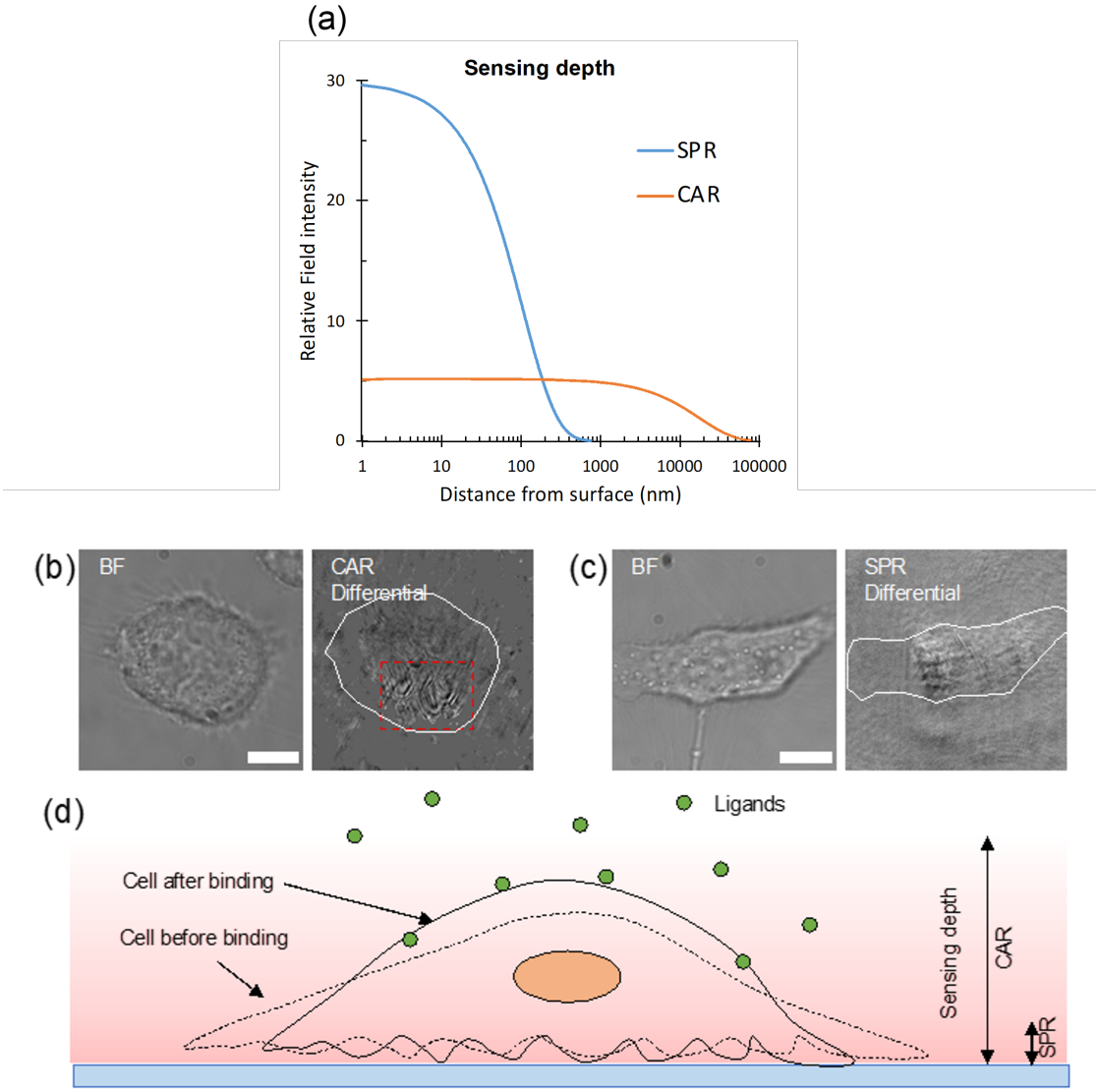

Figure 52. **Sensing depth of CAR and SPR.** (a) Calculated evanescent sensing depth of CARi and SPRi, at critical angle and SPR angle, respectively. (b) Bright field (left) and differential CAR (right) images of a single cell. The differential CAR image was obtained by subtracting two consecutive frames in an image sequence recorded at 10 frames per second. The white line marks the outline of the cell. The parabolic patterns within the cell (marked by the red square) are generated by the motion of organelles.

Figure 52. (c) Bright field (left) and differential SPR images of a single cell. The images were captured and processed under the same condition as in (a). Organelle motion was not revealed by SPR. (d) Schematic picture showing sensing a cell with CAR and SPR. SPR sense the sample with the surface-confined evanescent field and only the bottom section of the sample (several hundred nanometers) can be imaged. CAR has a portion of transmitted light additional to the much deeper evanescent field (tens of micrometers), which enables CAR to detect the binding-induced deformation of whole cell. (d) simulation result of SPR and CAR sensing depth, the incident angle is set at SPR and critical angle, respectively.

CAR illumination, which are organelles such as mitochondria (Figure 52b and Video S3).[107, 108] The parabolic shape arises from the interference between the evanescent wave and scattered light from the organelles.[107, 81] However, such patterns did not appear under SPR illumination (Figure 52c), because the organelles are beyond the detection range of SPR. Regardless of the sensing distance, the refractive index changes above the sensing surface will change the intensity of the reflected light and generate the sensor response (or image contrast) for CAR according to equation 5.1, similar to SPR.

The deeper sensing range also reveals cell deformation caused by ligand binding (Figure 52d).[105, 106] In fact, the CAR signal in WGA binding (Figure 48f) and acetylcholine binding (Figure 50b) reflects surface refractive index change caused by a combined effect of bound ligands induced surface mass increase and dynamic mass redistribution due to binding induced cell deformation. In both cases, ligand binding increases the surface refractive index because the refractive index of the ligand molecules are higher than the buffer solution, and cell deformation decreases the surface refractive index because the mass center of the cell moves away from the surface. The mass of WGA induces more refractive index change than cell deformation, thus the net signal is positive. Acetylcholine is a small molecule and the signal is dominated by cell deformation, so the net CAR signal is negative.

For molecular interaction studies, the longer sensing depth of CAR could pick up background noises from impurities in the sample, because the motion of particles or aggregates in the sample solution will generate noise to the CAR signal (Figures 39e and 42b) but has minimal impact to SPR.

5.4.2 Wavelength and Polarization of Incident Light

Another advantage of CAR over SPR is broader selection of light wavelength. SPR normally uses gold film and incident light with wavelength longer than 600 nm to generate SPR. In contrary, CAR is compatible with any wavelength in the visible range. In practice, shorter wavelength (such as green/blue light) can be employed to achieve better spatial resolution and shorter penetration depth which reduces noise from the solution background. UV light also could be used to further improve the spatial resolution and sensitivity, as proteins and nucleic acids absorb lights in the UV range and the signal will be boosted.[109] However, the optics and the camera also need to be UV compatible, and the UV light may cause damage to the sample.

Unlike SPR which requires p-polarized light, CAR is not limited by light polarization. Both p- and s-polarized lights present similar sensitivity and dynamic range in CAR (Figure 53), indicating CAR measurements can be performed using either or both polarizations at the same time. This capability may allow CAR to measure polarization-sensitive samples and couple with fluorescence anisotropy to determine the orientations and dynamics of molecules.

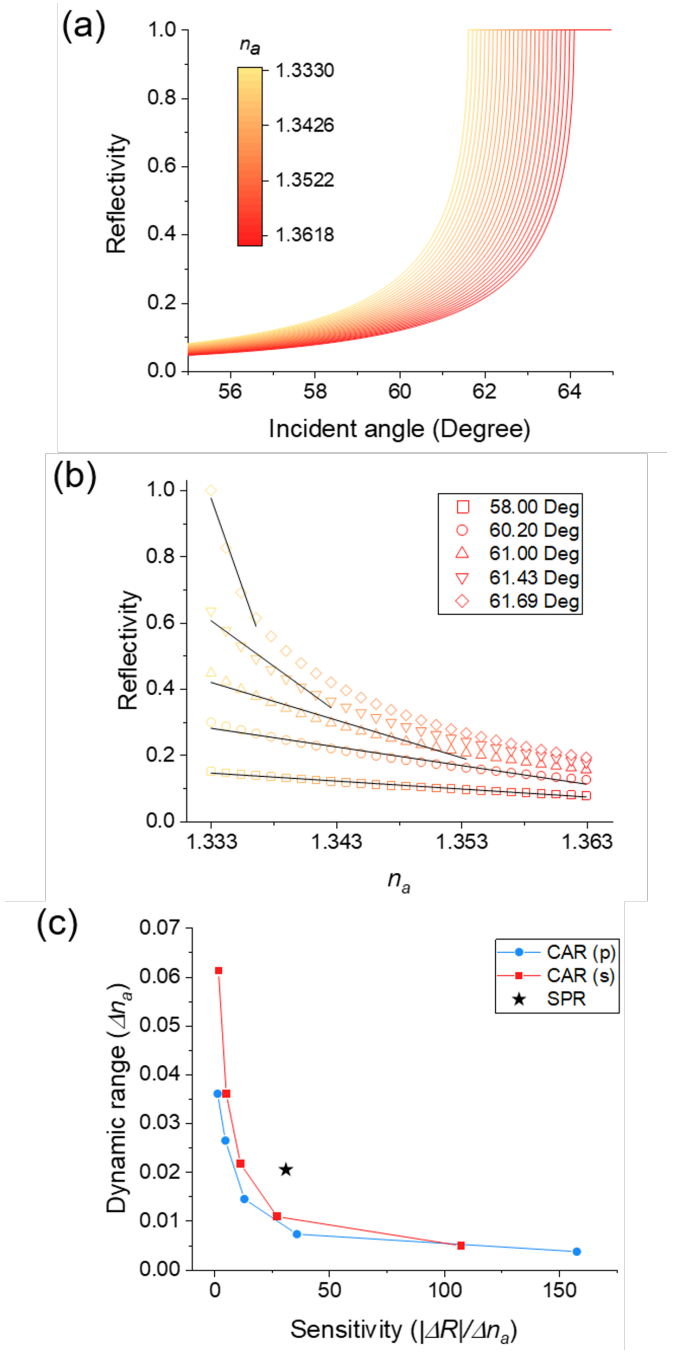

Figure 53. **Simulation results of CAR with s-polarized incident light.**

Figure 53. (a) Relationship between reflectivity and incident angle at different aqueous solution refractive indices (n_a). (b) Reflectivity vs. n_a at five representative incident angles. The black lines are fittings of the linear regions ($R^2 > 0.97$). (c) Sensitivity and dynamic range of CAR with s-polarization (CAR(s)) and p-polarization (CAR(p)) at the five representative angles. The star marks the theoretical sensitivity and dynamic range of SPR. The CAR(p) and SPR data are adopted from Figure 36c

5.4.3 Spatial Sensitivity Distribution

The incident light in SPR imaging setup may not illuminate the surface at perfectly uniform angle, which also varies with different instruments. The slight angle difference can barely affect the sensitivity of SPR because SPR has constant sensitivity near the SPR angle (Figure 46a). For CAR, however, the sensitivity is strongly dependent on the incident angle, and the imperfect illumination could lead to a non-uniform surface sensitivity (Figure 46c). We calibrated the CAR sensitivity of our prism-based setup with 1% ethanol and found that the sensitivity at different regions could differ by up to 4 times. The spatial sensitivity distribution stems from imperfect collimation of light, because the distribution pattern was independent of different sensor chips and samples (Figure 46e). The microscope-based setup showed a more uniform sensitivity because of tunable collimation of incident light and smaller illumination area. For this reason, we always use regions with similar sensitivities when comparing CAR signals in this work.

5.4.4 Detection Limit

Detection limit is determined by the noise level and sensitivity. For CAR at high angle, the noise level is 1.7×10^{-4} (unit: reflectivity) (Figure 38d) and the sensitivity

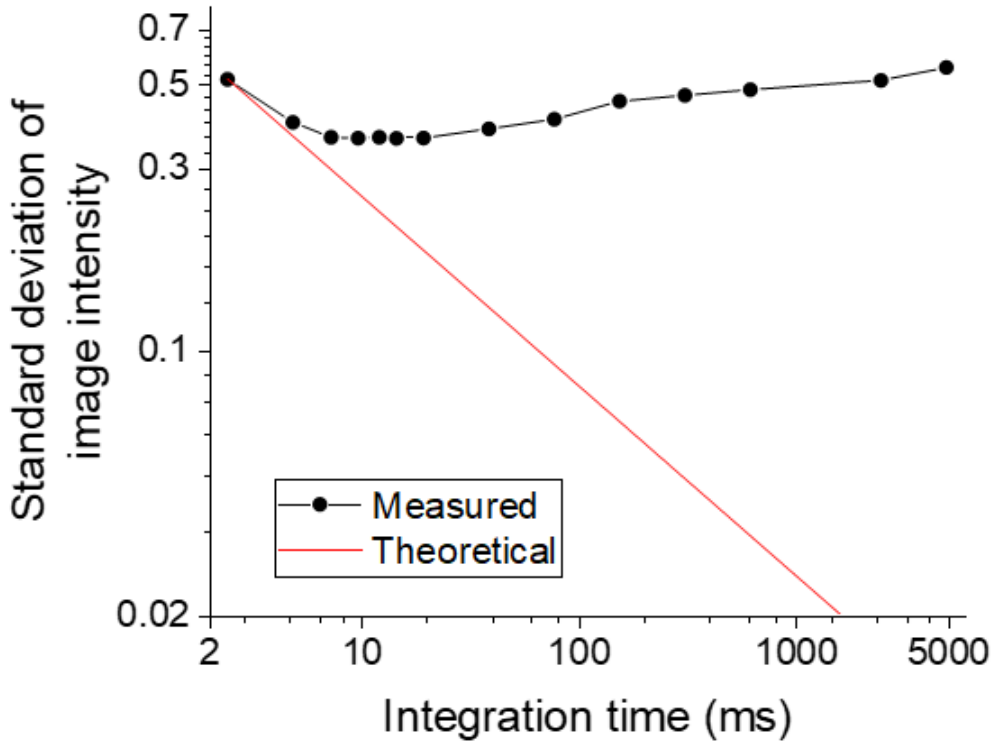

Figure 54. **System noise analysis.** Total noise (black) and shot noise (red) were calculated using a method by Piliarik et al.[110] An image sequence was recorded at 500 frames per second for 1 min. The images were averaged over different periods and the new image sequences were differentiated. Standard deviation of the differentiated image sequence was calculated and plotted vs. the integration time. At 1 s which is the typical sampling rate for biosensors, the total noise is 25 times larger than the shot noise.

is 112 (unit: reflectivity per refractive index unit (RIU^{-1}) (Figure 35d). The noise thus corresponds to 1.5×10^{-6} RIU, or 1.5 RU, or $\sim 1.5 pg/mm^2$ in mass density (biacore ref). Similarly, the noise for SPR is determined to be 2.4 pg/mm^2. The sensitivity is intrinsic property of CAR (at a specific angle) and SPR and could not be changed for a given instrument. Therefore, the only way to lower the detection limit is to reduce noise. In an ideal scenario, the smallest noise for optical sensors is the shot noise, which is due to the quantum nature of light. To reach shot noise limit, all other types of noise need to be well under control, such as light source noise and

environmental and system mechanical noise. We calculated the theoretical shot noise for our prism-based setup to be 25 times lower than the measured noise (Figure 54). The identified major noise source is mechanical noise from the system cooling fans. Therefore, over an order of magnitude lower detection limit could be reached if the system mechanical noise is reduced with a quiet cooling design.

5.5 Conclusion

We have developed a label-free optical sensing method called CAR imaging to quantify molecular binding kinetics on a cover glass surface. CAR measures the reflectivity change near critical angle in response to molecular binding induced refractive index changes on the sensor surface. The sensitivity and dynamic range of CAR is tunable by varying the incident angle of light, which allows optimizing the measurement for ligands with different sizes in both biomolecular and cell-based studies. CAR also has longer vertical sensing range than SPR due to deeper light penetration depth. Compared to the gold coated SPR sensor chips, the glass CAR sensor chips require no surface fabrication and fully compatible with fluorescence imaging, providing the capability of simultaneous fluorescence imaging. Broader wavelength and polarization selection of CAR may also lead to new applications. Since CAR imaging measurements can be performed on an SPR imaging setup with minimal efforts, we anticipate CAR imaging will become a useful addition to SPR imaging in terms of expanding the capability in small molecule detection, cell-based sensing and simultaneous fluorescence imaging.

Chapter 6

CONCLUSIONS AND PERSPECTIVE

The CSOD system with enhanced electrical field at the sensing area allows the charge sensitive optical detection carried out in normal buffer for the first time. It is demonstrated the system's capability on the detection of both large and small molecules, including quantification of binding kinetics of small molecule ligands and virion displayed GPCRs. The binding kinetics measured in normal and diluted buffer were compared and it was found that the diluted buffer reduced the affinity of the bound pair, likely due to the increased electrostatic repulsion force between the negatively charged ligands and receptors. The capability of measure in normal buffer will also favor the adoption of charge sensitive detection technology for broader applications. Furthermore, the CSOD system was optimized using large diameter fiber and fast detector. This microplate compatible detection was combined with phage display technology for drug screening. It was shown that CSOD can be used to distinguish different binding kinetics of different peptides displayed by phage display technology. The kinetic data were validated by the SPR measured purified peptide data. This method can be incorporated into a diversity display pipeline and increase the productivity of library screening. The fast detector and microplate compatibility brings high-throughput potential to CSOD. To further increase CSOD capability, normal buffer detection and fast detector detection can be combined together with some optimization of the well design.

The mass based label-free optical sensing method called CAR is able to quantify molecular binding kinetics on a cover glass surface. CAR measures the reflectivity

change near critical angle in response to molecular binding induced refractive index changes on the sensor surface. The sensitivity and dynamic range of CAR is tunable by varying the incident angle of light, which allows optimization of the measurement for ligands with different sizes in both biomolecular and cell-based studies. CAR also has longer vertical sensing range than SPR due to deeper light penetration depth. Compared to the gold coated SPR sensor chips, the glass CAR sensor chips require no surface fabrication and fully compatible with fluorescence imaging, providing the capability of simultaneous fluorescence imaging. Broader wavelength and polarization selection of CAR may also lead to new applications. Since CAR imaging measurements can be performed on an SPR imaging setup with minimal efforts, we anticipate CAR imaging will become a useful addition to SPR imaging in terms of expanding the capability of small molecule detection, cell-based sensing and simultaneous fluorescence imaging.

REFERENCES

[1] R. A. Copeland. "Evaluation of enzyme inhibitors in drug discovery. A guide for medicinal chemists and pharmacologists". In: *Methods Biochem Anal* 46 (2005), pp. 1–265.

[2] Wei Qi et al. "Selective inhibition of Ezh2 by a small molecule inhibitor blocks tumor cells proliferation". In: *Proceedings of the National Academy of Sciences* 109.52 (2012), pp. 21360–21365. DOI: 10.1073/pnas.1210371110. URL: https://www.pnas.org/content/pnas/109/52/21360.full.pdf.

[3] Bernd Reisinger et al. "Exploiting Protein Symmetry To Design Light-Controllable Enzyme Inhibitors". In: *Angewandte Chemie International Edition* 53.2 (2014), pp. 595–598. DOI: 10.1002/anie.201307207. URL: https://doi.org/10.1002/anie.201307207.

[4] Chia-Yung Wu et al. "Remote control of therapeutic T cells through a small molecule–gated chimeric receptor". In: *Science* 350.6258 (2015), aab4077. DOI: 10.1126/science.aab4077. URL: https://science.sciencemag.org/content/sci/350/6258/aab4077.full.pdf.

[5] M. Okada-Iwabu et al. "A small-molecule AdipoR agonist for type 2 diabetes and short life in obesity". In: *Nature* 503.7477 (2013), pp. 493–9. DOI: 10.1038/nature12656.

[6] H. J. Sharpe et al. "Regulation of the oncoprotein Smoothened by small molecules". In: *Nat Chem Biol* 11.4 (2015), pp. 246–55. DOI: 10.1038/nchembio.1776.

[7] Robert A. Copeland. "The drug–target residence time model: a 10-year retrospective". In: *Nature Reviews Drug Discovery* 15.2 (2016), pp. 87–95. DOI: 10.1038/nrd.2015.18. URL: https://doi.org/10.1038/nrd.2015.18.

[8] Mattia Bernetti et al. "Kinetics of Drug Binding and Residence Time". In: *Annual Review of Physical Chemistry* 70.1 (2019), pp. 143–171. DOI: 10.1146/annurev-physchem-042018-052340. URL: https://doi.org/10.1146/annurev-physchem-042018-052340.

[9] Ashwani K. Sharma, Alexandra D. Kent, and Jennifer M. Heemstra. "Enzyme-Linked Small-Molecule Detection Using Split Aptamer Ligation". In: *Analytical Chemistry* 84.14 (2012), pp. 6104–6109. DOI: 10.1021/ac300997q. URL: https://doi.org/10.1021/ac300997q.

[10] Jiajie Liang et al. "Aggregated Silver Nanoparticles Based Surface-Enhanced Raman Scattering Enzyme-Linked Immunosorbent Assay for Ultrasensitive Detection of Protein Biomarkers and Small Molecules". In: *Analytical Chemistry* 87.11 (2015), pp. 5790–5796. DOI: 10.1021/acs.analchem.5b01011. URL: https://doi.org/10.1021/acs.analchem.5b01011.

[11] Christoph J. Wienken et al. "Protein-binding assays in biological liquids using microscale thermophoresis". In: *Nature Communications* 1.1 (2010), p. 100. DOI: 10.1038/ncomms1093. URL: https://doi.org/10.1038/ncomms1093.

[12] Jiři Homola, Sinclair S. Yee, and Günter Gauglitz. "Surface plasmon resonance sensors: review". In: *Sensors and Actuators B: Chemical* 54.1 (1999), pp. 3–15. DOI: https://doi.org/10.1016/S0925-4005(98)00321-9. URL: http://www.sciencedirect.com/science/article/pii/S0925400598003219.

[13] C. A. Wartchow et al. "Biosensor-based small molecule fragment screening with biolayer interferometry". In: *J Comput Aided Mol Des* 25.7 (2011), pp. 669–76. DOI: 10.1007/s10822-011-9439-8.

[14] Darryl J. Bornhop et al. "Free-Solution, Label-Free Molecular Interactions Studied by Back-Scattering Interferometry". In: *Science* 317.5845 (2007), pp. 1732–1736. DOI: 10.1126/science.1146559. URL: https://science.sciencemag.org/content/sci/317/5845/1732.full.pdf.

[15] M. M. Baksh et al. "Label-free quantification of membrane-ligand interactions using backscattering interferometry". In: *Nat Biotechnol* 29.4 (2011), pp. 357–60. DOI: 10.1038/nbt.1790.

[16] S. T. Jepsen et al. "Evaluation of back scatter interferometry, a method for detecting protein binding in solution". In: *Analyst* 140.3 (2015), pp. 895–901. DOI: 10.1039/c4an01129e.

[17] P. Kozma et al. "Integrated planar optical waveguide interferometer biosensors: a comparative review". In: *Biosens Bioelectron* 58 (2014), pp. 287–307. DOI: 10.1016/j.bios.2014.02.049.

[18] N. J. Cho et al. "Quartz crystal microbalance with dissipation monitoring of supported lipid bilayers on various substrates". In: *Nat Protoc* 5.6 (2010), pp. 1096–106. DOI: 10.1038/nprot.2010.65.

[19] Roland G. Heym et al. "Label-free detection of small-molecule binding to a GPCR in the membrane environment". In: *Biochimica et Biophysica Acta (BBA) - Proteins and Proteomics* 1854.8 (2015), pp. 979–986. DOI: https:

//doi.org/10.1016/j.bbapap.2015.04.003. URL: http://www.sciencedirect.com/science/article/pii/S1570963915000990.

[20] M. Perpeet et al. "SAW Sensor System for Marker-Free Molecular Interaction Analysis". In: *Analytical Letters* 39.8 (2006), pp. 1747–1757. DOI: 10.1080/000327106006714063. URL: https://doi.org/10.1080/000327106006714063.

[21] A. C. Pan et al. "Molecular determinants of drug-receptor binding kinetics". In: *Drug Discov Today* 18.13-14 (2013), pp. 667–73. DOI: 10.1016/j.drudis.2013.02.007.

[22] S. Aydin. "A short history, principles, and types of ELISA, and our laboratory experience with peptide/protein analyses using ELISA". In: *Peptides* 72 (2015), pp. 4–15. DOI: 10.1016/j.peptides.2015.04.012.

[23] Web Page. 2017. URL: https://www.bosterbio.com/newsletter-archive/20170728-which-elisa.

[24] Stephanie D. Gan and Kruti R. Patel. "Enzyme immunoassay and enzyme-linked immunosorbent assay". In: *The Journal of investigative dermatology* 133.9 (2013), e12. DOI: 10.1038/jid.2013.287. URL: http://europepmc.org/abstract/MED/23949770%20https://doi.org/10.1038/jid.2013.287.

[25] Jiří Homola. "Surface Plasmon Resonance Sensors for Detection of Chemical and Biological Species". In: *Chemical Reviews* 108.2 (2008), pp. 462–493. DOI: 10.1021/cr068107d. URL: https://doi.org/10.1021/cr068107d.

[26] Jiři Homola, Sinclair S. Yee, and Günter Gauglitz. "Surface plasmon resonance sensors: review". In: *Sensors and Actuators B: Chemical* 54.1 (1999), pp. 3–15. DOI: https://doi.org/10.1016/S0925-4005(98)00321-9. URL: http://www.sciencedirect.com/science/article/pii/S0925400598003219.

[27] Web Page. 2006. URL: http://biosensingusa.com/technical-notes/technical-note-101-principle-spr-detection-intensity-profile-shift-spr-angle/.

[28] Y. S. Day et al. "Direct comparison of binding equilibrium, thermodynamic, and rate constants determined by surface- and solution-based biophysical methods". In: *Protein Sci* 11.5 (2002), pp. 1017–25. DOI: 10.1110/ps.4330102.

[29] Naoki Kanoh et al. "SPR Imaging of Photo-Cross-Linked Small-Molecule Arrays on Gold". In: *Analytical Chemistry* 78.7 (2006), pp. 2226–2230. DOI: 10.1021/ac051777j. URL: https://doi.org/10.1021/ac051777j.

[30] R. Karlsson et al. “Biosensor analysis of drug-target interactions: direct and competitive binding assays for investigation of interactions between thrombin and thrombin inhibitors”. In: *Anal Biochem* 278.1 (2000), pp. 1–13. DOI: 10.1006/abio.1999.4406.

[31] Helena Nordin et al. “Kinetic studies of small molecule interactions with protein kinases using biosensor technology”. In: *Analytical biochemistry* 340.2 (2005), pp. 359–368. DOI: 10.1016/j.ab.2005.02.027. URL: http://europepmc.org/abstract/MED/15840510%20https://doi.org/10.1016/j.ab.2005.02.027.

[32] D. J. Bornhop et al. “Free-solution, label-free molecular interactions studied by back-scattering interferometry”. In: *Science* 317.5845 (2007), pp. 1732–6. DOI: 10.1126/science.1146559.

[33] Darryl J. Bornhop et al. “Origin and prediction of free-solution interaction studies performed label-free”. In: *Proceedings of the National Academy of Sciences* 113.12 (2016), E1595. DOI: 10.1073/pnas.1515706113. URL: http://www.pnas.org/content/113/12/E1595.abstract.

[34] J. P. Overington, B. Al-Lazikani, and A. L. Hopkins. “How many drug targets are there?” In: *Nat Rev Drug Discov* 5.12 (2006), pp. 993–6. DOI: 10.1038/nrd2199.

[35] Jean-Luc Popot. “Amphipols, Nanodiscs, and Fluorinated Surfactants: Three Nonconventional Approaches to Studying Membrane Proteins in Aqueous Solutions”. In: *Annual Review of Biochemistry* 79.1 (2010), pp. 737–775. DOI: 10.1146/annurev.biochem.052208.114057. URL: https://doi.org/10.1146/annurev.biochem.052208.114057.

[36] Jasmina Minic et al. “Immobilization of native membrane-bound rhodopsin on biosensor surfaces”. In: *Biochimica et Biophysica Acta (BBA) - General Subjects* 1724.3 (2005), pp. 324–332. DOI: https://doi.org/10.1016/j.bbagen.2005.04.017. URL: http://www.sciencedirect.com/science/article/pii/S0304416505001091.

[37] I. G. Denisov et al. “Directed Self-Assembly of Monodisperse Phospholipid Bilayer Nanodiscs with Controlled Size”. In: *Journal of the American Chemical Society* 126.11 (2004), pp. 3477–3487. DOI: 10.1021/ja0393574. URL: https://doi.org/10.1021/ja0393574.

[38] Guan-Da Syu et al. “Development and application of a high-content virion display human GPCR array”. In: *Nature Communications* 10.1 (2019), p. 1997. DOI: 10.1038/s41467-019-09938-9. URL: https://doi.org/10.1038/s41467-019-09938-9.

[39] J. Borch et al. “Nanodiscs for immobilization of lipid bilayers and membrane receptors: kinetic analysis of cholera toxin binding to a glycolipid receptor”. In: *Anal Chem* 80.16 (2008), pp. 6245–52. DOI: 10.1021/ac8000644.

[40] Y. Guan et al. “Detection of molecular binding via charge-induced mechanical response of optical fibers”. In: *Chem Sci* 5.11 (2014), pp. 4375–4381. DOI: 10.1039/c4sc01188k.

[41] G. Ma et al. “Study of Small-Molecule-Membrane Protein Binding Kinetics with Nanodisc and Charge-Sensitive Optical Detection”. In: *Anal Chem* 88.4 (2016), pp. 2375–9. DOI: 10.1021/acs.analchem.5b04366.

[42] Juliana Cecchetto et al. “Serological point-of-care and label-free capacitive diagnosis of dengue virus infection”. In: *Biosensors and Bioelectronics* 151 (2020), p. 111972. DOI: https://doi.org/10.1016/j.bios.2019.111972. URL: http://www.sciencedirect.com/science/article/pii/S0956566319310498.

[43] Rui Campos et al. “Attomolar Label-Free Detection of DNA Hybridization with Electrolyte-Gated Graphene Field-Effect Transistors”. In: *ACS Sensors* 4.2 (2019), pp. 286–293. DOI: 10.1021/acssensors.8b00344. URL: https://doi.org/10.1021/acssensors.8b00344.

[44] Li Hou et al. “A competitive immunoassay for electrochemical impedimetric determination of chlorpyrifos using a nanogold-modified glassy carbon electrode based on enzymatic biocatalytic precipitation”. In: *Microchimica Acta* 187.4 (2020), p. 204. DOI: 10.1007/s00604-020-4175-1. URL: https://doi.org/10.1007/s00604-020-4175-1.

[45] Loubna Bounab et al. “Effective monitoring of the electro-Fenton degradation of phenolic derivatives by differential pulse voltammetry on multi-walled-carbon nanotubes modified screen-printed carbon electrodes”. In: *Applied Catalysis B: Environmental* 180 (2016), pp. 544–550. DOI: https://doi.org/10.1016/j.apcatb.2015.07.011. URL: http://www.sciencedirect.com/science/article/pii/S0926337315300242.

[46] Xuexin Duan et al. “Quantification of the affinities and kinetics of protein interactions using silicon nanowire biosensors”. In: *Nature Nanotechnology* 7.6 (2012), pp. 401–407. DOI: 10.1038/nnano.2012.82. URL: https://doi.org/10.1038/nnano.2012.82.

[47] Christos P. Papaneophytou et al. “Quantification of the Effects of Ionic Strength, Viscosity, and Hydrophobicity on Protein–Ligand Binding Affinity”. In: *ACS*

Medicinal Chemistry Letters 5.8 (2014), pp. 931–936. DOI: 10.1021/ml500204e. URL: https://doi.org/10.1021/ml500204e.

[48] G. Ma et al. "Measuring Ligand Binding Kinetics to Membrane Proteins Using Virion Nano-oscillators". In: *J Am Chem Soc* 140.36 (2018), pp. 11495–11501. DOI: 10.1021/jacs.8b07461.

[49] G. D. Short and Edmund Bishop. "Concentration Overpotentials on Antimony Electrodes in Differential Electrolytic Potentiometry". In: *Analytical Chemistry* 37.8 (1965), pp. 962–967. DOI: 10.1021/ac60227a003. URL: https://doi.org/10.1021/ac60227a003.

[50] Allen J. Bard. "Electrochemical methods : fundamentals and applications". In: *Electrochemical methods :* (2002).

[51] Alhassan Salami Tijani, Nur Afiqah Binti Kamarudin, and Fatin Athirah Binti Mazlan. "Investigation of the effect of charge transfer coefficient (CTC) on the operating voltage of polymer electrolyte membrane (PEM) electrolyzer". In: *International Journal of Hydrogen Energy* 43.19 (2018), pp. 9119–9132. DOI: https://doi.org/10.1016/j.ijhydene.2018.03.111. URL: http://www.sciencedirect.com/science/article/pii/S0360319918309017.

[52] Ivo Paseka. "Influence of hydrogen absorption in amorphous Ni–P electrodes on double layer capacitance and charge transfer coefficient of hydrogen evolution reaction". In: *Electrochimica Acta* 44.25 (1999), pp. 4551–4558. DOI: https://doi.org/10.1016/S0013-4686(99)00185-1. URL: http://www.sciencedirect.com/science/article/pii/S0013468699001851.

[53] A. Doménech-Carbó et al. "Electrochemical analysis of the alterations in copper pigments using charge transfer coefficient/peak potential diagrams. Application to microsamples of baroque wall paintings attached to polymer film electrodes". In: *Fresenius' Journal of Analytical Chemistry* 369.7 (2001), pp. 576–581. DOI: 10.1007/s002160100736. URL: https://doi.org/10.1007/s002160100736.

[54] C. Y. Biaku et al. "A semiempirical study of the temperature dependence of the anode charge transfer coefficient of a 6kW PEM electrolyzer". In: *International Journal of Hydrogen Energy* 33.16 (2008), pp. 4247–4254. DOI: https://doi.org/10.1016/j.ijhydene.2008.06.006. URL: http://www.sciencedirect.com/science/article/pii/S0360319908007118.

[55] Q. Shi, Y. Zhou, and Y. Sun. "Influence of pH and ionic strength on the steric mass-action model parameters around the isoelectric point of protein". In: *Biotechnol Prog* 21.2 (2005), pp. 516–23. DOI: 10.1021/bp049735o.

[56] C. Wang, J. Wang, and L. Deng. "Evaluating interaction forces between BSA and rabbit anti-BSA in sulphathiazole sodium, tylosin and levofloxacin solution by AFM". In: *Nanoscale Res Lett* 6.1 (2011), p. 579. DOI: 10.1186/1556-276x-6-579.

[57] J. E. Lauckner et al. "GPR55 is a cannabinoid receptor that increases intracellular calcium and inhibits M current". In: *Proc Natl Acad Sci U S A* 105.7 (2008), pp. 2699–704. DOI: 10.1073/pnas.0711278105.

[58] G. Ma et al. "Measuring Ligand Binding Kinetics to Membrane Proteins Using Virion Nano-oscillators". In: *J Am Chem Soc* 140.36 (2018), pp. 11495–11501. DOI: 10.1021/jacs.8b07461.

[59] C. M. Henstridge. "Off-target cannabinoid effects mediated by GPR55". In: *Pharmacology* 89.3-4 (2012), pp. 179–87. DOI: 10.1159/000336872.

[60] B. Isin et al. "Identifying ligand binding conformations of the 2-adrenergic receptor by using its agonists as computational probes". In: *PLoS One* 7.12 (2012), e50186. DOI: 10.1371/journal.pone.0050186.

[61] Ping-Wei Chen et al. "Detecting Protein–Ligand Interaction from Integrated Transient Induced Molecular Electronic Signal (i-TIMES)". In: *Analytical Chemistry* 92.5 (2020), pp. 3852–3859. DOI: 10.1021/acs.analchem.9b05310. URL: https://doi.org/10.1021/acs.analchem.9b05310.

[62] SABYASACHI GHOSH. Accessed: 06-17-2020. 2016. URL: https://www.teknoscienze.com/tks_article/peptide-therapeutics-market-forecast-and-analysis-2015-2025/.

[63] P. Vlieghe et al. "Synthetic therapeutic peptides: science and market". In: *Drug Discov Today* 15.1-2 (2010), pp. 40–56. DOI: 10.1016/j.drudis.2009.10.009.

[64] J. Sheehan and W. A. Marasco. "Phage and Yeast Display". In: *Microbiol Spectr* 3.1 (2015), Aid-0028–2014. DOI: 10.1128/microbiolspec.AID-0028-2014.

[65] R. Tonikian et al. "Identifying specificity profiles for peptide recognition modules from phage-displayed peptide libraries". In: *Nat Protoc* 2.6 (2007), pp. 1368–86. DOI: 10.1038/nprot.2007.151.

[66] Mojca Lunder et al. "Affinity ranking of phage-displayed peptides: Enzyme-linked immunosorbent assay versus surface plasmon resonance". In: *Acta Chimica Slovenica* 55 (2008), pp. 233–235.

[67] E. Lasonder, G. A. Schellekens, and G. W. Welling. "A fast and sensitive method for the evaluation of binding of phage clones selected from a surface displayed library". In: *Nucleic acids research* 22.3 (1994), pp. 545–546. DOI: 10.1093/nar/22.3.545. URL: https://pubmed.ncbi.nlm.nih.gov/8127700%20https://www.ncbi.nlm.nih.gov/pmc/articles/PMC523622/.

[68] A. Shabani et al. "Bacteriophage-modified microarrays for the direct impedimetric detection of bacteria". In: *Anal Chem* 80.24 (2008), pp. 9475–82. DOI: 10.1021/ac801607w.

[69] Chaker Tlili et al. "Bacteria Screening, Viability, And Confirmation Assays Using Bacteriophage-Impedimetric/Loop-Mediated Isothermal Amplification Dual-Response Biosensors". In: *Analytical Chemistry* 85.10 (2013), pp. 4893–4901. DOI: 10.1021/ac302699x. URL: https://doi.org/10.1021/ac302699x.

[70] M. Tolba et al. "A bacteriophage endolysin-based electrochemical impedance biosensor for the rapid detection of Listeria cells". In: *Analyst* 137.24 (2012), pp. 5749–56. DOI: 10.1039/c2an35988j.

[71] T. A. Kunkel, J. D. Roberts, and R. A. Zakour. "Rapid and efficient site-specific mutagenesis without phenotypic selection". In: *Methods Enzymol* 154 (1987), pp. 367–82. DOI: 10.1016/0076-6879(87)54085-x.

[72] P. Costet, M. Krempf, and B. Cariou. "PCSK9 and LDL cholesterol: unravelling the target to design the bullet". In: *Trends Biochem Sci* 33.9 (2008), pp. 426–34. DOI: 10.1016/j.tibs.2008.06.005.

[73] J. D. Horton, J. C. Cohen, and H. H. Hobbs. "PCSK9: a convertase that coordinates LDL catabolism". In: *J Lipid Res* 50 Suppl.Suppl (2009), S172–7. DOI: 10.1194/jlr.R800091-JLR200.

[74] N. G. Seidah. "PCSK9 as a therapeutic target of dyslipidemia". In: *Expert Opin Ther Targets* 13.1 (2009), pp. 19–28. DOI: 10.1517/14728220802600715.

[75] D. W. Zhang et al. "Binding of proprotein convertase subtilisin/kexin type 9 to epidermal growth factor-like repeat A of low density lipoprotein receptor decreases receptor recycling and increases degradation". In: *J Biol Chem* 282.25 (2007), pp. 18602–12. DOI: 10.1074/jbc.M702027200.

[76] Y. Zhang et al. "Identification of a small peptide that inhibits PCSK9 protein binding to the low density lipoprotein receptor". In: *J Biol Chem* 289.2 (2014), pp. 942–55. DOI: 10.1074/jbc.M113.514067.

[77] Xiao-Li Zhou et al. "Surface Plasmon Resonance Microscopy: From Single-Molecule Sensing to Single-Cell Imaging". In: *Angewandte Chemie International Edition* 59.5 (2020), pp. 1776–1785. DOI: https://doi.org/10.1002/anie.201908806. URL: https://onlinelibrary.wiley.com/doi/abs/10.1002/anie.201908806.

[78] Simon G. Patching. "Surface plasmon resonance spectroscopy for characterisation of membrane protein–ligand interactions and its potential for drug discovery". In: *Biochimica et Biophysica Acta (BBA) - Biomembranes* 1838.1, Part A (2014), pp. 43–55. DOI: https://doi.org/10.1016/j.bbamem.2013.04.028. URL: http://www.sciencedirect.com/science/article/pii/S0005273613001466.

[79] Noemi Bellassai et al. "Surface Plasmon Resonance for Biomarker Detection: Advances in Non-invasive Cancer Diagnosis". In: *Frontiers in Chemistry* 7.570 (2019). DOI: 10.3389/fchem.2019.00570. URL: https://www.frontiersin.org/article/10.3389/fchem.2019.00570.

[80] D. G. Myszka. "Analysis of small-molecule interactions using Biacore S51 technology". In: *Anal Biochem* 329.2 (2004), pp. 316–23. DOI: 10.1016/j.ab.2004.03.028.

[81] Shaopeng Wang et al. "Label-free imaging, detection, and mass measurement of single viruses by surface plasmon resonance". In: *Proceedings of the National Academy of Sciences of the United States of America* 107.37 (2010), pp. 16028–16032. DOI: 10.1073/pnas.1005264107. URL: https://pubmed.ncbi.nlm.nih.gov/20798340%20https://www.ncbi.nlm.nih.gov/pmc/articles/PMC2941305/.

[82] Wei Wang et al. "Label-free measuring and mapping of binding kinetics of membrane proteins in single living cells". In: *Nature Chemistry* 4.10 (2012), pp. 846–853. DOI: 10.1038/nchem.1434. URL: https://doi.org/10.1038/nchem.1434.

[83] K. Syal et al. "Plasmonic imaging of protein interactions with single bacterial cells". In: *Biosens Bioelectron* 63 (2015), pp. 131–137. DOI: 10.1016/j.bios.2014.06.069.

[84] Qing Liu et al. "Mach–Zehnder interferometer (MZI) point-of-care system for rapid multiplexed detection of microRNAs in human urine specimens". In: *Biosensors and Bioelectronics* 71 (2015), pp. 365–372. DOI: https://doi.org/10.1016/j.bios.2015.04.052. URL: http://www.sciencedirect.com/science/article/pii/S0956566315300476.

[85] César S. Huertas, David Fariña, and Laura M. Lechuga. "Direct and Label-Free Quantification of Micro-RNA-181a at Attomolar Level in Complex Media Using a Nanophotonic Biosensor". In: *ACS Sensors* 1.6 (2016), pp. 748–756. DOI: 10.1021/acssensors.6b00162. URL: https://doi.org/10.1021/acssensors.6b00162.

[86] N. B. Shah and T. M. Duncan. "Bio-layer interferometry for measuring kinetics of protein-protein interactions and allosteric ligand effects". In: *J Vis Exp* 84 (2014), e51383. DOI: 10.3791/51383.

[87] Kerry J. Vahala. "Optical microcavities". In: *Nature* 424.6950 (2003), pp. 839–846. DOI: 10.1038/nature01939. URL: https://doi.org/10.1038/nature01939.

[88] F. Ghasemi et al. "Multiplexed detection of lectins using integrated glycan-coated microring resonators". In: *Biosens Bioelectron* 80 (2016), pp. 682–690. DOI: 10.1016/j.bios.2016.01.051.

[89] Martin D. Baaske, Matthew R. Foreman, and Frank Vollmer. "Single-molecule nucleic acid interactions monitored on a label-free microcavity biosensor platform". In: *Nature Nanotechnology* 9.11 (2014), pp. 933–939. DOI: 10.1038/nnano.2014.180. URL: https://doi.org/10.1038/nnano.2014.180.

[90] Guoliang Wang et al. "A combined reflectometry and quartz crystal microbalance with dissipation setup for surface interaction studies". In: *Review of Scientific Instruments* 79.7 (2008), p. 075107. DOI: 10.1063/1.2957619. URL: https://aip.scitation.org/doi/abs/10.1063/1.2957619.

[91] David W. Ralin et al. "Kinetic Analysis of Glycoprotein–Lectin Interactions by Label-Free Internal Reflection Ellipsometry". In: *Clinical Proteomics* 4.1 (2008), pp. 37–46. DOI: 10.1007/s12014-008-9007-y. URL: https://doi.org/10.1007/s12014-008-9007-y.

[92] Yangyang Chen et al. "Optical biosensors based on refractometric sensing schemes: A review". In: *Biosensors and Bioelectronics* 144 (2019), p. 111693. DOI: https://doi.org/10.1016/j.bios.2019.111693. URL: http://www.sciencedirect.com/science/article/pii/S0956566319307729.

[93] Augusto García-Valenzuela, Mary Peña-Gomar, and Claudia Fajardo-Lira. "Measuring and sensing a complex refractive index by laser reflection near the critical angle". In: *Optical Engineering - OPT ENG* 41 (2002). DOI: 10.1117/1.1483084.

[94] Meng Li et al. "Total Internal Reflection-Based Extinction Spectroscopy of Single Nanoparticles". In: *Angewandte Chemie International Edition* 58.2 (2019),

pp. 572–576. DOI: https://doi.org/10.1002/anie.201810324. URL: https://onlinelibrary.wiley.com/doi/abs/10.1002/anie.201810324.

[95] S. G. Kazarian and K. L. A. Chan. "Applications of ATR-FTIR spectroscopic imaging to biomedical samples". In: *Biochimica et Biophysica Acta (BBA) - Biomembranes* 1758.7 (2006), pp. 858–867. DOI: https://doi.org/10.1016/j.bbamem.2006.02.011. URL: http://www.sciencedirect.com/science/article/pii/S0005273606000630.

[96] K. L. Andrew Chan and S. G. Kazarian. "Attenuated total reflection Fourier-transform infrared (ATR-FTIR) imaging of tissues and live cells". In: *Chem Soc Rev* 45.7 (2016), pp. 1850–64. DOI: 10.1039/c5cs00515a.

[97] G. Steiner. "Surface plasmon resonance imaging". In: *Anal Bioanal Chem* 379.3 (2004), pp. 328–31. DOI: 10.1007/s00216-004-2636-8.

[98] Max Born and Emil Wolf. *Principles of Optics: Electromagnetic Theory of Propagation, Interference and Diffraction of Light*. 7th ed. Cambridge: Cambridge University Press, 1999. DOI: DOI:10.1017/CBO9781139644181. URL: https://www.cambridge.org/core/books/principles-of-optics.

[99] Mary Carmen Peña-Gomar and Augusto García-Valenzuela. "Reflectivity of a Gaussian beam near the critical angle with external optically absorbing media". In: *Applied Optics* 39.28 (2000), pp. 5131–5137. DOI: 10.1364/AO.39.005131. URL: http://ao.osa.org/abstract.cfm?URI=ao-39-28-5131.

[100] V. M. Krishnamurthy et al. "Carbonic anhydrase as a model for biophysical and physical-organic studies of proteins and protein-ligand binding". In: *Chem Rev* 108.3 (2008), pp. 946–1051. DOI: 10.1021/cr050262p.

[101] F. Zhang et al. "Quantification of epidermal growth factor receptor expression level and binding kinetics on cell surfaces by surface plasmon resonance imaging". In: *Anal Chem* 87.19 (2015), pp. 9960–5. DOI: 10.1021/acs.analchem.5b02572.

[102] H. Ghazarian, B. Idoni, and S. B. Oppenheimer. "A glycobiology review: carbohydrates, lectins and implications in cancer therapeutics". In: *Acta Histochem* 113.3 (2011), pp. 236–47. DOI: 10.1016/j.acthis.2010.02.004.

[103] Rita Santos et al. "A comprehensive map of molecular drug targets". In: *Nature Reviews Drug Discovery* 16.1 (2017), pp. 19–34. DOI: 10.1038/nrd.2016.230. URL: https://doi.org/10.1038/nrd.2016.230.

[104] Edson X. Albuquerque et al. “Mammalian nicotinic acetylcholine receptors: from structure to function”. In: *Physiological reviews* 89.1 (2009), pp. 73–120. DOI: 10.1152/physrev.00015.2008. URL: https://pubmed.ncbi.nlm.nih.gov/19126755%20https://www.ncbi.nlm.nih.gov/pmc/articles/PMC2713585/.

[105] F. Zhang et al. “Label-Free Quantification of Small-Molecule Binding to Membrane Proteins on Single Cells by Tracking Nanometer-Scale Cellular Membrane Deformation”. In: *ACS Nano* 12.2 (2018), pp. 2056–2064. DOI: 10.1021/acsnano.8b00235.

[106] Yan Guan et al. “Kinetics of small molecule interactions with membrane proteins in single cells measured with mechanical amplification”. In: *Science Advances* 1.9 (2015), e1500633. DOI: 10.1126/sciadv.1500633. URL: http://advances.sciencemag.org/content/1/9/e1500633.abstract.

[107] Guangzhong Ma et al. “Optical imaging of single-protein size, charge, mobility, and binding”. In: *Nature Communications* 11.1 (2020), p. 4768. DOI: 10.1038/s41467-020-18547-w. URL: https://doi.org/10.1038/s41467-020-18547-w.

[108] Y. Yang et al. “Label-Free Tracking of Single Organelle Transportation in Cells with Nanometer Precision Using a Plasmonic Imaging Technique”. In: *Small* 11.24 (2015), pp. 2878–84. DOI: 10.1002/smll.201403016.

[109] Benjamin J. Zeskind et al. “Nucleic acid and protein mass mapping by live-cell deep-ultraviolet microscopy”. In: *Nature Methods* 4.7 (2007), pp. 567–569. DOI: 10.1038/nmeth1053. URL: https://doi.org/10.1038/nmeth1053.

[110] Johannes Schindelin et al. “Fiji: an open-source platform for biological-image analysis”. In: *Nature Methods* 9.7 (2012), pp. 676–682. DOI: 10.1038/nmeth.2019. URL: https://doi.org/10.1038/nmeth.2019.